Multi-bistability and spin dynamics of ring-shaped multi-nuclear metal complexes

Takuto Matsumoto

February 2014

Multi-bistability and spin dynamics of ring-shaped multi-nuclear metal complexes

Takuto Matsumoto
Doctoral Program in Frontier Science

Submitted to the Graduate School of
Pure and Applied Sciences
in Partial Fulfillment of the Requirements
for the Degree of Doctor of Philosophy in
Science

at the
University of Tsukuba

INDEX

CHAPTER 1

General Introduction

1.1 Aim of This Thesis

Chemistry allows us to make new materials and its developments can have huge impacts on our everyday lives. In the 21st century, nano-technologies are required for development of computer science, tackling energy problems, enhancing human health and protecting our natural environment. Transition metal complexes are inorganic (metal ion) and organic (ligand) hybrid systems, and therefore show many interesting physical phenomena; magnetism, redox behaviour, conductivity, dielectric and optical properties originating from the inorganic metal ions and high designability due to the organic ligands. In particular, multi-nuclear metal complexes show peculiar physical properties and functions that cannot be realized by mono-nuclear complexes, and thus have attracted a great deal of attention, not only from within the chemistry community, but from other associated fields interested in the search for new physical phenomena and biologically-inspired synthetic systems. The coordination bond is the origin of unique phenomena such as catalytic behavior, but it can be difficult for the chemist to predict the final structure of a coordination complex. In order to maximize the functionality of a metal complex, the coordination chemist needs employ a molecular design approach. For example, the controlled inclusion of a reaction centre in the coordination sphere of a metal centre can be critical in the synthesis of homogeneous catalysts. Further, the positions and connectivity of transition metal ions in a multinuclear cluster is a vital synthetic goal, as the control of electronic interactions between metal ions leads to the expression of tunable physical properties. The paramagnetic nature of most transition metal ions means that it is difficult to analyze the structure of metal complexes using a nuclear magnetic resonance (NMR). Moreover, metal complexes usually exist in equilibrium in the solution-state, and it can be difficult to accurately determine their composition by mass spectrometry. The dissociation of metal complex in solution can also make it difficult to prepare single crystals. Thus, the rational syntheses and multi-functionalization of metal complexes are challenging topics in coordination chemistry. Of particular interest to the author are the specific physical properties of multinuclear complexes derived from their molecular structures, i.e. the structure-property relationship. The topologies of metal ion arrays dictate their electronic properties, and the rational molecular design of coordination compounds can provide various coordination architectures with uncommon shapes not found in inorganic compounds, such as an isolated chains (wires), rings, wheels, two-dimensional grids, cubes, cages, and nanoparticles. Ring-shaped multinuclear complexes have a simple, regular and highly symmetrical array of metal ions, in which the metal ions are usually in the same electronic state. Considering the physical properties derived from the electronic states of constituent metal ions, ring-shaped molecules can exhibit electronic fluctuations and low-energy excitations due to cooperative effects upon the application of external stimuli, resulting in multi-stable switchable properties. To investigate the potentially accessible physical properties the author studied the rational syntheses of ring-shaped multi-nuclear metal complexes

and studied their multi-bistability and spin dynamics. The results are shown in the following chapters.

In this thesis, the structures and magnetic properties of ring-shaped multi-nuclear metal complexes were studied. Frist, a brief overview of the important topics relating to the titled work is introduced in CHAPTER 1. With particular relevance to CHAPTER 2, spin-crossover phenomena, mixed-valence complexes, grid-like metal complexes, and coordination compounds with multi-stability are introduced in the following sections. In CHAPTER 2, a new multi-bistable system based on tetranuclear Fe grids is proposed and demonstrated. The grids showed thermal or light induced multi-step spin-crossover behaviour and multi-bistability. In CHAPTER 3, solid-state NMR measurements of antiferromagnetic six, seven, and eight membered rings are discussed in order to elucidate the magnetic ground state of the oxo-vanadium rings. In CHAPTER 4, the synthetic strategy for triangular trinuclear complexes with planar structures is investigated. The ligand design, syntheses and magnetic properties of triangular tri-nuclear complexes with copper and nickel ions are described.

1.2 Spin-crossover Complexes

Non-coordinated transition metal ions have quintet-degenerate d-orbitals. According to crystal field theory, the splitting of d-orbitals (Δ_o, 10 Dq) is based on the electronic repulsions between the d-electrons and the ligands. In the case of the six-coordinated octahedral coordination mode, the two d-orbitals that are directly towards the ligands (e_g) are destabilized, causing them to split from the remaining three d-orbitals (t_{2g}), which are stabilized. The electronic arrangements of six-coordinated octahedral complexes with d^n (n = 4 - 7) electrons depend on the relative strengths of Δ_o and the spin pairing energy P. In case of $\Delta_o << P$, the electrons are arranged to make maximize their sum of spin angular momentum following Hund's rule (high spin (HS) state, Figure 1.1 (left)). In the reverse situation, Hund's rule is broken and the electrons make pairs and occupy the t_{2g} orbitals, preferentially (low spin (LS) state, Figure 1.1 (right)). When the Δ_o and P are close, some first transition metal ions with d^4 to d^7 electronic configurations may show reversible spin-crossover (SCO) behaviour between their HS and LS states by stimuli like temperature, light, and pressure.

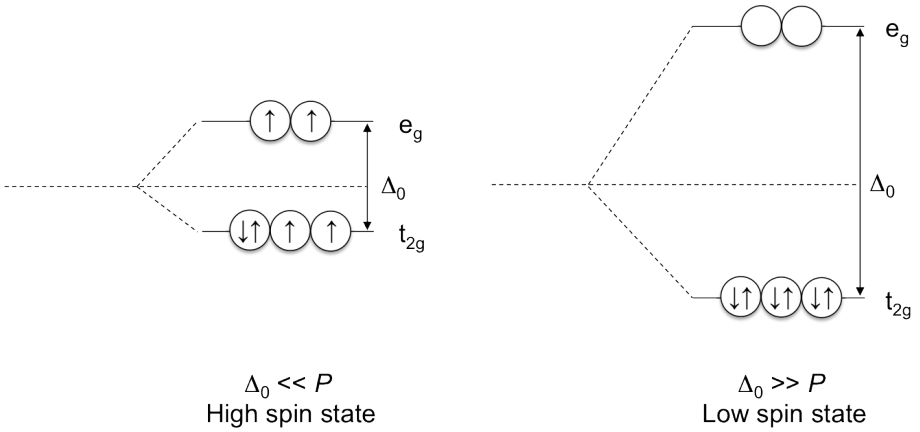

Figure 1.1: High spin (left) and low spin (right) state of six-coordinated octahedral metal ions with d^6 electrons.

An iron(II) SCO complexes, $[Fe(phen)_2(NCE)_2]$ (phen = 1,10-phenanthroline, E = S, Se), was discovered in 1964,[1] and its SCO behaviour were recognized three years later by magnetic measurements (Figure 1.2).[2] Iron(II) complexes are the most commonly reported thermal SCO materials and show dramatic magnetic changes between their paramagnetic HS state ($t_{2g}^4e_g^2$, $^5T_{2g}$ S = 2) and diamagnetic LS state (t_{2g}^6, $^1A_{1g}$) upon the application of external stimuli. In the HS state, their d-electrons occupy the anti-bonding e_g orbitals, thus the coordination bond distances between the iron ion and donor atoms of HS state are usually longer than in the LS state. SCO phenomena also induce color changes. HS-Fe(II) in a N_6 coordination environment SCO complex shows the spin allowed d-d transition $^5T_{2g} \rightarrow {}^5E_g$, which translates to give a value of 10 Dq as ca. 12,000 cm^{-1}.[3] In the LS state, the iron(II) complex showed d-d transition $^1A_{1g} \rightarrow {}^1T_{2g}$ and strong absorption band corresponding to the metal to ligand charge transfer (MLCT) band for extended π-system around 20,000 cm^{-1}.

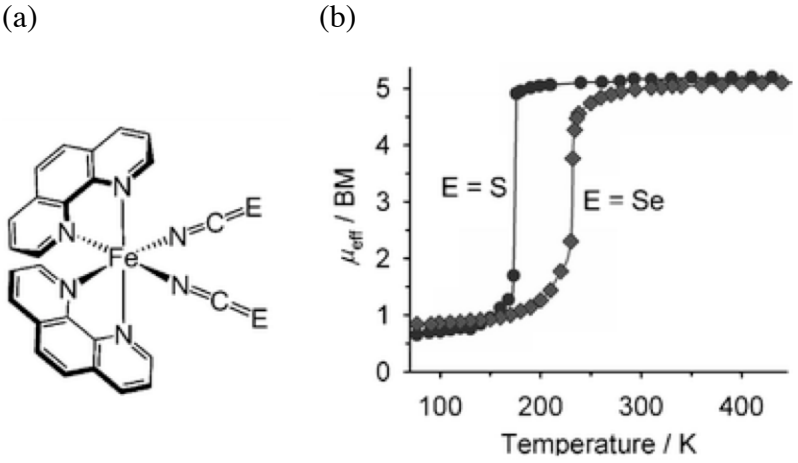

Figure 1.2: (a) The structural formula of $[Fe^{II}(phen)_2(NCE)_2]$. (b) Thermal SCO behaviour of $[Fe^{II}(phen)_2(SCN)_2]$ (●) and $[Fe^{II}(phen)_2(NCSe)_2]$ (◆).

Some iron complexes show photo-induced SCO behaviour termed light-induced excited spin state trapping (LIESST). For LS-Fe(II) SCO-active complexes at very low temperature, light induces the transition of an electron of the $^1A_1$ state to the $^1T_1$ state (ca. 550 nm). This excited electron shows relaxation to the ground state ($^1A_1$) or lowest energy level of HS state ($^5T_{2g}$) via $^3T_2$ and $^3T_1$ states (Figure 1.3). Due to the difference of spin multiplet and the high potential barrier, the relaxation time from HS ($^5T_{2g}$) to LS ($^1A_1$) state is very slow at low temperature. Thus, the electron excited to the HS state is trapped by light irradiation. Additional excitations of $^1A_1$ electrons generate the $^5T_{2g}$ state, and lead to full transition to the HS state.

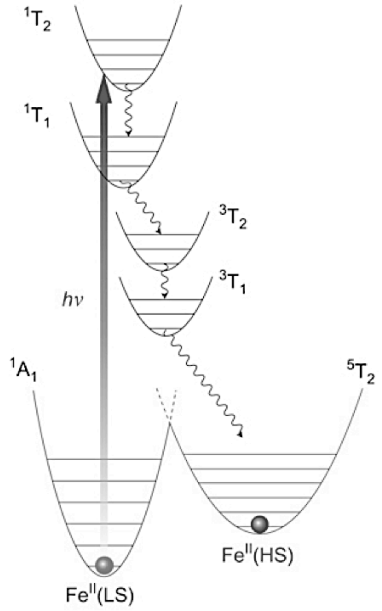

Figure 1.3: Potential wells of the d^6 spin-crossover system at low temperature. Arrows indicate the mechanism of LIESST.

LIESST phenomena can be detected from changes in the magnetic moment. In the SQUID (superconducting quantum interference device) chamber, when a LIESST active SCO complex in the LS state was irradiated by light at low temperature, increase of the $\chi_m T$ value can be observed, corresponding to the LS to HS state transition (Figure 1.4). Although the light-excited state is stable even in the dark at low temperature region, heating of the sample induces thermal relaxation of the excited state, returning the complex to its original LS state.[4] While LIESST active species have potential applications as photo-responsive switching materials, they are likely to be operative only at low temperature, i.e. below approximately 50 K.

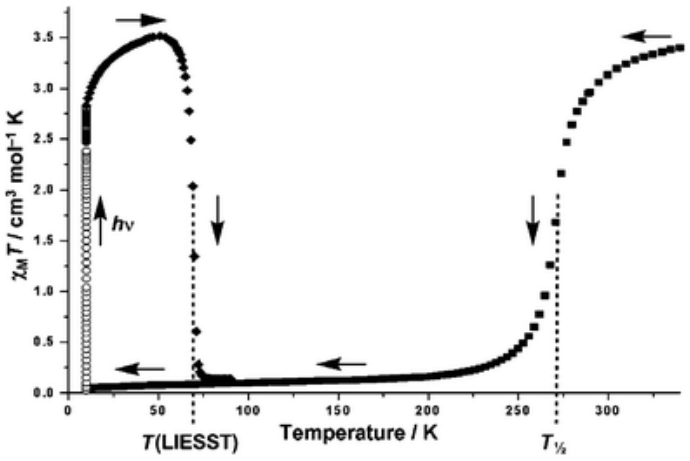

Figure 1.4: Thermal (■) and light (○) induced SCO behavior of a typical SCO active Fe (II) complex. The light induced excited state shows thermal relaxation upon heating (◆).

J.-F. Létard and his coworkers researched the relationship between the thermal spin transition temperature ($T_{1/2}$) and thermal relaxation temperature of light excited HS state to LS state T(LIESST) (Figure 1.5).[5] The results showed that complexes with high $T_{1/2}$ show low T(LIESST) in the same coordination mode, generally, and comparing the T(LIESST) of tris-bidentate and bis-tridentate complexes with same $T_{1/2}$, the T(LIESST) of the bis-tridentate complexes are higher than those of the tris-bidentate species. Bis-tridentate complexes show large structural changes upon spin transition, therefore energetically stabilizing the light-induced HS state. When considering light-switchable SCO memory devices, the use of ligands with tridentate coordination site might be more effective.

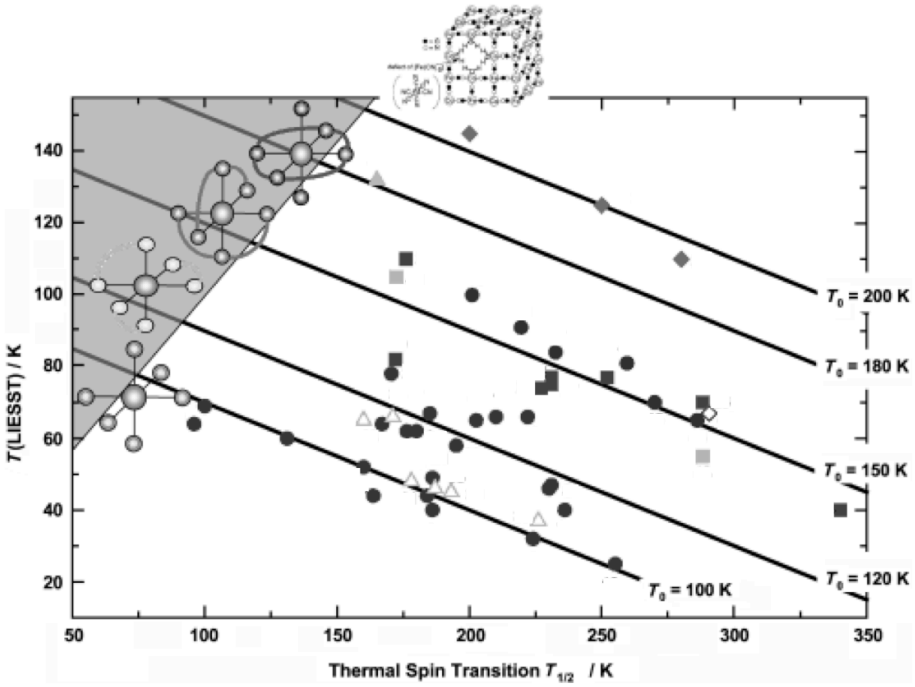

Figure 1.5: Variation of T(LIESST) versus $T_{1/2}$ for several SCO compounds.

The syntheses of multi-nuclear SCO complexes is a challenging topic in coordination chemistry. To the best author's knowledge, a discrete nano-ball, $[\{Cu^{I}(Tp^{4\text{-py}})(CH_3CN)\}_8\{Fe^{II}(NCS)_2\}_{10/3}\{Fe^{II}(NCS)(CH_3CN)\}_{8/3}](ClO_4)_{8/3}\cdot n CH_3CN$ ($(Tp^{4\text{-py}})^-$ = [tris{3-(4'-pyridyl)-pyrazol-1-yl}hydroborate]), is the largest SCO-active complex, and its synthesis and SCO behaviour were reported by Batten et al. in 2009.[6] The nano-ball has a rigid $[Fe^{II}_6\{Cu^{I}(Tp^{4\text{-py}})\}_8]$ cage structure with an approximate diameter of 3 nm, while there is a huge space that is filled by solvent molecules between the cages (Figure 1.6). Thus, this nano-ball showed not only thermal and light-induced SCO behaviour but also solvent absorption/desorption induced SCO behaviour (Figures 1.6 (b) and (c)).

(a) (b) (c)

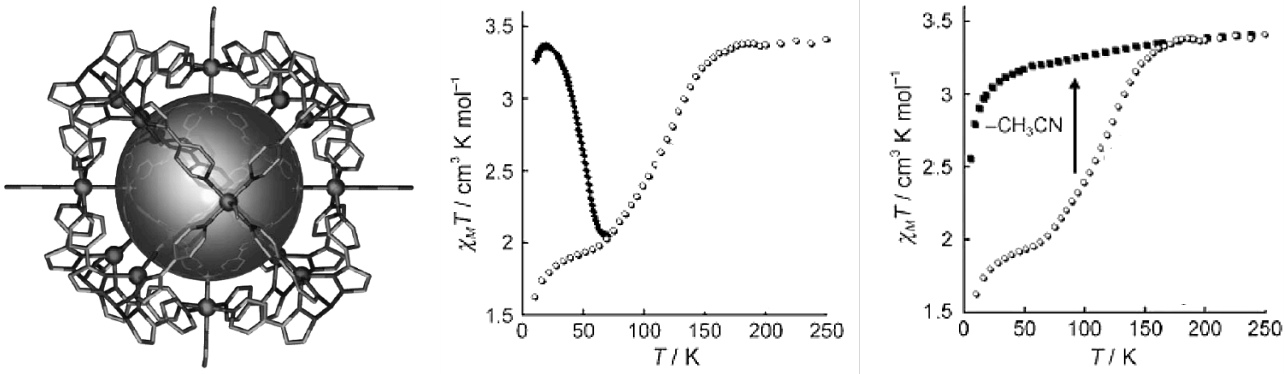

Figure 1.6: (a) The core structure of $[Fe^{II}_6(NCS)_{36-x}(CH_3CN)_x\{Cu^I(Tp^{4-py})\}_8]$ cage. (b) The magnetic data of thermal (○) and light (◆) induced SCO behaviour. (c) The magnetic data of guest-sorbed (○) and desorbed (■) species.

1.3 Mixed-valence Complexes

Mixed-valence complexes are multi-nuclear metal complexes containing metal ions with different oxidation numbers (valence). Some mixed-valence complexes exhibit electron transfer between the metal ions with different valence, and then valence/electron fluctuation, spatially and temporally can be observed. Valence fluctuations exhibit characteristic absorption spectra, due to their inter-valence charge transfer (IVCT) band. The analysis of an IVCT band gives yields information on the nature of the inter-metal electronic interaction, and some parameters, H_{ab} and α^2, have been introduced as estimations of the degree of electron delocalization:[7]

$$H_{ab} = 2.06 \times 10^{-2}(\varepsilon_{max} v_{max} \Delta v_{1/2})^{1/2}/(br) \quad (1.1)$$

$$\alpha^2 = 4.2 \times 10^{-4} \varepsilon_{max} \Delta v_{1/2}/(b v_{max} r^2) \quad (1.2)$$

where ε_{max}, $\Delta v_{1/2}$, b, v_{max} and r denote the maximum molar absorption coefficient, the full width at half maximum of the IVCT band, the degeneracy of the transition, the maximum energy of the IVCT band and the distance between the metal centres respectively. Robin and Day grouped IVCT bands into three classes depending on the degree of electron delocalization (Figure 1.7);[8]

Class I $(\alpha^2 \approx 0)$
The interaction between metal ions is very weak, and valence electrons are localized on their metal ions.

Class II $(0 < \alpha^2 < 0.5)$
The interactions of metal ions are stronger than Class I, and electrons are slightly delocalized between the metal ions.

Class III ($\alpha^2 = 0.5$)

The interactions of metal ions are very strong, and electrons are completely delocalized between the metal ions. The metal ions cannot be distinguished by any optical measurements.

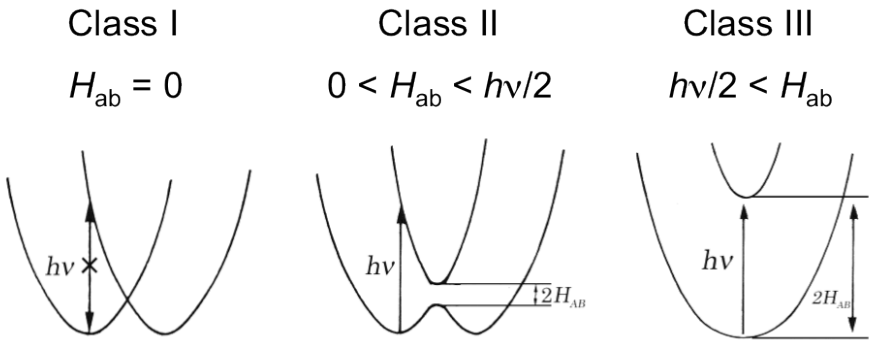

Figure 1.7: The symmetric potential surface of di-nuclear mixed-valence complex.

In mixed-valence systems, the dynamics of valence electrons are an interesting topic. Carboxylate-bridged tri-nuclear iron systems, for example, $[Fe_3O(O_2CCH_2CN)_6(H_2O)_3]$ consist of two Fe^{III} and one Fe^{II} ions, and the mixed-valence state is stable in air.[9] At room temperature, the space group of the single crystal is $R\bar{3}$, which has a crystalographic C_3 axis at the centre of the iron triangular core, and the different iron valence states cannot be differentiated by X-ray structural analysis (Figure 1.8(a)). The ^{57}Fe Mössbauer spectrum of the triangle at room temperature shows one doublet peak, suggesting that the valence electrons of the iron ions are delocalized between the metal centres (Figure 1.8(b)). Both these analyses indicate that $[Fe_3O(O_2CCH_2CN)_6(H_2O)_3]$ is a class III delocalized system at room temperature. When the complex is cooled down to 100 K, the space group changes to $P\bar{1}$, indicating the occurrence of a structural phase transition. As the symmetry was broken, Mössbauer spectra changed and showed two doublet peaks, corresponding to HS-Fe^{III} and HS-Fe^{II}. The phase transition was detected by not only structural analyses but also heat capacity measurements (Figure 1.8 (c)). The results showed that the dynamics of valence strongly depend on temperature and the symmetry of the cluster core, and that the complex showed class II electron delocalization at low temperature.

(a)

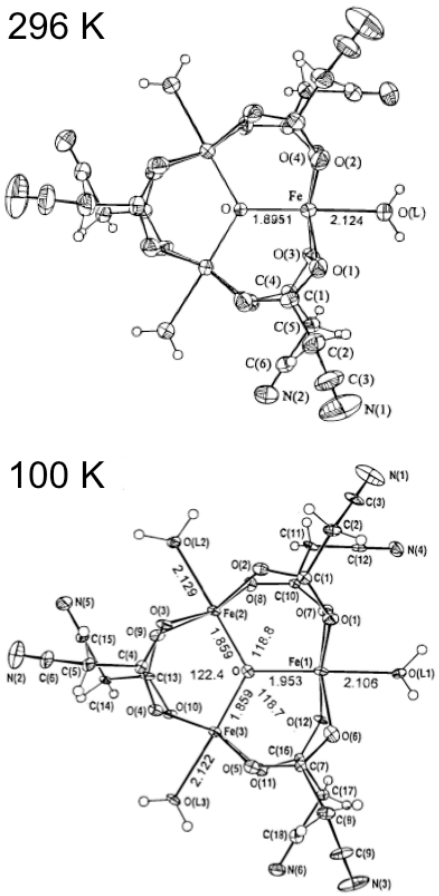

(b)

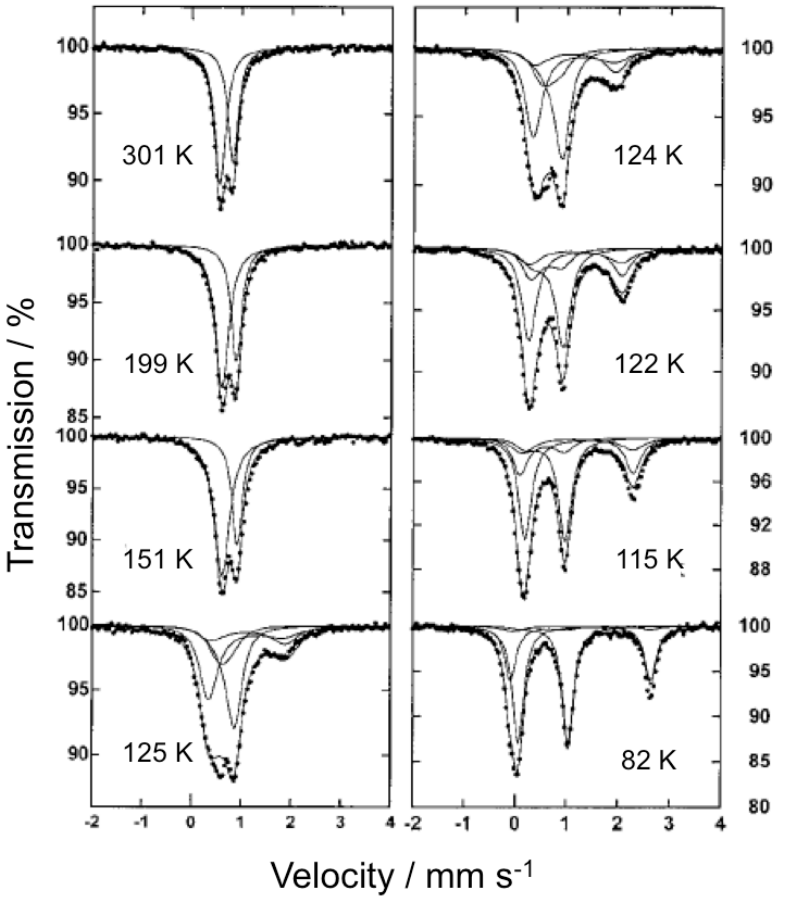

(c)

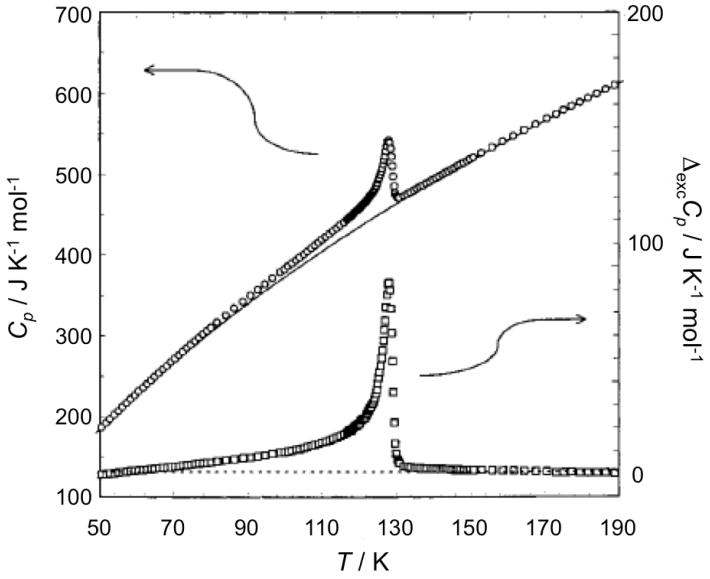

Figure 1.8: (a) The structural analyses of $[Fe_3O(O_2CCH_2CN)_6(H_2O)_3]$ at 296 K (top) and 100 K (bottom). (b) Temperature dependent Mössbauer spectra. The solid lines represent theoretical fits. (c) Molar heat capacity (○) and excess heat capacity due to the phase transition (□).

The manganese Keggin-type cluster, $[Mn^{IV}Mn^{III}_{12}O_6(OH)_2(OMe)_4(bemp)_6]^{4+}$ ($[Mn_{13}]^{4+}$, H_3bemp = 2,6-bis[*N*-(2-hydroxyethyl)iminomethyl]-4-methylphenol), is a mixed-valence complex, and the electrochemical and magnetic properties were reported by Oshio et al. in 2011 (Figure 1.9 (a)).[10] $[Mn_{13}]^{4+}$ shows four quasi-reversible redox waves, corresponding to four one-electron redox processes of $[Mn_{13}]^{2+}/[Mn_{13}]^{3+}$, $[Mn_{13}]^{3+}/[Mn_{13}]^{4+}$, $[Mn_{13}]^{4+}/[Mn_{13}]^{5+}$, and $[Mn_{13}]^{5+}/[Mn_{13}]^{6+}$, respectively (Figure 1.9 (b)). The comproportionation constants of the one electron reduced $[Mn_{13}]^{3+}$, the native species $[Mn_{13}]^{4+}$, and the one electron oxidized $[Mn_{13}]^{5+}$ are estimated to be 560, 2.6×10^5, and 5.5×10^3, respectively, suggesting that $[Mn_{13}]^{5+}$ is relatively stable in solution. The one electron and fully oxidized complexes, $[Mn_{13}]^{5+}$ and $[Mn_{13}]^{6+}$, were synthesized by chemical oxidation, and the magnetic properties were measured. All $[Mn_{13}]^{n+}$ (n = 4～6) clusters showed slow magnetic relaxation, below their blocking temperatures, and single molecule magnet (SMM) behaviour. The magnetization curves at 0.04 K showed that the hysteresis loops depended on their oxidation states (Figure 1.9 (c)). These experiments indicate that the physical properties of metal complexes clearly depend on their valence states.

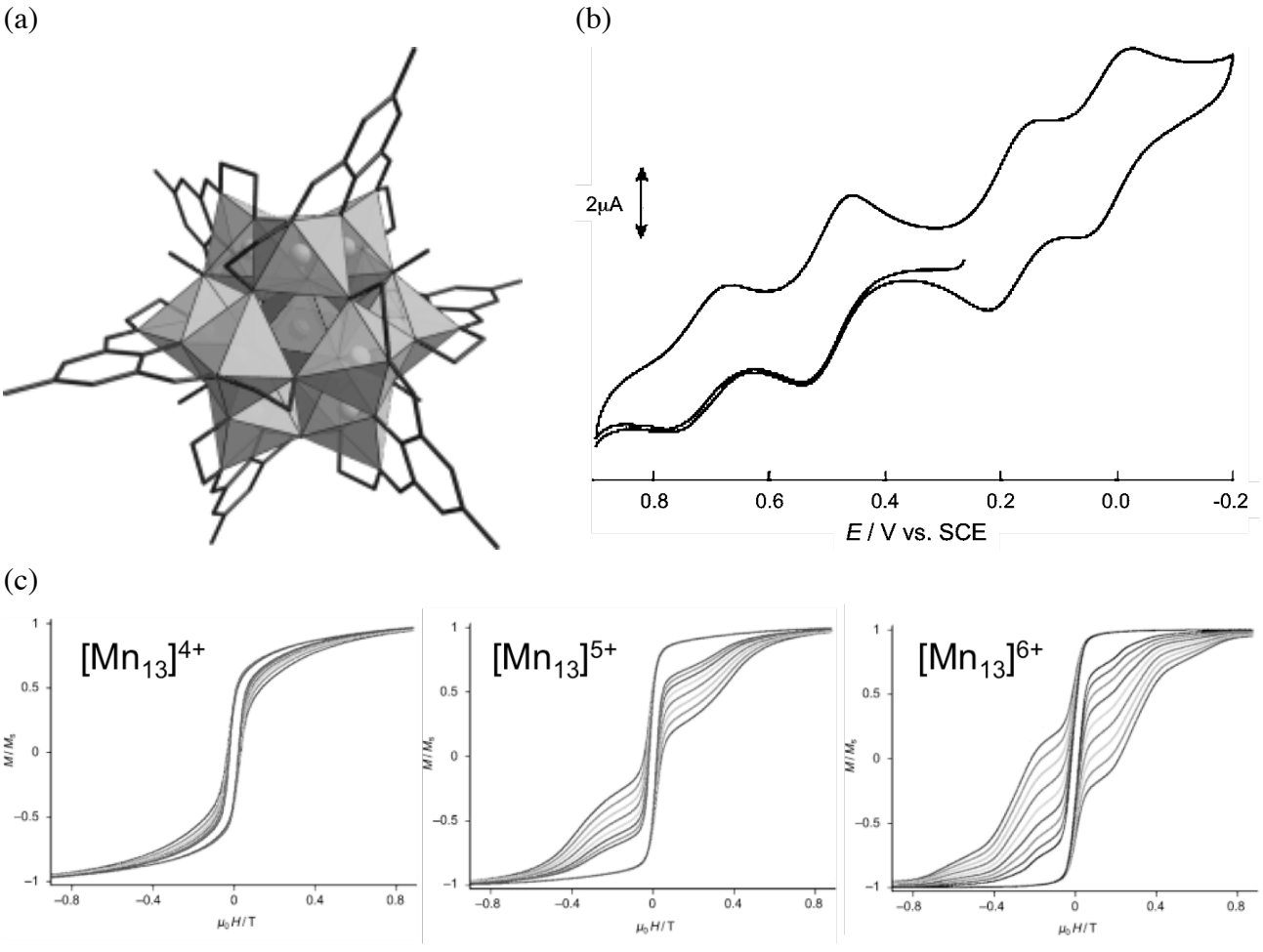

Figure 1.9: (a) The crystal structure of $[Mn_{13}]^{4+}$. (b) The cyclic voltammogram of $[Mn_{13}]^{4+}$ in N,N-dimethylformamide. (c) The hysteresis measurements displaying the scan-rate dependence for $[Mn_{13}]^{4+}$ (left), $[Mn_{13}]^{5+}$ (centre), and $[Mn_{13}]^{6+}$ (right) at 0.04 K.

1.4 Grid-like Metal Complexes

Grid-like metal complexes are multi-nuclear metal clusters in which multi-dentate ligands bridge between metal ions, to generate molecular structures that look like grids. The smallest grid-like complex is a [2 × 2] grid that consists of four metal ions and four bridging ligands. First, a copper(I) tetranuclear grid-like architecture, $[Cu^{I}_{4}(L1)_{4}](CF_3SO_3)_4$ (L1 = 3,6-bis(2'-pyridyl)pyridazine), was reported by Youinou et al. in 1992.[11] Next, a cobalt grid-like complex, $[Co^{II}_{4}(L2)_{4}]^{8+}$ (L2 = 2-methyl-4,6-bis(2',2''-bipyrid-6'-yl)-2-phenyl-pyrimidine), was well studied from the viewpoint of self-assembly by J.-M. Lehn et al..[12] They prepared a poly-pyridyl type bis-tridentate ligand for the construction of a [2 × 2] grid, and the ligand bridged between the metal ions via a pyrimidine moiety. The metal ions assembled with the ligands to produce a stable grid-like structure, with N_6 coordination environments. In 2000, an iron tetra-nuclear grid-like complex, $[Fe^{II}_{4}(L3)_{4}](ClO_4)_8$ (L3 = 4,6-bis(2',2''-bipyrid-6'-yl)-2-phenyl-pyrimidine), was reported and the structure and magnetic properties were studied.[13] This iron grid showed gradual thermal SCO behaviour over a wide temperature region and pressure induced SCO behaviour. Moreover, the grid also showed LIESST upon irradiation with an Ar-ion laser (514 nm) irradiation at low temperature. A few years later, O. Sato et al. and F. Meyer et al. reported further SCO active iron grids. O. Sato and his co-workers prepared an oxygen donating bridging ligand and its iron(II) [2 × 2] grid complex, $[Fe^{II}_{4}(HL4)_{4}](BF_4)_4 \cdot 2H_2O \cdot CH_3OH$, which showed one-step thermal SCO behaviour (4HS ⇄ 2HS-2LS).[14] The crystal structure of its 2HS-LS state suggests that the grid had a *cis*-2HS-2LS configuration. F. Meyer and his co-workers reported a pyrazolate bridged-type iron(II) [2 × 2] grid, $[Fe^{II}_{4}(L5)_{4}](BF_4)_4 \cdot 4DMF$ (HL5 = 3,5-bis[6-(pyrid-2-yl)pyrid-2-yl]-1*H*-pyrazole), which showed two-step thermal SCO behavior (Figure 1.10).[15] This pyrazolate bridged grid showed four step redox behaviour corresponding to the one-electron oxidation of the four iron centres, and a two electron oxidized complex was isolated ($[Fe^{III}_{2}Fe^{II}_{2}(L5)_{4}](BF_4)_6 \cdot 3CH_3CN$). The spin state of the mixed-valence grid was $[(LS\text{-}Fe^{III})_2(HS\text{-}Fe^{II})_2]$, and the magnetic susceptibility data suggested that ferromagnetic interactions were operative between the neighboring iron centres. The author reported a mixed-valence manganese [2 × 2] grid, $[Mn^{III}_{2}Mn^{II}_{2}(L6)_{4}(H_2O)_2](PF_6)_2 \cdot CHCl_3 \cdot CH_3OH \cdot 1.5H_2O$ (H_2L6 = 2-[3-(2-hydroxyphenyl)-1*H*-pyrazol-5-yl]-6-pyridinecarboxylic acid ethyl ester), which also shows ferromagnetic interactions between the manganese(III) and manganese(II) ions.[16]

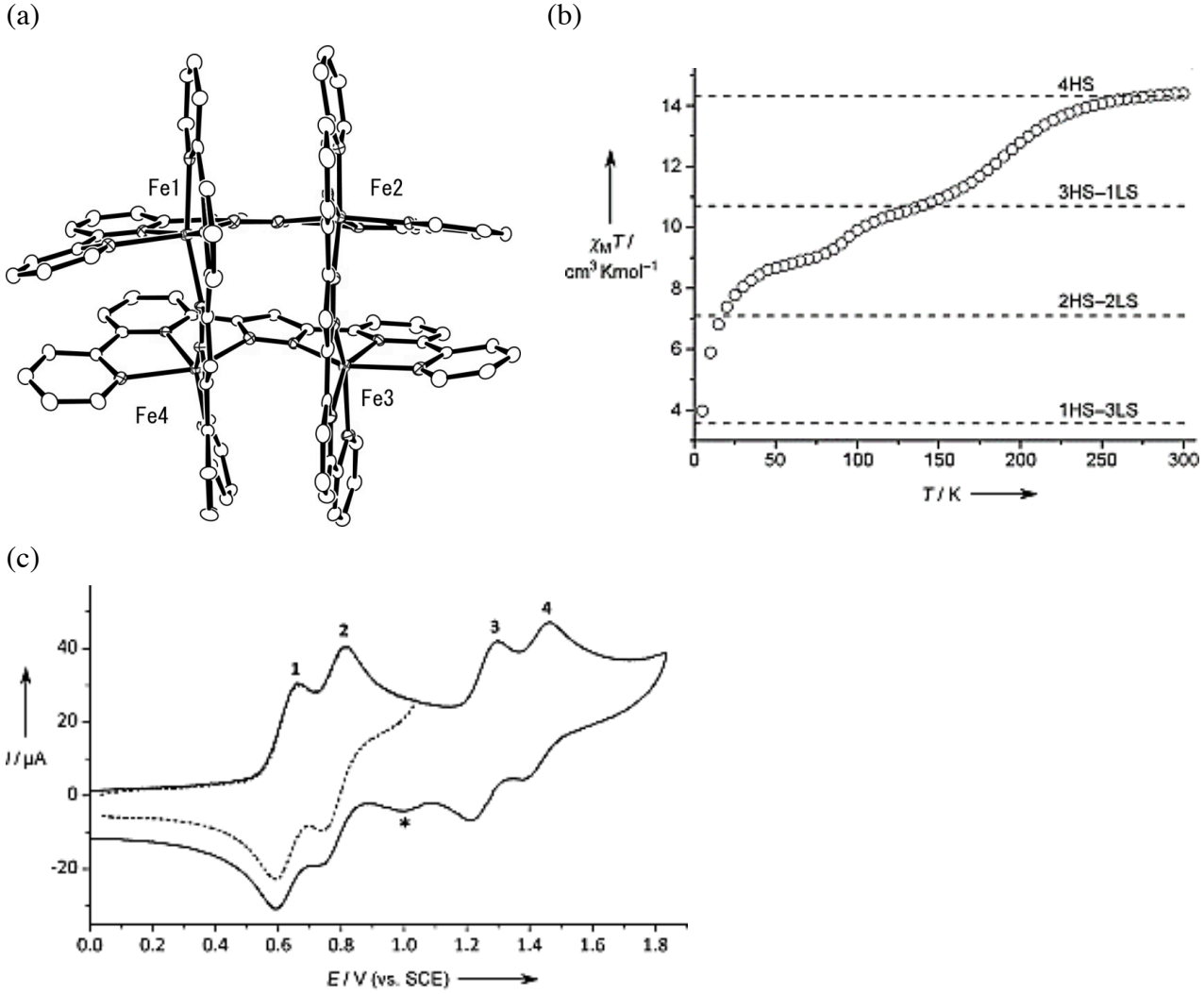

Figure 1.10: (a) The structures, (b) SCO behaviour, and (c) cyclic voltammogram of $[Fe^{II}_4(L5)_4](BF_4)_4 \cdot 4DMF$.

L. K. Thompson and his co-workers synthesized a manganese [3 × 3] grid-like cluster, $[Mn^{II}_9(L7)_6](ClO_4)_6 \cdot 3.75CH_3CN \cdot 11H_2O$, that shows multi-step redox behaviour. H. Oshio et al. and M.-L. Tong et al. also reported some similar poly-pyridyl-type [3 × 3] grid-like clusters based on copper. Oshio's copper(II) [3 × 3] grid, $[Cu^{II}_9(L8)_6](BF_4)_6 \cdot 1\text{-}PrOH \cdot 5H_2O$ (H_2L8 = 2,6-bis[5-(pyrid-2-yl)-1*H*-pyrazol-3-yl]pyridine), showed four-step redox behaviour and its two electron reduced grid was isolated (Figure 1.11).[17] X-ray structure analyses indicated that the divalent and mixed-valence complexes had similar [3 × 3] grid-like structures, but the Jahn-Teller distortions of the central copper(II) ions of the grids differed as a result of contrasting grid distortions. The related cobalt [3 × 3] grid, $[Co^{III}Cu^{II}_8(L8)_6](BF_4)_7 \cdot 8H_2O$, was also isolated and shown to be a mixed-valence and mixed-spin state cluster (corner; HS-cobalt(II), edge; LS-cobalt(II), and centre; LS-cobalt(III)), and it showed SMM behaviour.[18] L. K. Thompson and J.-M. Lehn group have intensively studied giant size grid compounds, such as [4 × 4], and [5 × 5] metal arrays.

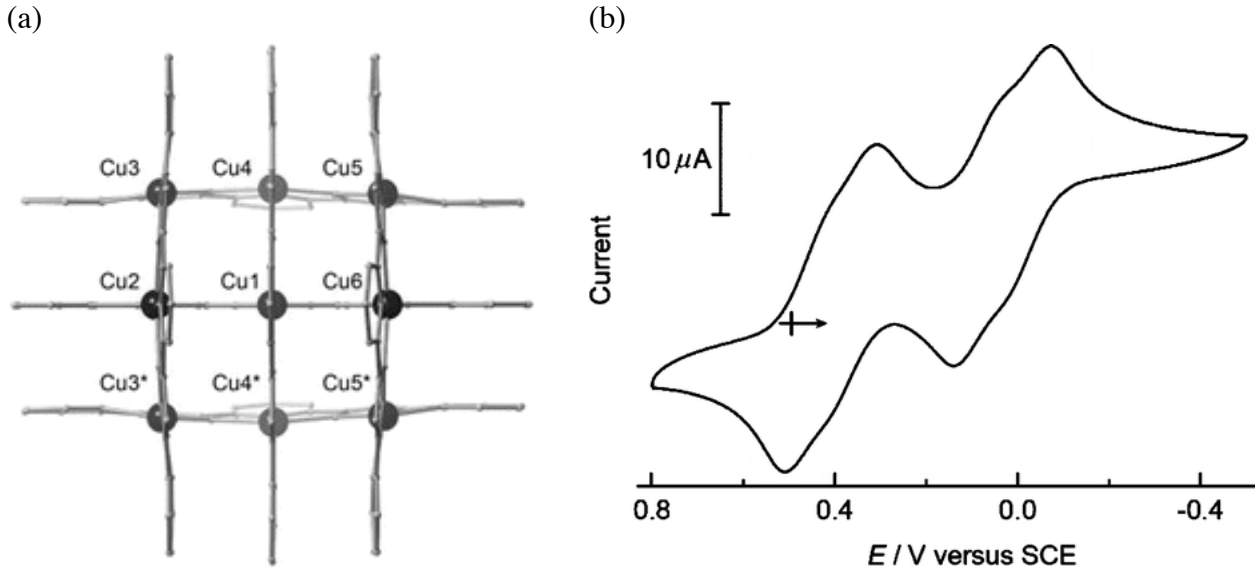

Figure 1.11: (a) The structure and (b) the cyclic voltammogram of $[Cu^{II}_9(L8)_6](BF_4)_6 \cdot$ 1-PrOH $\cdot$ $5H_2O$.

1.5 Coordination Compounds with Multi-stability

Bistability is when a physical property can be reversibly converted between two states with hysteresis under the application of external stimuli. Bistable molecules have, therefore, attracted intense research interest due to their potential applications in molecular switches and memory devices. Chromic meterials, spin-crossover phenomena, mixed-valence compounds, valence tautomerism, and ETCST (Electron-Transfer-Coupled Spin Transition) are major examples for bistable system. [19,20,21,22,23] Systems incorporating multiple bistable building units may display more than two stable phases when stimulated by heat or light, and have the potential to act as multi-responsive, multifaceted[24] or selective switches in nano-scale devices.[25] Approaches to the generation of multi-bistable systems include the crystallization of mononuclear SCO complexes in asymmetric packing environments,[26] the co-crystallization of different bistable molecules, and the combination of two or more bistable building blocks in one molecule in which the stabilization of an intermediate state depends upon the degree to which neighbouring chromophores are electronically coupled. $[Fe^{II}(dpp)_2][Ni(mnt)_2]_2 \cdot CH_3NO_2$ is a co-crystallized compound containing two kinds of bistable molecules (Figure 1.12 (a)). [27] $[Fe^{II}(dpp)_2]^{2+}$ (dpp = 2,6-di(1*H*-pyrazol-1-yl)pyridine) is a typical SCO-active complex cation and shows not only thermal but also light-induced bistability. $[Ni^{III}(mnt)_2]^-$ (mnt = maleonitriledithiolate) is a planar anion with $S = 1/2$ and can switch between a diamagnetic dimer state and a paramagnetic monomer state ($S = 1/2 \times 2$) when thermally stimulated, and also shows bistability. Both $[Fe^{II}(dpp)_2]^{2+}$ and $[Ni(mnt)_2]^-$ ions showed spin state conversion and five thermodynamically stable states were observed in the magnetic susceptibility measurements. $[\{Fe^{II}(bt)(NCS)_2\}_2bpym]$ is a molecule with two iron(II) SCO active sites, and showed two step thermal SCO behaviour, the steps corresponding to transitions on the different centres (Figure 1.12 (b)).[28] Interestingly, while 1342 nm laser irradiation of $[\{Fe^{II}(bt)(NCS)_2\}_2bpym]$ at low temperature induced 2LS to HS-LS conversion, 767.4 nm laser irradiation induced 2LS to 2HS state spin conversion, respectively.

(a)

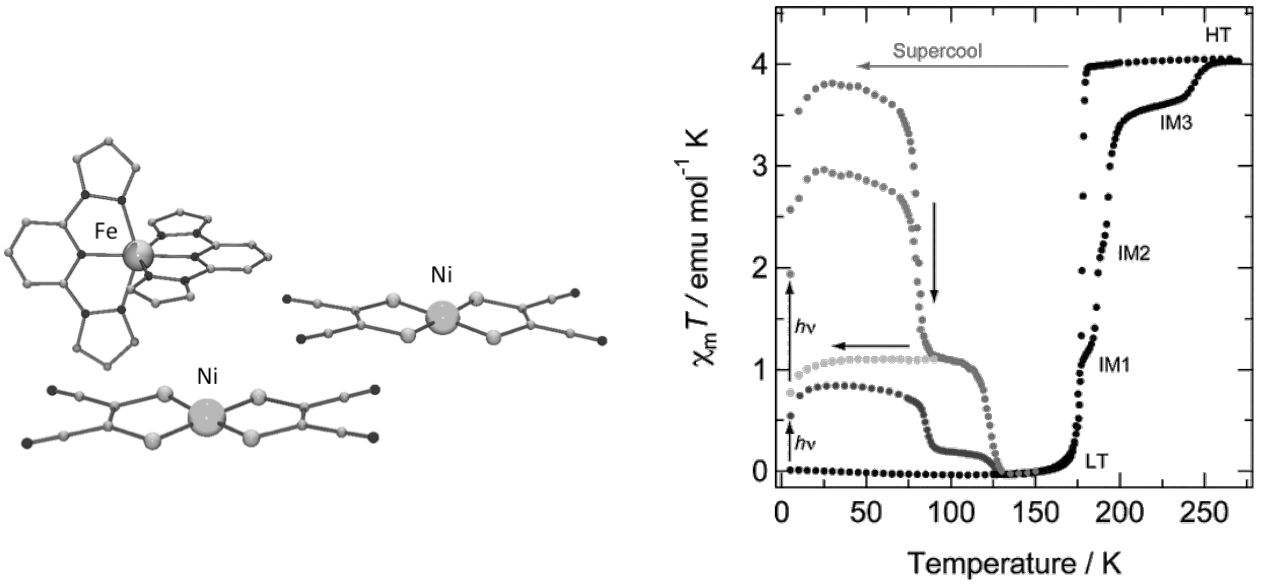

(b)

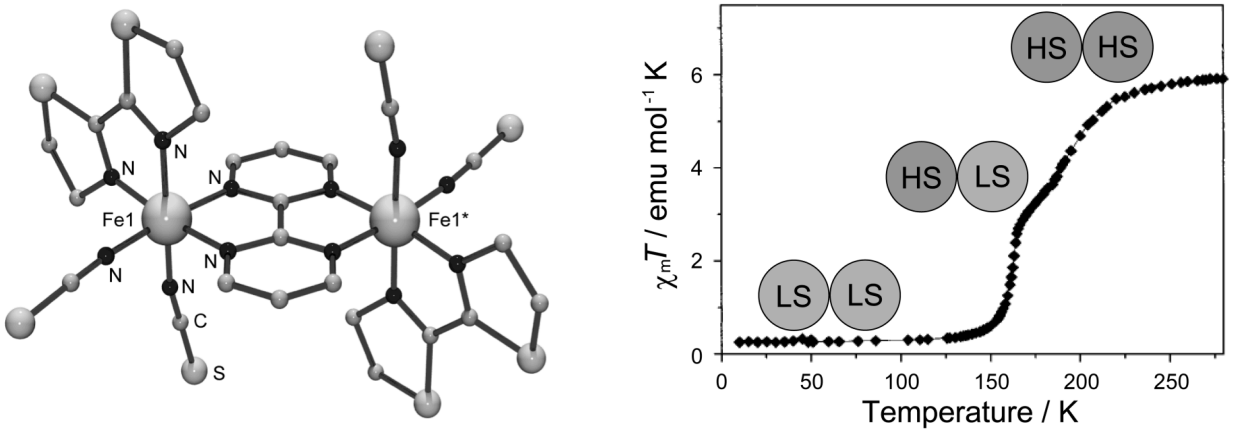

Figure 1.12: The examples of multi-stable complexes (left) and their magnetic data (right). (a) Co-crystallization of different bistable molecules ($[Fe^{II}(dpp)_2][Ni(mnt)_2]_2 \cdot CH_3NO_2$). (b) Combination of two bistable sites in one molecule ($[\{Fe^{II}(bt)(NCS)_2\}_2bpym]$).

---

[1] Baker W. A. & Bobonich H. M. Magnetic Properties of Some High-Spin Complexes of Iron(II). *Inorg. Chem.* **3**, 1184-1188 (1964).

[2] König E. & Madeja K. $^5T_2$-$^1A_1$ Equilibriums in some iron(II)-bis(1,10-phenanthroline) complexes. *Inorg. Chem.* **6**, 48-55 (1967).

[3] Hauser, A. Intersystem crossing in the $[Fe(ptz)_6](BF_4)_2$ spin crossover system (ptz = 1-propyltetrazole). J. Chem. Phys., 94, 2741-2748 (1991).

[4] Carbonera, C., Costa, J. S., Money, V. A., Elhaïk, J., Howard, J. A. K., Halcrow, M. H. & Létard, J.-F. Photomagnetic properties of iron(II) spin crossover complexes of 2,6-dipyrazolylpyridine and 2,6-dipyrazolylpyrazine ligands. *Dalton Trans.,* 3058-3066 (2006).

[5] Létard, J.-F., Guionneau, P., Nguyen, O., Costa, J. S., Marcen, S., Chastanet, G., Marchivie, M. & Capes, L. A Guideline of the Design of Molecular-Based Material with Long-Lived Photomagnetic Lifetimes. *Chem. Eur. J.*, **11**, 4582-4589 (2005).

[6] Duriska, M. B., Neville, S. M., Moubaraki, B., Cashion, J. D., Halder, G. J., Chapman, K. W.,

Balde, C., Létard, J.-F, Murray, K. S., Kepert, C. J. & Batten, S. R. A Nanoscale Molecular Switch Triggered by Thermal, Light, and Gest Perturbation. *Angew. Chem. Int. Ed.*, **48**, 2549-2552 (2009).
[7] D'Alessandro D. M. & Keene F. R. Intervalence Charge Transfer (IVCT) in Trinuclear and Tetranuclear Complexes of Iron, Ruthenium, and Osmium. *Chem. Rev.* **106**, 2270-2298 (2006).
[8] Robin, M. B., Day, P. Mixed-valence chemistry: a survey and classification. *Adv. Inorg. Chem. Radiochem.*, 10, 247–422 (1967).
[9] Nakamoto, T., Hanaya. M., Katoda, M., Endo, K., Kitagawa, S. & Sano, H. The Valence-Detrapping Phase Transition in a Crystal of the Mixed-Valence Trinuclear Iron Cyanoacetate Complex $[Fe_3O(O_2CCH_2CN)_6(H_2O)_3]$. *Inorg. Chem.*, **36**, 4347-4359 (1997).
[10] Newton, G. N., Tamashita, S., Hasumi, K., Matsuno, J., Yoshida, N., Nihei, M., Shiga, T., Nakano, M., Nojiri, H., Wernsdorfer, W. & Oshio, H. Redox-Controlled Magnetic $\{Mn_{13}\}$ Keggin Systems. *Angew. Chem. Int. Ed.*, **50**, 5716-5720 (2011).
[11] Youinou, M.-T., Rahmouni, N., Fischer, J & Osborn, J. A. Self-Assembly of a Cu_4 Complex with Coplanar Copper(I) Ions: Synthesis, Structure, and Electrochemical Properties. *Angew. Chem. Int. Ed. Engl.*, **39**, 733-735 (1992).
[12] Hanan, G. S., Volkmer, D., Schubert, U. S., Lehn, J.-M., Baum, G. & Fenske, D. Coordination Arrays: Tetranuclear Cobalt(II) Complexes with [2 × 2]-Grid Structure. *Angew. Chem. Int. Ed.*, **36**, 1842-1844 (1997).
[13] Breuning, E., Ruben, M., Lehn, J.-M., Renz, F., Garcia, Y., Ksenofontov, V., Cütlich, P., Wegelius, E. & Rissanen, K. Spin Crossover in a Supermolecular Fe_4^{II} [2 × 2] Grid Triggered by Temperature, Pressure, and Light. *Angew. Chem. Int. Ed.*, **39**, 2504-2507 (2005).
[14] Wu D.-Y., Sato, O., Einaga, Y. & Duan. C.-Y. A Spin-Crossover Cluster of Iron(II) Exhibiting a Mixed-Spin Structure and Synergy between Spin Transition and Magnetic Interaction. *Angew. Chem. Int. Ed.* **48**, 1475-1478 (2009).
[15] Schneider, B., Demeshko, S., Dechert, S. & Meyer, F. A Double-Switching Multistable Fe_4 Grid Complex with Stepwise Spin-Crossover and Redox Transition. *Angew. Chem. Int. Ed.* **49**, 9274-9277 (2010).
[16] Matsumoto, T., Shiga, T., Noguchi, M., Onuki, T., Newton, G. N., Hoshino, N., Nakano, M. & Oshio, H**.** Contrasting Magnetic of $[Mn^{III}_4]$ and $[Mn^{II}_2Mn^{III}_2]$ Squares. *Inorg. Chem.* **49**, 368-370 (2010).
[17] Sato, H., Miya, L., Mitsumoto, K., Matsumoto, T., Shiga, T., Newton, G. N. & Oshio, H. Multi-redox Active [3 × 3] Copper Grids. *Inorg. Chem.* **52**, 9714-9716 (2013).
[18] Shiga, T., Matsumoto, T., Noguchi, M., Onuki, T., Hoshiono, N., Newton, G. N., Nakano, N. & Oshio, H. Cobalt Antiferromangetic Ring and Grid Single-Molecule Magnet. *Chem. – Asian J.* **4**, 1660-1663 (2009).
[19] Nihei, M., Suzuki, Y., Kimura, N., Kera, Y. & Oshio, H. Bidirectional Photomagnetic Conversions in a Spin-Crossover Complex with a Diarylethene Moiety. *Chem. -A Eur. J.* **19**, 6946-6949 (2013).
[20] Rodríguez-Velamazán, J. A., González, M. A., Real, J. A., Castro, M., Muñoz, M. C., Gaspar, A. B., Ohtani, R., Ohba, M. Yoneda, K., Hijikata, Y., Yanai, N., Mizuno, M., Ando, H. & Kitagawa. S. A Switchable Molecular Rotator: Neutron Spectroscopy Study on a Polymeric Spin-Crossover Compound. *J. Am. Chem. Soc.*, 134, 5083-5089 (2012).
[21] Braun-Sand, S. B. & Wiest, O. Theoretical Studies of Mixed-Valence Transition Metal Complexes for Molecular Computing. *J. Phys. Chem. A* **107**, 285-291 (2003).
[22] Sato, O, Hayami, S., Gu, Z.-Z., Seki, K., Nakajima, R. & Fujishima, A. Photo-Induced Long-Lived Intramolecular Electron Transfer in a Co Valence Tautomeric Complex. *Chem. Lett.*, 874 (2001).
[23] Nihei, M., Sekine, Y., Suganami, N. & Oshio, H. Thermally Two-stepped Spin Transitions

Induced by Intramolecular Electron Transfers in a Cyanide-bridged Molecular Square. *Chem. Lett.* **39**, 978-979 (2010).

[24] Hoshino, N., Iijima, F., Newton, G. N., Yoshida, N., Shiga, T., Nojiri, H., Nakao, A., Kumai, R., Murakami, Y. & Oshio, H. Three-way switching in a cyanide-bridged [CoFe] chain. *Nature Chem.* **4**, 921-926 (2012).

[25] Rotaru, A., Dugay, J., Tan, R. P., Gural'skiy, I. A., Salmon, L., Demont, P., Carrey, L., Molnár, G., Respaud, M. & Bousseksou, A. Nano-electromanipulation of Spin Crossover Nanorods: Towards Switchable Nanoelectronic Devices. *Adv. Mater.* **25**, 1745-1749 (2013).

[26] Li, B., Wei, R.-J., Tao, J. Huang, R.-B., Zheng, L.-S. & Zheng, Z. Solvent-Induced Transformation of Single Crystals of a Spin-Crossover (SCO) Compound to Single Crystals with Two Distinct SCO Centers. *J. Am. Chem. Soc.* **132**, 1558–1566 (2010).

[27] Nihei, M., Tahira, H., Takahashi, N., Otake, Y., Yamamura, Y., Saito, K. & Oshio, H. Multiple Bistability and Tristability with Dual Spin-State Conversions in $[Fe(dpp)_2][Ni(mnt)_2]\cdot 2MeNO_2$. *J. Am. Chem. Soc.* **131**, 3553–3560 (2010).

[28] Gaspar, A. B., Muñoz, M. C. & Real, J. A. Dinuclear iron(II) spin crossover compounds: singular molecular materials for electronics. *J. Mater. Chem.* **16**, 2522-2533 (2006).

CHAPTER 2

Multi-bistability of Iron Grids

2.1 Introduction

Bistable materials have switchable electronic states that can be manipulated through the application of external stimuli and may have major applications in future technologies as molecular switches or components in memory storage devices.[1,2] Spin-crossover (SCO) is a phenomenon by which a transition metal centre can exhibit magnetic bistability, and it has been reported in a wide range of systems, from mononuclear complexes to infinite coordination polymers.[3,4] Transition metal ions with d^4 to d^7 electronic configurations may show reversible spin state transitions between their high spin (HS) and low spin (LS) states when stimulated by temperature, light, pressure or guest absorption/desorption;[5,6] simplicity and functionality that have made such materials excellent candidates as molecular switches or sensors.[7] Iron(II) complexes are the most commonly reported thermal SCO materials,[8] but there are examples of other SCO-active species based on chromium(II),[9] manganese(III),[10] cobalt(II)[11] and iron(III) ions,[12] amongst others.[13]

Iron complexes can also exhibit light-induced LS→HS state transition (LIESST: light-induced exited spin state trapping),[14] usually at low temperatures. In LIESST-active iron(II) complexes, the light-induced excited state is generated by excitation of the d-d or metal-to-ligand charge transfer (MLCT) absorption band, changing the spin state of the iron(II) ion from $S_{LS} = 0$ to $S_{HS} = 2$. The LS to HS transition is accompanied by a concomitant elongation (~0.2 Å) of the coordination bond lengths from ~1.9 Å to ~2.1 Å,[15,16] thus the reverse HS to LS thermal relaxation is energetically disfavoured at low temperature and the light-induced excited state can be trapped. A light-induced excited state can also be accessed in iron(III) SCO complexes, usually through excitation of the ligand-to-metal charge transfer (LMCT) band, but can be more difficult to trap; the shorter associated average (LS to HS) bond elongation of ~0.1 Å lowering the energy barrier to thermal relaxation.[17]

A molecule consisting of multiple bistable building units may display more than two stable states upon the application of external stimuli such as heat or light, exhibiting multi-bistability. Although challenging, the combination of serendipitous self-assembly and carefully planned molecular design can allow the generation of multi-bistable molecular systems, with potential to act as multi-state, multi-responsive or selective switches in nano-scale devices.[18] Approaches to the generation of multi-bistable systems range from the crystallization of mononuclear SCO complexes in asymmetric packing environments,[19] to the co-crystallization of different bistable molecules,[20] to the combination of two or more bistable building blocks in one molecule.[21] In the latter, the stabilization of an intermediate state is likely to depend upon the nature of the intramolecular electronic cooperativity, and thus ligand design is critical.

Multidentate or bridging ligands can mediate intramolecular cooperativity through their stereoscopic and electronic interactions; a phenomenon observed in dinuclear complexes[21] as well as tetranuclear squares[22,23] and grid-like complexes.[24,25,26] Grid-type clusters have been shown to

display properties such as multi-step redox behaviour[27,28] and single-molecule magnetism,[29] so are strong candidates for the generation of functional molecular materials. Multi-nuclear SCO complexes with substantial direct and indirect electronic interactions between metal centres, such as intervalence charge transfer (IVCT) and MLCT/LMCT respectively, can show multi-step thermal SCO as the geometric and electronic changes associated with their spin transitions have knock-on effects on the electronic states of the neighbouring metal ions. Step-wise thermal conversion does not, however, guarantee that multiple discrete phases can be accessed photochemically.

To address this, the author's strategy was to develop a molecule containing different SCO-active chromophores, which would allow the cluster to exist in three discrete light-accessible states at one temperature. The schematic detailing is shown in Figure 2.1, where HT, IM and LT are the high temperature, intermediate and low temperature (thermally-accessible) phases, and PP1 and PP2 are the first and second photo-induced phases respectively. The thermal multi-bistability is represented by the blue trace, which undergoes two hysteretic transitions, from HT to LT via an IM phase. The corresponding photochemical phases, PP1 and PP2, accessed by irradiation at wavelengths $h\nu_1$ and $h\nu_2$ are represented by green and red traces respectively. The schematic on the right shows how the different chromophores are excited by the different wavelengths of light.

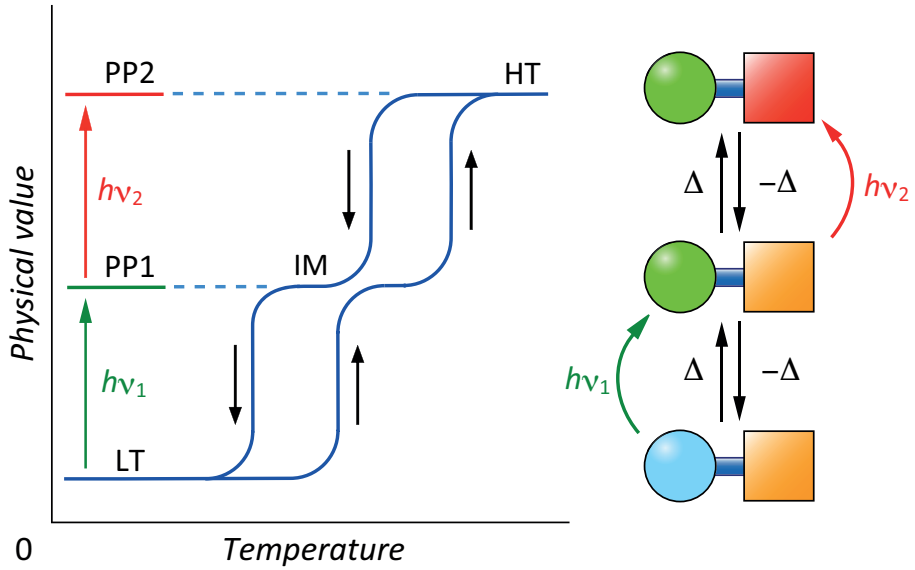

Figure 2.1: Representative plots and scheme of the adopted approach to the synthesis of selectively photo-excitable molecules, in which different SCO-active chromophores are incorporated into the same structure.

The author hypothesised that the ideal system for maximised intramolecular cooperativity and the best chance of site-selective excitation should consist of heterovalent metal centres bridged by aromatic ligands. To test this strategy, the author combined Fe^{II} and Fe^{III} SCO chromophores in an imidazolate-bridged grid architecture and found that, as hoped, the individual SCO centres could be selectively excited by different laser stimuli, thus creating the first example of site-selective spin state switching.

2.2 Experiments

Experimental Procedures

X-ray Crystallography: A single crystal was removed from the mother liquor, mounted on a glass rod and intensity data were collected using a Bruker SMART APEX II CCD system with Mo-Kα radiation ($\lambda = 0.71073$ Å). The structure was solved by direct methods and refined by full-matrix least-square techniques on F^2 using SHELXTL. The SQUEEZE program from the PLATON suite was employed to remove highly disordered solvent molecules from the crystallographic calculations on all data sets. The formulae were adjusted according to the assignment of the residual electron density calculated by SQUEEZE.

Magnetic Measurements: Magnetic susceptibility data with an applied magnetic field of 500 Oe were collected using a Quantum Design MPMS-5S SQUID magnetometer. The temperature dependence was measured at 3.0 K increments in settle mode. The scan rate of the temperature was fixed to 10.0 K/min, and each measurement was performed 30 s after the temperature had stabilized. Magnetic data were corrected for the diamagnetism of the sample holder and for the diamagnetism of the sample using Pascal's constants. In the light irradiation experiments, a small amount of sample was used to maximise the light conversion ratio. The sample was irradiated at 5 K by a DPSS laser (532 nm with 10 mW/cm^2, Opto Tech 532.200.KE.01 and 808 nm with 10 mW/cm^2, Intelite I808-120G-CAP) through an optical fiber (Newport F-MBD; 3 m length, 1.0 mm core size, 1.4 mm diameter). During irradiation, the magnetic moment was recorded at regular time intervals until saturation, after which point the light irradiation was stopped. The temperature dependence of magnetic susceptibility after light irradiation was measured using an applied magnetic field of 500 Oe and a scan rate of 0.1 K/min in scaning mode.

^{57}Fe Mössbauer spectra: Mössbauer experiments were carried out using a ^{57}Co/Rh source in a constant-acceleration transmission spectrometer (Topologic Systems) equipped with an Iwatani HE05/CW404 cryostat. The spectrometer was calibrated using standard α-Fe foil. All samples for Mössbauer experiments were obtained using ^{57}Fe enriched starting materials (95.5 %). In the light irradiation experiments, the sample was irradiated at 5 K by the DPSS lasers.

Single-crystal absorption spectroscopy: Single crystal absorption spectroscopy experiments were carried out using a specially designed spectrometer with a 25 cm grating monochromator (JASCO M25-GT) and an optical microscope. Light sources are a 150 W tungsten-halogen lamp and a 250 W xenon lamp, and detectors are photodiodes (Si and Ge) and a photomultiplier. These light sources and detectors were selected depending on the measured energy range. Samples were cooled in a conduction-type cryostat.

ESI-MS spectroscopy: ESI-MS spectra were recorded on a Waters UPLC/Synapt G2 HDMS.

Cyclic voltammetry: Cyclic voltammetry measurements were carried out in a standard one-compartment cell under a nitrogen atmosphere at 20 °C equipped with a platinum-wire counter electrode, an SCE reference electrode, and a glassy carbon (GC) working electrode using a BAS 620A electrochemical analyzer. The measurements were performed in acetonitrile with 0.1 M tetra-*n*-butylammonium hexafluorophosphate (*n*-Bu_4NPF_6) as the supporting electrolyte.

UV-Vis-NIR spectroscopy: UV-Vis-NIR absorption spectra were recorded on Shimadzu UV-3150 spectrometer. The variable temperature dependence of UV-Vis-NIR spectra was

measured on KBr pellet samples using the Shimadzu UV-3150 spectrometer equipped with a Unisoku USP-203-A cryostat.

Controlled potential spectroscopy: Controlled potential spectroscopy experiments were done in a 0.5 mm path length quartz cell under a nitrogen atmosphere. The BAS 620A electrochemical analyzer was used as a potentiostat. Electrochemical experiments were performed in a three-electrode cell containing a platinum-mesh working electrode, a platinum-wire counter electrode and the SCE reference electrode. Controlled potential spectra were recorded with the Shimadzu UV-3150 spectrometer. The measurements were performed in acetonitrile with 0.1 M tetra-*n*-butylammonium hexafluorophosphate as the supporting electrolyte.

NMR measurements: ^{1}H-NMR spectra were measured on a Bruker AVANCE400 spectrometer at room temperature. Chemical shifts in NMR were reported in ppm (δ), relative to the internal standard of tetramethylsilane (TMS). The signals observed were described as s (singlet), d (doublet), t (triplet), m (multiplets). The number of protons (n) for a given resonance is indicated as nH. Coupling constants are reported as *J* in Hz.

Elemental analysis: Elemental analyses were performed using a Perkin Elmer 2400 element analyzer.

Synthetic Procedures

All chemicals were used without further purification except when noted. Solvents and reagents were used as received from commercial suppliers or additionally distilled over calcium hydride (diglyme (bis(2-methoxyethyl)ether)) or over sodium/benzophenone (diethyl ether). The ^{57}Fe enriched samples for ^{57}Fe Mössbauer spectra measurements were prepared using metallic ^{57}Fe foils (95.5%).

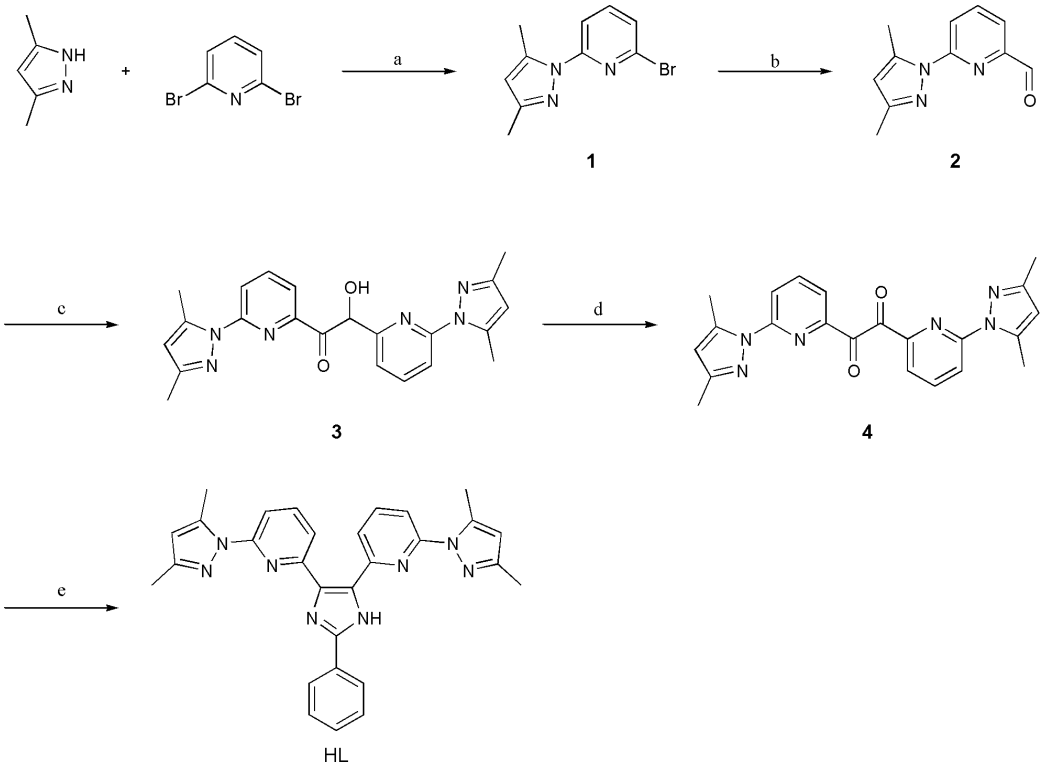

Scheme 2.1: Synthetic scheme of HL. a; Sodium, diglyme, 61%. b; *n*-BuLi, DMF, Et_2O, 61%. c; KCN (20 %mol), EtOH, H_2O, 92%. d; HNO_3, 59%. e; benzaldehyde, NH_4OAc, AcOH, 51%.

Preparation of 2-bromo-6-(3,5-dimethyl-1*H*-pyrazol-1-yl)pyridine (1)

A solution of 3,5-dimethyl-1*H*-pyrazol (8.00 g, 83.2 mmol) in anhydrous diglyme (200 cm^3) was stirred at 70 °C with sodium (1.80 g, 79.0 mmol) until the metal dissolved. To this solution was added 2,6-dibromopyridine (20.0 g, 84.4 mmol) in one portion. The resulting mixture was stirred at 60 °C for 42 hours. The solvent was removed, and water (200 cm^3) was added. A crude white precipitate was collected by filtration and dried. The solid was purified by column chromatography on silica gel (eluting with dichloromethane) to give **1** (12.2 g, 48.3 mmol, 61 % yield) as a crystalline white solid: ^{1}H-NMR ($CDCl_3$) δ 7.84 (d, 1H, J = 8.0 Hz), 7.60 (dd, 1H, J = 7.8 Hz), 7.29 (d, 1H, J = 7.2 Hz), 5.99 (s, 1H), 2.65 (s, 3H), 2.28 (s, 3H). Anal. (calc.) for $C_{10}H_{10}N_3Br$ (**1**): C, 47.81 (47.64); H, 4.07 (4.00); N, 16.69 (16.67)%.

Preparation of 6-(3,5-dimethyl-1*H*-pyrazol-1-yl)-2-pyridinecarboxaldehyde (2)

1 (10.1 g, 40.0 mmol) was dissolved in anhydrous diethyl ether (150 cm^3) under a nitrogen atmosphere. The solvent was cooled down to -78 °C and *n*-buthyl lithium (2.6 M in hexane) (15.4

cm^3, 40.0 mmol) was added slowly, keeping under -60 °C. After stirring for one hour at -78 °C, anhydrous *N*,*N*-dimethylformamide (3.37 cm^3, 44.0 mmol) was added, ensuring that the reaction temperature did not exceed -70 °C. The mixture was stirred for one further hour at -78 °C, before the reaction was quenched by the addition of 6 M hydrochloric acid. (15 cm^3). The organic phase was collected and dried over anhydrous magnesium sulfate. After evaporating the solvent, the residue was purified by column chromatography on a silica gel (eluting with dichloromethane/ethyl acetate = 20: 1) to give **2** (4.94 g, 24.5 mmol, 61 % yield) as a crystalline white solid: ^{1}H-NMR ($CDCl_3$) δ 10.02 (s, 1H), 8.16 (d, 1H, J = 8.4 Hz), 7.95 (dd, 1H, J = 7.6 Hz), 7.80 (d, 1H, J = 7.2 Hz), 6.05 (s, 1H), 2.75 (s, 3H), 2.31 (s, 3H). Anal. (calc.) for $C_{11}H_{11}N_3O$ (**2**): C, 65.43 (65.66); H, 5.61 (5.51); N, 20.56 (20.88)%.

Preparation of 1,2-bis[6-(3,5-dimethyl-1*H*-pyrazol-1-yl)pyrid-2-yl]-2-hydroxyetanone (3)

2 (4.94 g, 24.5 mmol) was dissolved in ethanol (100 cm^3) and an aqueous solution (10 cm^3) of potassium cyanide (325 mg, 5.00 mmol) was added while the mixture was stirred. A yellow precipitate was collected by filtration and washed with a small amount of water and ethanol. After drying, the crystalline yellow solid of **3** (4.42 g, 11.3 mmol, 92 % yield) was obtained: ^{1}H-NMR ($CDCl_3$) δ 12.01 (s, 2H), 7.95 (dd, 2H, J = 8.0 Hz), 7.81 (d, 2H, J = 7.8 Hz), 7.66 (d, 2H, J = 8.0 Hz), 6.07 (s, 2H), 2.59 (s, 6H), 2.32 (s, 6H). Anal. (calc.) for $C_{22}H_{22}N_6O_2$ (**3**): C, 65.53 (65.66); H, 5.60 (5.51); N, 20.73 (20.88)%.

Preparation of bis-[6-(3,5-dimethyl-1*H*-pyrazol-1-yl)pyrid-2-yl]glyoxal (4)

3 (4.42 g, 11.3 mmol) was dissolved in concentrated nitric acid (10 cm^3). After the evolution of nitrogen dioxide gas had subsided, the solution was neutralized with a saturated aqueous solution of potassium hydroxide. A precipitate was collected by filtration and purified by column chromatography on silica gel (eluting with dichloromethane/ethyl acetate = 20:1) to give **4** (2.68 g, 6.69 mmol, 59 % yield) as a pale yellow green solid: ^{1}H-NMR ($CDCl_3$) δ 8.20-8.18 (m, 2H), 8.00-7.99 (m, 4H), 5.86 (s, 2H), 2.22 (s, 6H), 2.11 (s, 6H). Anal. (calc.) for $C_{22}H_{20}N_6O_2$ (**4**): C, 66.04 (65.99); H, 5.12 (5.03); N, 20.98 (20.99)%.

Preparation of 2-phenyl-4,5-bis[6-(3,5-dimethyl-1*H*-pyrazol-1-yl)pyrid-2-yl]- 1*H*-imidazole (HL)

4 (2.68 g, 6.69 mmol), benzaldehyde (743 mg, 7.00 mmol) and ammonium acetate (1.85 g, 24.0 mmol) were dissolved in acetic acid (80 cm^3) and refluxed for sixteen hours before cold water was added and the mixture was neutralized by addition of saturated sodium hydroxide solution. The resulting precipitate was extracted into dichloromethane, and the organic phase was dried over anhydrous magnesium sulfate. The solvent was removed in *vacuo*, and the residue was purified by alumina column chromatography (activity stage I, eluting with dichloromethane then methanol) to give HL (1.65 g, 3.38 mmol, 51 % yield) as a white solid: ^{1}H-NMR ($CDCl_3$) δ 11.16 (s, 1H), 8.20 (d, 1H, J = 7.6 Hz), 8.03 (d, 2H, J = 7.2 Hz), 7.00 (d, 1H, J = 7.6 Hz), 7.91 (dd, 1H, J = 8.0 Hz), 7.78 (d, 1H, J = 8.0 Hz), 7.61 (dd, 1H, J = 7.6 Hz), 7.50 (d, 1H, J = 7.6 Hz), 7.49 (dd, 2H, J = 7.4 Hz), 7.42 (dd, 1H, J = 7.4 Hz), 6.06 (s, 1H), 5.93 (s, 1H), 2.66 (s, 3H), 2.32 (s, 6H), 2.28 (s, 3H). Anal. (calc.) for $C_{29}H_{26}N_8$ (HL): C, 71.31 (71.59); H, 5.60 (5.39); N, 22.59 (23.03)%.

Preparation of $[Fe^{II}_4(L)_4](BF_4)_4 \cdot 2CH_3CN$ ($[Fe^{II}_4] \cdot 2CH_3CN$)

HL (97.3 mg, 0.20 mmol) in acetonitrile (5.0 cm^3) was added to $Fe(BF_4)_2 \cdot 6H_2O$ (67.5 mg, 0.20 mmol) in acetonitrile (5.0 cm^3). Diethyl ether was allowed to diffuse into the solution, resulting in the formation of orange blocks and yellow needle crystals. The crystals were then washed with methanol, and the yellow crystals removed. The orange crystals of $[Fe^{II}_4] \cdot 2CH_3CN$ were collected by filtration (31.5 mg, 0.013 mmol, 25 % yield). Anal. (calc.) for $C_{116}H_{100}N_{32}B_4F_{16}Fe_4$ ($[Fe^{II}_4]$): C, 55.32 (55.45); H, 4.31 (4.01); N, 17.70 (17.84)%.

Preparation of $[Fe^{III}_2Fe^{II}_2(L)_4](BF_4)_6 \cdot 6CH_3NO_2 \cdot (C_2H_5)_2O \cdot 4H_2O$
($[Fe^{III}_2Fe^{II}_2] \cdot 6CH_3NO_2 \cdot (C_2H_5)_2O \cdot 4H_2O$)

Excess amount of $AgBF_4$ (12.0 mg, 0.062 mmol) was added to a nitromethane (5.0 cm^3) solution of $[Fe^{II}_4]$ (31.5 mg, 0.013 mmol). The mixture was stirred for fifteen minutes at 50 °C, cooled to room temperature, and the precipitate (silver) removed by filtration. Diethyl ether was allowed to diffuse into the filtrate, resulting in the formation of dark red rhombic crystals of $[Fe^{III}_2Fe^{II}_2] \cdot 6CH_3NO_2 \cdot (C_2H_5)_2O \cdot 4H_2O$, which were collected by filtration (28.1 mg, 0.009 mmol, 74 % yield). Anal. (calc.) for $C_{123}H_{127}N_{35}B_6F_{24}Fe_4O_{11}$ ($[Fe^{III}_2Fe^{II}_2] \cdot 3CH_3NO_2 \cdot (C_2H_5)_2O \cdot 4H_2O$): C, 49.25 (48.99); H, 4.18 (4.24); N, 15.97 (16.26)%.

Table 2.1: Table of crystallographic parameters for complex $[Fe^{II}_4]$ and $[Fe^{III}_2Fe^{II}_2]$.

	$[Fe^{II}_4]$ (HT)	$[Fe^{II}_4]$ (IM)	$[Fe^{II}_4]$ (LT)	$[Fe^{II}_4]$ (LT)
T / K	293	190	100	18
Instrument	APEX2	APEX2	APEX2	APEX2
Formula	$C_{120}H_{106}B_4F_{16}Fe_4N_{34}$	$C_{120}H_{106}B_4F_{16}Fe_4N_{34}$	$C_{120}H_{106}B_4F_{16}Fe_4N_{34}$	$C_{120}H_{106}B_4F_{16}Fe_4N_{34}$
F.W.	2595.03	2595.03	2595.03	2595.03
Space Group	$P\bar{1}$ (No.2)	$P\bar{1}$ (No.2)	$P\bar{1}$ (No.2)	$P\bar{1}$ (No.2)
a / Å	14.8611(7)	14.800(4)	14.604(3)	14.586(2)
b / Å	15.5694(7)	15.418(5)	15.272(4)	15.288(2)
c / Å	25.3433(11)	50.701(15)	25.118(6)	25.069(4)
α / °	88.9160(10)	89.662(4)	89.533(3)	88.663(2)
β / °	89.2600(10)	88.980(4)	88.974(3)	88.935(2)
γ / °	84.3780(10)	80.578(4)	84.143(3)	84.150(2)
V / Å^3	5834.3(5)	11411(6)	5572(2)	5558.4(15)
Z	2	4	2	2
μ / mm^{-1}	0.580	0.593	0.607	0.609
λ / Å	0.71073	0.71073	0.71073	0.71073
$R1$ ($> 2\sigma$)	0.0446	0.0879	0.0644	0.0873
$wR2$ ($> 2\sigma$)	0.1002	0.2144	0.1658	0.2584

	$[Fe^{II}_4]$ (HT*) 532 nm	$[Fe^{II}_4]$ (HT*) 808 nm	$[Fe^{III}_2Fe^{II}_2]$ (250 K)	$[Fe^{III}_2Fe^{II}_2]$ (100 K)
T / K	18	18	250	100
Instrument	APEX2	APEX2	APEX2	APEX2
Formula	$C_{120}H_{106}B_4F_{16}Fe_4N_{34}$	$C_{120}H_{106}B_4F_{16}Fe_4N_{34}$	$C_{126}H_{136}B_6F_{24}Fe_4N_{38}O_{17}$	$C_{126}H_{136}B_6F_{24}Fe_4N_{38}O_{17}$
F.W.	2595.03	2595.03	3198.99	3198.99
Space Group	$P\bar{1}$ (No.2)	$P\bar{1}$ (No.2)	$C2/c$ (No.15)	$C2/c$ (No.15)
a / Å	14.780(3)	14.817(3)	30.44(3)	29.931(3)
b / Å	15.351(4)	15.320(3)	20.141(18)	19.6750(18)
c / Å	24.994(6)	24.960(3)	28.47(2)	28.022(3)
α / °	87.078(4)	86.955(3)	90	90
β / °	89.444(4)	89.287(3)	121.602(11)	121.5550(10)
γ / °	81.872(4)	81.204(3)	90	90
V / Å^3	5607(2)	5591(2)	14868(22)	14062(2)
Z	2	2	4	4
μ / mm^{-1}	0.604	0.602	0.486	0.514
λ / Å	0.71073	0.71073	0.71073	0.71073
$R1$[a]	0.1329	0.0557	0.0561	0.0635
$wR2$[b]	0.3140	0.1438	0.1466	0.1787

[a] $R1 = \sum | |F_o| - |F_c| | / \sum |F_o|$. [b] $wR2 = \{ \sum [w(F_o^2 - F_o^2)^2] / \sum [w(F_o^2)^2] \}^{1/2}$.

Table 2.2: Table of bond distances (Å) in complex $[Fe^{II}_4]$ and $[Fe^{III}_2Fe^{II}_2]$.

$[Fe^{II}_4]$ (HT, 293 K)		$[Fe^{II}_4]$ (IM, 190 K)			
Occupancy: 100 %		Occupancy: 35.5(8) %		Occupancy: 64.5(8) %	
Fe1-N30	2.141(2)	Fe1A-N4A	2.04(4)	Fe1B-N29B	2.121(19)
Fe1-N3	2.149(2)	Fe1A-N30A	2.05(5)	Fe1B-N3B	2.139(19)
Fe1-N4	2.153(2)	Fe1A-N3A	2.13(3)	Fe1B-N1B	2.152(17)
Fe1-N29	2.161(2)	Fe1A-N29A	2.25(3)	Fe1B-N4B	2.21(2)
Fe1-N1	2.202(2)	Fe1A-N1A	2.26(3)	Fe1B-N30B	2.21(3)
Fe1-N32	2.215(2)	Fe1A-N32A	2.28(2)	Fe1B-N32B	2.220(13)
Fe2-N5	2.119(2)	Fe2A-N5A	2.08(3)	Fe2B-N5B	2.119(15)
Fe2-N6	2.150(2)	Fe2A-N6A	2.08(3)	Fe2B-N6B	2.156(16)
Fe2-N11	2.151(2)	Fe2A-N11A	2.10(2)	Fe2B-N11B	2.164(11)
Fe2-N12	2.159(2)	Fe2A-N12A	2.175(19)	Fe2B-N12B	2.170(10)
Fe2-N8	2.204(2)	Fe2A-N8A	2.23(3)	Fe2B-N8B	2.176(15)
Fe2-N9	2.210(2)	Fe2A-N9A	2.29(2)	Fe2B-N9B	2.202(10)
Fe3-N20	2.141(2)	Fe3A-N14A	1.95(3)	Fe3B-N14B	1.884(13)
Fe3-N19	2.144(2)	Fe3A-N13A	1.973(19)	Fe3B-N19B	1.902(15)
Fe3-N13	2.146(2)	Fe3A-N17A	1.99(3)	Fe3B-N13B	1.965(9)
Fe3-N14	2.150(2)	Fe3A-N19A	2.01(3)	Fe3B-N20B	2.002(15)
Fe3-N17	2.196(2)	Fe3A-N20A	2.03(3)	Fe3B-N17B	2.004(15)
Fe3-N16	2.207(3)	Fe3A-N16A	2.04(2)	Fe3B-N16B	2.030(12)
Fe4-N21	2.111(2)	Fe4A-N24A	2.07(4)	Fe4B-N27B	2.05(2)
Fe4-N22	2.146(2)	Fe4A-N21A	2.10(4)	Fe4B-N28B	2.10(2)
Fe4-N27	2.148(2)	Fe4A-N22A	2.10(4)	Fe4B-N21B	2.14(2)
Fe4-N28	2.167(2)	Fe4A-N25A	2.22(3)	Fe4B-N22B	2.15(2)
Fe4-N24	2.200(2)	Fe4A-N28A	2.26(4)	Fe4B-N25B	2.160(17)
Fe4-N25	2.215(2)	Fe4A-N27A	2.29(4)	Fe4B-N24B	2.32(2)

[Fe^{II}_4] (IM, 190 K)				[Fe^{II}_4] (LT, 100 K)	
Occupancy: 46.9(3) %		Occupancy: 53.1(3) %		Occupancy: 55.4(4) %	
Fe1C-N1C	2.136(19)	Fe1D-N30D	2.102(13)	Fe1A-N4A	2.12(3)
Fe1C-N29C	2.136(14)	Fe1D-N3D	2.112(18)	Fe1A-N1A	2.15(2)
Fe1C-N4C	2.16(2)	Fe1D-N29D	2.141(12)	Fe1A-N29A	2.150(12)
Fe1C-N30C	2.164(16)	Fe1D-N4D	2.14(2)	Fe1A-N3A	2.173(16)
Fe1C-N3C	2.17(2)	Fe1D-N32D	2.221(17)	Fe1A-N30A	2.176(16)
Fe1C-N32C	2.277(17)	Fe1D-N1D	2.231(15)	Fe1A-N32A	2.198(12)
Fe2C-N6C	1.968(15)	Fe2D-N5D	2.118(17)	Fe2A-N8A	2.022(14)
Fe2C-N5C	2.03(2)	Fe2D-N11D	2.134(19)	Fe2A-N5A	2.07(3)
Fe2C-N11C	2.03(2)	Fe2D-N12D	2.148(12)	Fe2A-N6A	2.115(16)
Fe2C-N12C	2.074(15)	Fe2D-N6D	2.178(13)	Fe2A-N12A	2.120(9)
Fe2C-N8C	2.084(15)	Fe2D-N9D	2.188(13)	Fe2A-N11A	2.155(11)
Fe2C-N9C	2.130(15)	Fe2D-N8D	2.273(13)	Fe2A-N9A	2.245(11)
Fe3C-N19C	2.11(2)	Fe3D-N20D	2.14(2)	Fe3A-N19A	1.798(19)
Fe3C-N14C	2.13(2)	Fe3D-N13D	2.165(13)	Fe3A-N14A	1.946(9)
Fe3C-N20C	2.16(3)	Fe3D-N19D	2.17(2)	Fe3A-N13A	1.980(9)
Fe3C-N13C	2.175(14)	Fe3D-N17D	2.19(2)	Fe3A-N17A	1.985(18)
Fe3C-N17C	2.22(2)	Fe3D-N14D	2.189(18)	Fe3A-N20A	2.10(2)
Fe3C-N16C	2.240(18)	Fe3D-N16D	2.212(14)	Fe3A-N16A	2.118(11)
Fe4C-N27C	1.858(15)	Fe4D-N24D	1.974(18)	Fe4A-N22A	1.861(13)
Fe4C-N25C	1.886(14)	Fe4D-N21D	2.07(3)	Fe4A-N21A	1.96(2)
Fe4C-N22C	1.94(3)	Fe4D-N22D	2.12(3)	Fe4AN24A	1.968(14)
Fe4C-N21C	2.02(3)	Fe4D-N27D	2.138(16)	Fe4A-N27A	1.975(14)
Fe4C-N28C	2.065(13)	Fe4D-N28D	2.150(12)	Fe4A-N28A	2.024(13)
Fe4C-N24C	2.24(2)	Fe4D-N25D	2.315(14)	Fe4A-N25A	2.027(16)

$[Fe^{II}_4]$ (LT, 100 K)		$[Fe^{II}_4]$ (LT, 18 K dark)			
Occupancy: 44.6(4) %		Occupancy: 67.9(4) %		Occupancy: 32.1(4) %	
Fe1B-N30B	2.08(2)	Fe1A-N3A	2.101(14)	Fe1B-N32B	1.86(3)
Fe1B-N3B	2.09(2)	Fe1A-N4A	2.13(3)	Fe1B-N30B	2.06(5)
Fe1B-N29B	2.145(16)	Fe1A-N30A	2.14(2)	Fe1B-N1B	2.14(4)
Fe1B-N4B	2.15(3)	Fe1A-N29A	2.152(14)	Fe1B-N4B	2.20(6)
Fe1B-N1B	2.22(3)	Fe1A-N1A	2.219(17)	Fe1B-N29B	2.20(3)
Fe1B-N32B	2.257(17)	Fe1A-N32A	2.374(13)	Fe1B-N3B	2.22(3)
Fe2B-N11B	1.928(11)	Fe2A-N8A	2.119(12)	Fe2B-N11B	1.933(16)
Fe2B-N9B	1.946(13)	Fe2A-N12A	2.128(8)	Fe2B-N9B	1.936(18)
Fe2B-N6B	1.98(2)	Fe2A-N5A	2.130(14)	Fe2B-N5B	1.97(3)
Fe2B-N12B	2.004(11)	Fe2A-N6A	2.133(11)	Fe2B-N6B	2.01(3)
Fe2B-N5B	2.03(4)	Fe2A-N11A	2.161(8)	Fe2B-N12B	2.038(19)
Fe2B-N8B	2.226(17)	Fe2A-N9A	2.253(9)	Fe2B-N8B	2.25(3)
Fe3B-N14B	1.924(13)	Fe3A-N19A	1.880(16)	Fe3B-N16B	1.945(19)
Fe3B-N16B	1.961(11)	Fe3A-N14A	1.914(10)	Fe3B-N20B	1.96(2)
Fe3B-N20B	1.99(3)	Fe3A-N17A	1.972(14)	Fe3B-N19B	2.00(3)
Fe3B-N17B	2.05(2)	Fe3A-N13A	2.012(8)	Fe3B-N17B	2.09(3)
Fe3B-N13B	2.085(12)	Fe3A-N16A	2.040(11)	Fe3B-N13B	2.10(2)
Fe3B-N19B	2.11(3)	Fe3A-N20A	2.067(12)	Fe3B-N14B	2.14(3)
Fe4B-N27B	1.97(2)	Fe4A-N22A	1.907(9)	Fe4B-N21B	2.08(3)
Fe4B-N25B	2.08(2)	Fe4A-N27A	1.929(17)	Fe4B-N28B	2.12(4)
Fe4B-N28B	2.118(18)	Fe4A-N21A	1.989(14)	Fe4B-N27B	2.13(4)
Fe4B-N21B	2.14(3)	Fe4A-N25A	1.996(13)	Fe4B-N22B	2.13(2)
Fe4B-N22B	2.14(2)	Fe4A-N24A	2.016(12)	Fe4B-N25B	2.19(3)
Fe4B-N24B	2.175(17)	Fe4A-N28A	2.052(15)	Fe4B-N24B	2.24(3)

$[Fe^{II}_4]$ (HT*, 18 K, 532 nm)		$[Fe^{II}_4]$ (HT*, 18 K, 808 nm)	
Occupancy: 100 %		Occupancy: 100 %	
Fe1-N30	2.117(7)	Fe1-N30	2.124(2)
Fe1-N3	2.147(7)	Fe1-N4	2.143(3)
Fe1-N4	2.149(8)	Fe1-N3	2.145(2)
Fe1-N29	2.162(6)	Fe1-N29	2.174(2)
Fe1-N1	2.201(7)	Fe1-N1	2.207(3)
Fe1-N32	2.226(6)	Fe1-N32	2.212(2)
Fe2-N5	2.107(8)	Fe2-N5	2.115(3)
Fe2-N6	2.153(7)	Fe2-N11	2.159(3)
Fe2-N11	2.154(8)	Fe2-N6	2.159(3)
Fe2-N12	2.159(7)	Fe2-N12	2.163(3)
Fe2-N8	2.201(9)	Fe2-N8	2.199(3)
Fe2-N9	2.206(7)	Fe2-N9	2.212(2)
Fe3-N20	2.119(8)	Fe3-N20	2.121(3)
Fe3-N14	2.140(8)	Fe3-N14	2.135(3)
Fe3-N19	2.146(8)	Fe3-N13	2.146(3)
Fe3-N13	2.148(7)	Fe3N19	2.147(2)
Fe3-N17	2.208(9)	Fe3-N17	2.200(3)
Fe3-N16	2.214(8)	Fe3-N16	2.210(3)
Fe4-N21	2.118(8)	Fe4-N21	2.102(3)
Fe4-N27	2.138(7)	Fe4-N27	2.136(2)
Fe4-N22	2.149(7)	Fe4-N22	2.145(2)
Fe4-N28	2.159(6)	Fe4-N28	2.162(2)
Fe4-N24	2.193(7)	Fe4-N24	2.199(3)
Fe4-N25	2.201(7)	Fe4-N25	2.207(3)

$[Fe^{III}_2Fe^{II}_2]$ (250 K)		$[Fe^{III}_2Fe^{II}_2]$ (100 K)	
Fe1-N3	1.927(2)	Fe1-N3	1.916(2)
Fe1-N3	1.927(2)	Fe1-N3	1.916(2)
Fe1-N4	1.976(2)	Fe1-N4	1.960(2)
Fe1-N4	1.976(2)	Fe1-N4	1.960(2)
Fe1-N1	1.993(3)	Fe1-N1	1.969(2)
Fe1-N1	1.993(3)	Fe1-N1	1.969(2)
Fe2-N11	1.927(2)	Fe2-N11	1.909(2)
Fe2-N6	1.928(2)	Fe2-N6	1.913(2)
Fe2-N12	1.999(2)	Fe2-N12	1.976(2)
Fe2-N5	2.000(2)	Fe2-N8	1.977(2)
Fe2-N8	2.001(3)	Fe2-N5	1.979(2)
Fe2-N9	2.003(3)	Fe2-N9	1.989(2)
Fe3-N14A	1.807(13)	Fe3-N14	1.904(3)
Fe3-N14A	1.807(13)	Fe3-N14	1.904(3)
Fe3-N16A	1.88(2)	Fe3-N13	1.950(2)
Fe3-N16A	1.88(2)	Fe3-N13	1.950(2)
Fe3-N13	1.970(2)	Fe3-N16	1.961(3)
Fe3-N13	1.970(2)	Fe3-N16	1.961(3)
Fe3-N14B	2.028(11)		
Fe3-N14B	2.028(11)		
Fe3-N16B	2.074(17)		
Fe3-N16B	2.074(17)		

Table 2.3: The Σ(°)[a] of [Fe^{II}_4] and [$Fe^{III}_2Fe^{II}_2$].

[Fe^{II}_4]

Temperature	Fe1	Fe2	Fe3	Fe4	Occupancy
293 K	146.13(29)	151.90(29)	144.42(31)	152.65(29)	100 %
190 K (A)	141(5)	150.3(37)	99.7(38)	132.0(56)	35.5(8) %
190 K (B)	146.4(28)	148.5(18)	86.1(19)	163.6(31)	64.5(8) %
190 K (C)	148.7(26)	112.0(26)	143.1(30)	88.1(34)	46.9(3) %
190 K (D)	141.0(22)	164.5(21)	146.4(25)	151.5(29)	53.1(3) %
100 K (A)	143.6(30)	153.6(25)	66.3(23)	92.8(30)	55.4(4) %
100 K (B)	144.4(39)	100.2(32)	107.9(30)	121.8(40)	44.6(4) %
18 K (dark, A)	139.7(24)	151.2(14)	75.8(18)	92.4(24)	67.9(4) %
18 K (dark, B)	150(6)	99.0(34)	115.4(38)	138(5)	32.1(4) %
18 K (532 nm)	142.9(9)	155.0(10)	143.4(10)	151.9(9)	100 %
18 K (808 nm)	143.48(33)	156.61(35)	145.22(36)	153.37(34)	100 %

[$Fe^{III}_2Fe^{II}_2$]

Temperature	Fe5	Fe6	Fe7	Fe7 Occupancy
250 K	78.77(39)	82.75(37)	64.07(27)	48(2) %
			89.27(21)	52(2) %
100 K	78.56(37)	81.87(34)	79.42(40)	100 %

[a] Σ is the sum of the deviation of each of the 12 *cis* N-Fe-N angles from 90°.

$$\Sigma = \sum_{i=1}^{12} |90° - \theta_i|$$

2.3 Results and Discussion

Structures. The crystallographically determined structures of $[Fe^{II}_4]$ and $[Fe^{III}_2Fe^{II}_2]$ are shown in Figure 2.2. $[Fe^{II}_4]$ crystallized in the $P\bar{1}$ space group and temperature dependence of structural data were collected at 18 K (in a dark), 100 K, 190 K (in heating mode) and 293 K. The crystal data are summarized in Table 2.1. $[Fe^{II}_4]$ has a tetranuclear grid-like core, consisting of four crystallographically independent iron ions, ligands, and tetrafluorobrate anions. Thus, charge balance suggests that all iron ions are divalent. The ligands adopt bis-tridentate coordination modes, bridging the iron ions through their central imidazolate moieties, ensuring that all four iron ions are coordinated by two tridentate binding sites, resulting in N_6 coordination environments. Structural data collected at both 18 K (Figure 2.3 and Table 2.4) and 100 K (Figure 2.4 and Table 2.5) allowed the characterisation of the cluster in two partially occupied, overlaid configurations (A and B). Bond distances and angles indicated that Fe1A and Fe2A were HS and Fe3A and Fe4A were LS ions, while Fe1B and Fe4B were HS and Fe2B and Fe3B were in the LS state; a ratio confirmed by low temperature magnetic susceptibility and ^{57}Fe Mössbauer data (Figures 2.13 and 2.16, and Table 2.10). In both configurations the grid had a *cis*-2HS-2LS configuration, abbreviated as $[(HS\text{-}Fe^{II})_2(LS\text{-}Fe^{II})_2]$, similar to that described in the first crystallographically determined 2HS-2LS iron grid and the subsequent theoretical studies thereupon,[30,31] although more recently a *trans*-2HS-2LS grid has also been reported.[32] Increasing the measurement temperature from 100 K to 190 K, caused the *c*-axis to double in length, and the unit cell to contain two crystallographically independent sites, both of which were occupied by two overlaid cluster configurations (Figure 2.5 and Table 2.6).[33,34,35] At site 1, in both configurations A and B, the bond lengths and angles indicated that ion Fe3A/B was in the LS state, while all other ions were in the HS state. At the second site, in contrast, molecule C contained two LS ions at positions Fe2C and Fe4C, while all ions in molecule D were in the HS state. Overall, the IM phase can be represented by the average formula $[(HS\text{-}Fe^{II})_3(LS\text{-}Fe^{II})]$, a ratio confirmed by magnetic susceptibility and Mössbauer data (Figures 2.13 and 2.16, and Table 2.10). As the sample temperature was further increased to 293 K, the length of the *c*-axis changed to 25.389(2) Å, and the resultant unit cell contained only one complex unit. The average coordination bond lengths around the iron ions ($HS\text{-}Fe^{II}\text{-}N_{av}$ = 2.166(2) Å) suggested that all iron irons were in the HS state. The temperature dependent crystallographic analysis showed $[Fe^{II}_4]$ to display two-step intramolecular SCO behaviour whilst retaining single crystallinity.

$[Fe^{III}_2Fe^{II}_2]$ crystallized in the monoclinic space group *C*2/*c* at 100 K (Figure 2.2). The oxidation and spin states of the iron ions in $[Fe^{III}_2Fe^{II}_2]$ were confirmed by charge balance considerations, magnetic susceptibility measurements and Mössbauer spectra. The grid was diagonally bisected by a C_2 axis, resulting in three crystallographically independent iron ions, and suggesting that the homovalent ions were likely to be found on opposite corners. The Mössbauer spectrum of $[Fe^{III}_2Fe^{II}_2]$ collected at 100 K confirmed that LS-Fe^{III} and LS-Fe^{II} ions existed in a 1: 1 ratio in the grid and the observation of two LS-Fe^{III} doublets and one LS-Fe^{II} doublet suggested that the Fe^{III} ions were located on the crystallographically inequivalent Fe5 and Fe7 positions, that is, Fe5 and Fe7 = LS-Fe^{III}, and Fe6 = LS-Fe^{II} (Figure 2.17 and Table 2.11). The average coordination

bond lengths around the iron ions at 100 K were Fe5 = 1.948(3) Å, Fe6 = 1.957(3) Å and Fe7 = 1.940(3) Å, respectively, suggesting that all iron ions were in the low-spin state at 100 K. Increasing the data collection temperature to 250 K caused structural disorder around the Fe7 centre, indicative of incomplete single-site Fe^{III} spin transition, an observation in line with the Mössbauer spectra, in which a low-intensity HS-Fe^{III} doublet progressively appeared as temperature was increased (Figure. 2.6 and Table 2.7).

(a)

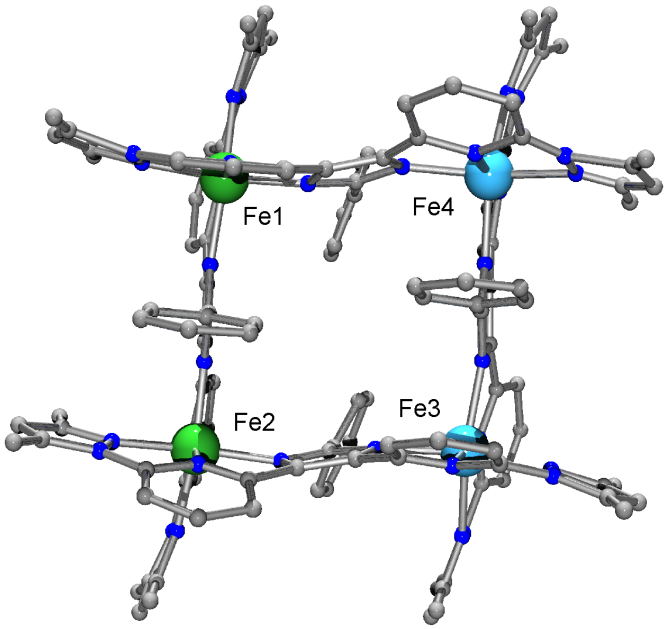

(b)

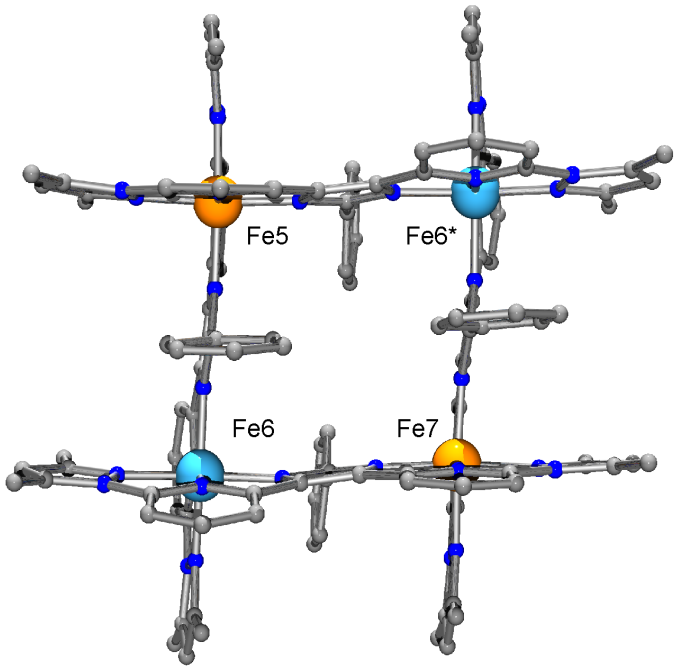

Figure 2.2: Ball and stick representations of the crystal structures of the homo- and heterovalent tetranuclear [2 × 2] grid-like complexes $[Fe^{II}_4]$ (Position A, a) and $[Fe^{III}_2Fe^{II}_2]$ (b) at 100 K. HS-Fe^{II} centres are shown in green; LS-Fe^{II}, sky-blue; LS-Fe^{III}, orange; C, grey and N, blue. For clarity, counteranions, hydrogen atoms and solvent molecules have been omitted.

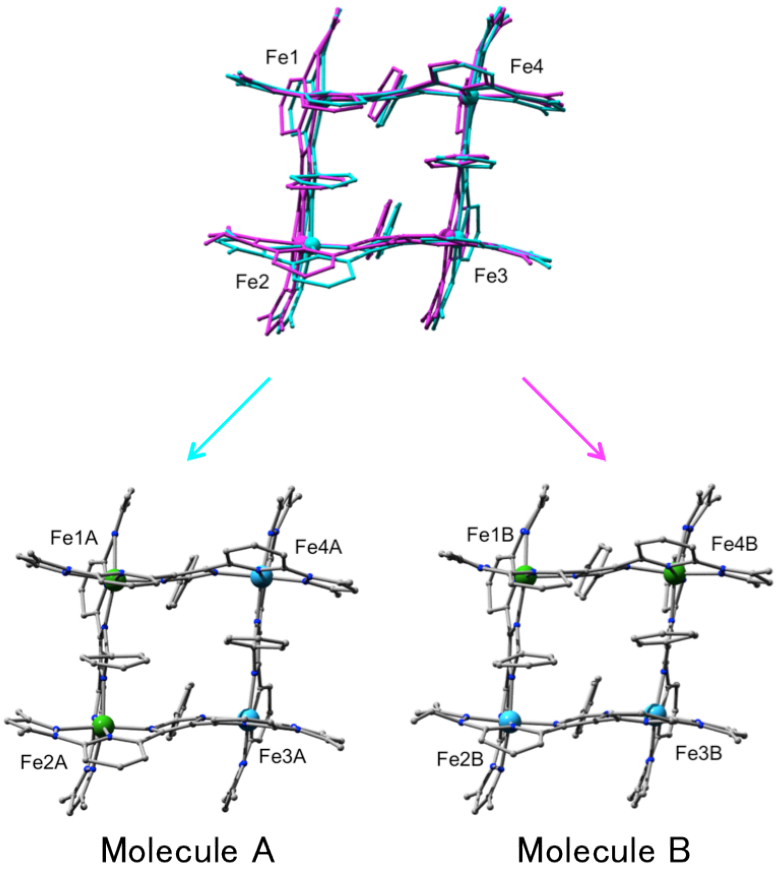

Figure 2.3: Crystal structure of [Fe^{II}_4] at 18 K (before irradiation). The structure could be split two positions and shown as molecule A (cyan) and B (magenta).

Table 2.4: The average coordination bond lengths around the iron centres, distortion of their coordination geometries (Σ), and assignment of spin state for [Fe^{II}_4] at 18 K.

Molecule A (occupancy: 67.9(4) %)

	Average Fe-N bond lengths [Å]	Σ [deg.]	Spin state
Fe1A	2.19(2)	139.7(24)	HS
Fe2A	2.154(11)	151.2(14)	HS
Fe3A	1.981(12)	75.8(18)	LS
Fe4A	1.982(14)	92.4(24)	LS

Molecule B (occupancy: 32.1(4) %)

	Average Fe-N bond lengths [Å]	Σ [deg.]	Spin state
Fe1B	2.11(4)	150(6)	HS
Fe2B	2.02(2)	99.0(34)	LS
Fe3B	2.04(3)	115.4(38)	LS
Fe4B	2.15(3)	138(5)	HS

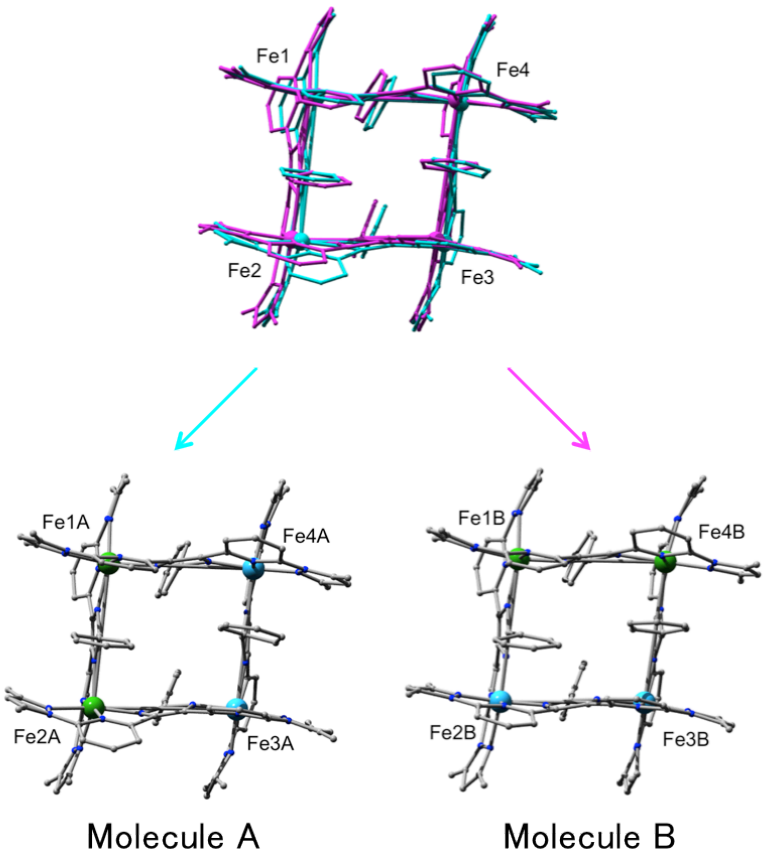

Figure 2.4: Crystal structure of [Fe^{II}_4] at 100 K. The structure could be split two positions and shown as molecule A (cyan) and B (magenta).

Table 2.5: The average coordination bond lengths around the iron centres, distortion of their coordination geometries (Σ), and assignment of spin state for [Fe^{II}_4] at 100 K.

Molecule A (occupancy: 55.4(4) %)

	Average Fe-N bond lengths [Å]	Σ [deg.]	Spin state
Fe1A	2.16(2)	143.6(30)	HS
Fe2A	2.16(2)	153.6(25)	HS
Fe3A	1.99(2)	66.3(23)	LS
Fe4A	1.97(2)	92.8(30)	LS

Molecule B (occupancy: 44.6(4) %)

	Average Fe-N bond lengths [Å]	Σ [deg.]	Spin state
Fe1B	2.16(2)	144.4(39)	HS
Fe2B	2.02(2)	100.2(32)	LS
Fe3B	2.02(3)	107.9(30)	LS
Fe4B	2.10(2)	121.8(40)	HS

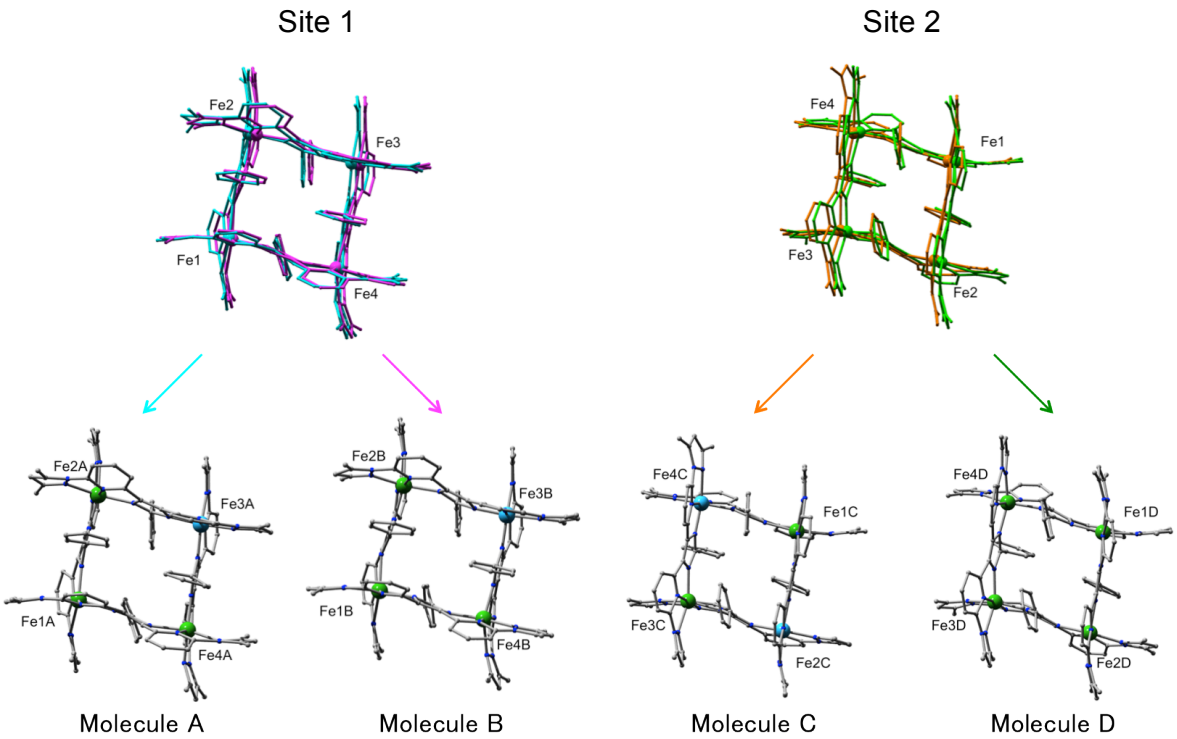

Figure 2.5: Crystal structure of $[Fe^{II}_4]$ at 190 K. The unit cell contains two crystallographically independent cation site, each of which is occupied by two superimposed molecules A (cyan) and B (magenta) at site 1, and C (orange), and D (green) at site 2.

Table 2.6: The average coordination bond lengths around the iron centres, distortion of their coordination geometries (Σ), and assignment of spin state for [Fe^{II}_4] at 190 K.

Molecule A (occupancy: 35.5(8) %)

	Average Fe-N bond lengths [Å]	Σ [deg.]	Spin state
Fe1A	2.17(3)	141(5)	HS
Fe2A	2.16(3)	150.3(37)	HS
Fe3A	1.99.(3)	99.7(38)	LS
Fe4A	2.17(4)	132.0(56)	HS

Molecule B (occupancy: 64.5(8) %)

	Average Fe-N bond lengths [Å]	Σ [deg.]	Spin state
Fe1B	2.18(2)	146.4(28)	HS
Fe2B	2.165(13)	148.5(18)	HS
Fe3B	1.965(13)	86.1(19)	LS
Fe4B	2.15(2)	163.6(31)	HS

Molecule C (occupancy: 46.9(3) %)

	Average Fe-N bond lengths [Å]	Σ [deg.]	Spin state
Fe1C	2.17(2)	148.7(26)	HS
Fe2C	2.05(2)	112.0(26)	LS
Fe3C	2.17(2)	143.1(30)	HS
Fe4C	2.00(2)	88.1(34)	LS

Molecule D (occupancy: 53.1(3) %)

	Average Fe-N bond lengths [Å]	Σ [deg.]	Spin state
Fe1D	2.16(2)	141.0(22)	HS
Fe2D	2.173(15)	164.5(21)	HS
Fe3D	2.18(2)	146.4(25)	HS
Fe4D	2.13(2)	151.5(29)	HS

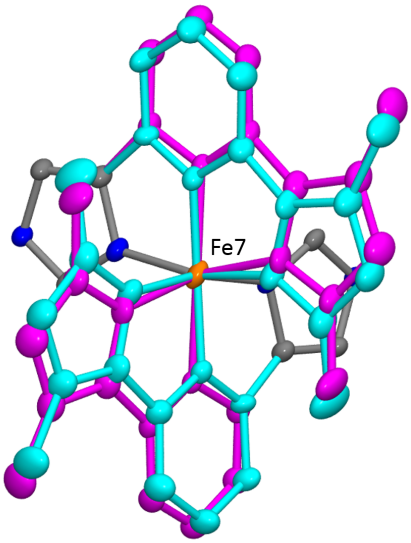

Figure 2.6: The crystallographically determined coordination environment around the Fe7 position of $[Fe^{III}_2Fe^{II}_2]$ at 250 K. The coordinating ligands are disordered into two positions, A (cyan) and B (magenta). Atoms are displayed as thermal ellipsoids at 30% probability.

Table 2.7: The average coordination bond lengths, distortion of their coordination geometries (Σ), assignment of spin state, and occupancy of the ligands around the Fe7 position of $[Fe^{III}_2Fe^{II}_2]$ at 250 K.

	Average Fe-N bond lengths [Å]	Σ [deg.]	Spin state	Occupancy [%]
Position A	1.89(2)	64.07(27)	LS	48(2)
Position B	2.02(2)	89.27(21)	HS	52(2)

Light-irradiation experiments were carried out on single crystals of $[Fe^{II}_4]$ and $[Fe^{III}_2Fe^{II}_2]$. Before irradiation in the dark at 18 K, the bond distances are similar to 100 K one and the structure was the *cis*-2HS-2LS configuration. Irradiation at 532 or 808 nm to a single crystal of $[Fe^{II}_4]$ caused the bond distances to increase to lengths and Σ similar to those seen at 293 K, characteristic of full $[(HS\text{-}Fe^{II})_2(LS\text{-}Fe^{II})_2] \rightarrow [(HS\text{-}Fe^{II})_4]$ transition (Tables 2.2 and 2.3). The unit cell volumes were also increased by LIESST effect. No structural change was, however, observed upon radiation of $[Fe^{III}_2Fe^{II}_2]$ crystals, perhaps due to their dark colour and impenetrability to light.

ESI-MS spectroscopy. The ESI-MS spectrum of $[Fe^{II}_4]$ was measured in acetonitrile and shown in (Figure 2.7 and Table 2.8). Main cluster peak was observed at 541.5 m/z, which was corresponded to $[Fe^{II}_4(L)_4]^{4+}$, and suggests that the grid-like core structure is stable in acetonitrile.

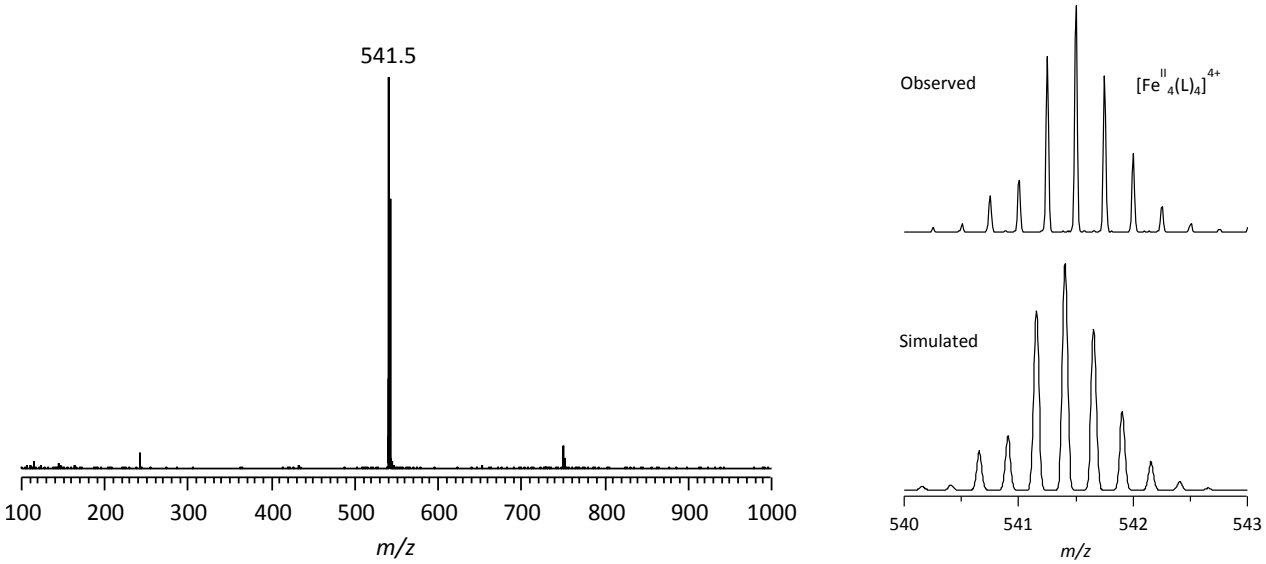

Figure 2.7: ESI-MS spectra on dissolved crystals of $[Fe^{II}_4]$ (main cluster peak of $[Fe^{II}_4(L)_4]^{4+}$ at 541.5 (541.5) *m/z*). Peak assignment is given in Table 2.8.

Table 2.8: Peak assignment for ESI-MS of $[Fe^{II}_4]$.

m/z	Formula
541.5	$[Fe^{II}_4(L)_4]^{4+}$

Electrochemical properties. Cyclic voltammetry measurements of $[Fe^{II}_4]$ were carried out in acetonitrile at 293 K (Figure 2.8 and Table 2.9). The cyclic voltammogram showed four quasi-reversible redox waves at $E_{1/2}$ = +0.52 V, +0.61 V, +0.90 V and +1.00 V (versus SCE) corresponding to the one-electron oxidation of the four iron centres. The comproportionation constant of the two-electron oxidized complex $\{Fe^{III}_2Fe^{II}_2\}^{6+}$ was 9.8×10^4,[36] suggesting that the mixed-valence species was relatively stable in acetonitrile.

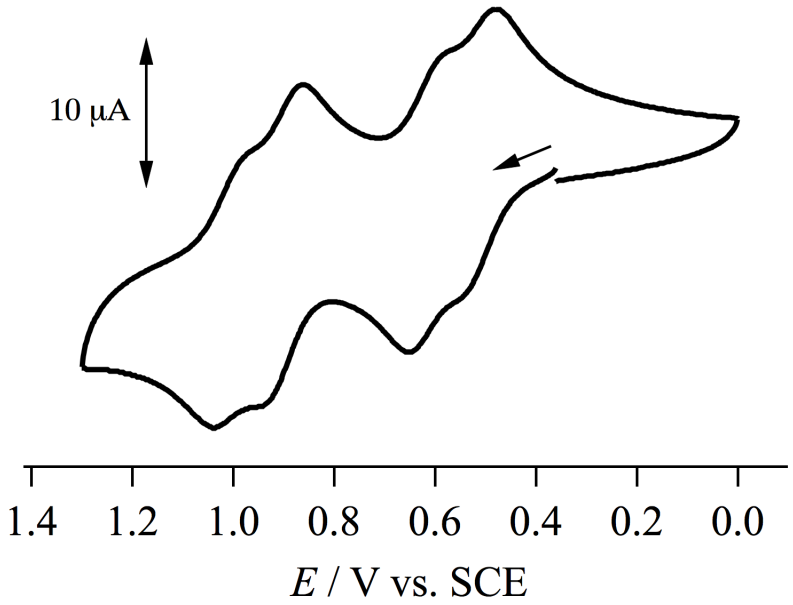

Figure 2.8: Cyclic voltammogram of $[Fe^{II}_4]$ in acetonitrile/0.1 M *n*-Bu_4NPF_6 referenced against SCE at a scan rate of 50 mVs^{-1}.

Table 2.9: CV data[a] for $[Fe_4]^{n+}$.

	E_{pa} (V)	E_{pc} (V)	$E_{1/2}$ (V)[b]
$\{Fe^{II}_4\}^{4+}$ / $\{Fe^{III}Fe^{II}_3\}^{5+}$	0.56	0.48	0.52
$\{Fe^{III}Fe^{II}_3\}^{5+}$ / $\{Fe^{III}_2Fe^{II}_2\}^{6+}$	0.65	0.57	0.61
$\{Fe^{III}_2Fe^{II}_2\}^{6+}$ / $\{Fe^{III}_3Fe^{II}\}^{7+}$	0.94	0.86	0.90
$\{Fe^{III}_3Fe^{II}\}^{7+}$ / $\{Fe^{III}_4\}^{8+}$	1.04	0.96	1.00

[a] vs. SCE at 293 K. [b] $E_{1/2} = (E_{pa} + E_{pc})/2$

Controlled potential spectroscopy. Controlled potential UV-Vis-NIR measurements were conducted on a solution of $[Fe^{II}_4]$ in acetonitrile to track the absorption bands associated with all accessible redox states. Initial oxidation from $\{Fe^{II}_4\}^{4+}$ to $\{Fe^{III}_2Fe^{II}_2\}^{6+}$ caused the LS-Fe^{II} MLCT band (λ_{max} = 501 nm) to weaken, while new absorption bands appeared at 864 nm and 2462 nm (Figure 2.9 (a)). Full oxidation to a $\{Fe^{III}_4\}^{8+}$ species caused the band at 2462 nm to disappear while that at 864 nm remained, indicating the absorption at 2462 nm to be an IVCT band between heterovalent iron ions, and the band at 864 nm to be the LS-Fe^{III} LMCT band (Figure 2.9 (b)).[37]

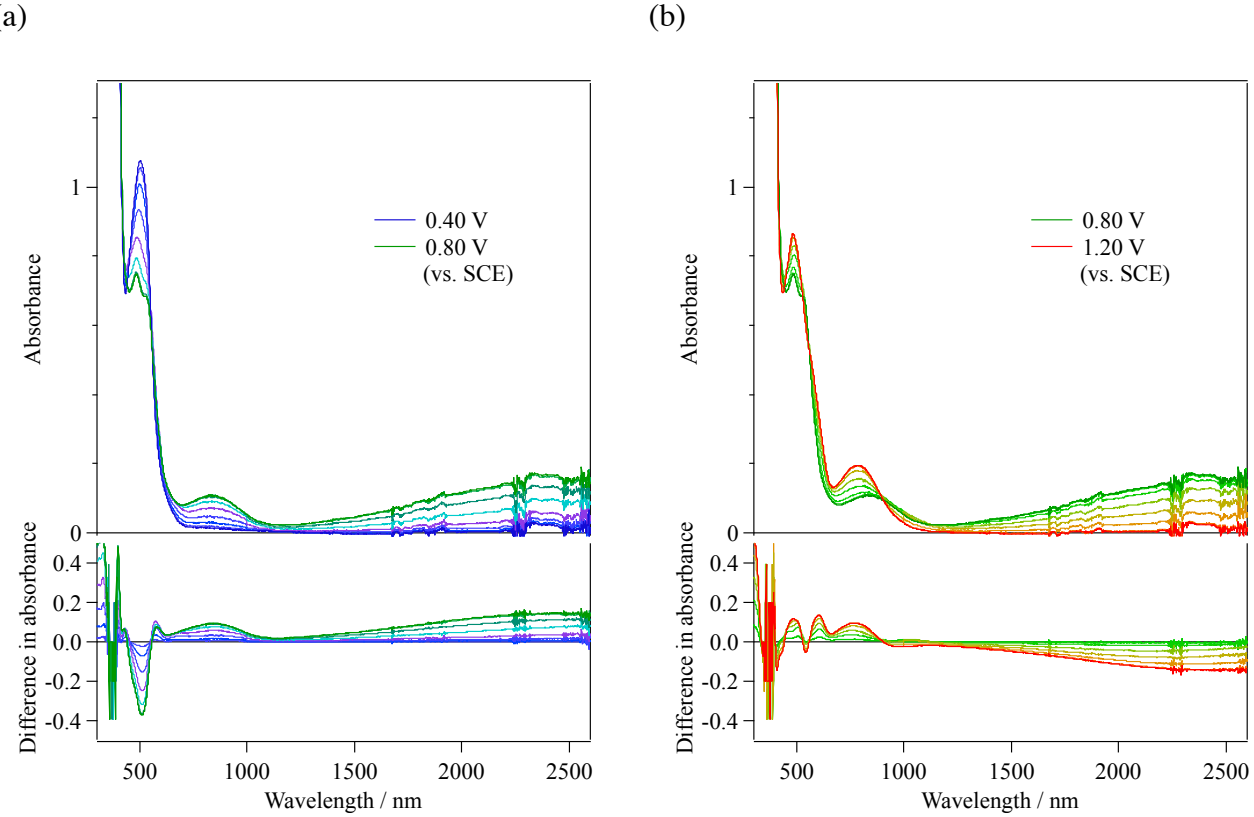

Figure 2.9: Controlled potential absorption spectra of $[Fe^{II}_4]$ between (a) 0.4 V-0.8 V (vs. SCE) and (b) 0.8 V-1.2 V in acetonitrile at 293 K.

UV-Vis-NIR spectroscopy. Absorption spectra of [Fe^{II}_4] and [$Fe^{III}_2Fe^{II}_2$] in acetonitrile at 293 K were shown in Figure 2.10. The band {4062 cm^{-1} (2462 nm), ε_{max}= 2800 $M^{-1}cm^{-1}$} of [$Fe^{III}_2Fe^{II}_2$] was assigned as an IVCT band between heterovalent iron ions. The pertinent delocalization parameters were obtained from Hush theory, based on ε_{max}= 1400 $M^{-1}cm^{-1}$ (two chromophores), ν_{max} = 4060 cm^{-1} (2462 nm), and $\Delta\nu_{1/2}$ = 1600 cm^{-1}, which yielded H_{ab} = 320 cm^{-1} and α^2 = 0.006 (or H_{ab} = 450 cm^{-1} and α^2 = 0.012 by disregarding the double degeneracy of the transition), indicative of a Robin-Day class II electron delocalized mixed-valence complex.[38]

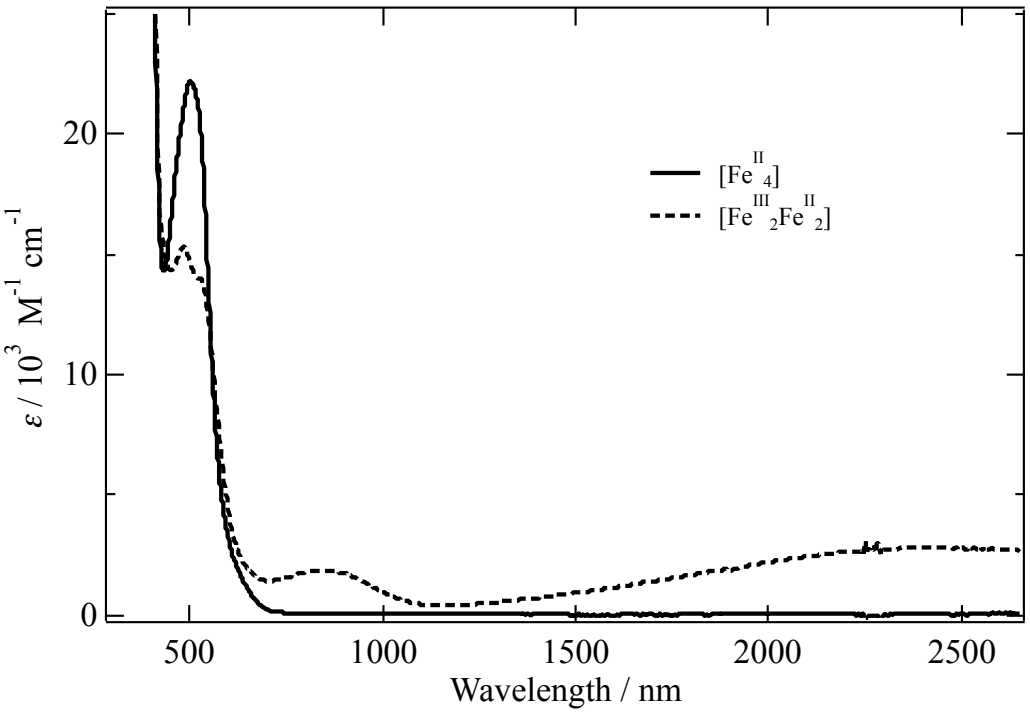

Figure 2.10: Absorption spectra of [Fe^{II}_4] and [$Fe^{III}_2Fe^{II}_2$] in acetonitrile at 293 K.

Temperature dependent absorption spectra of $[Fe^{II}_4]$ and $[Fe^{III}_2Fe^{II}_2]$ in solid state were shown in Figure 2.11. Spectra were collected on solid samples compressed into KBr pellets and measured in transmission mode. For $[Fe^{II}_4]$, LS-Fe^{II} MLCT band was observed (λ_{max} = 530 nm) at 100 K, and the band change to weak by heating. The spectra showed change even up to 373 K, suggesting that the LT state was stabilized in a pressed sample. For $[Fe^{III}_2Fe^{II}_2]$, LS-Fe^{II} MLCT band (*ca*. 500nm), LS-Fe^{III} LMCT band (*ca*. 850 nm) and IVCT band (*ca*. 2400 nm) were observed and did not show temperature dependency (Figure 2.11 (b)).

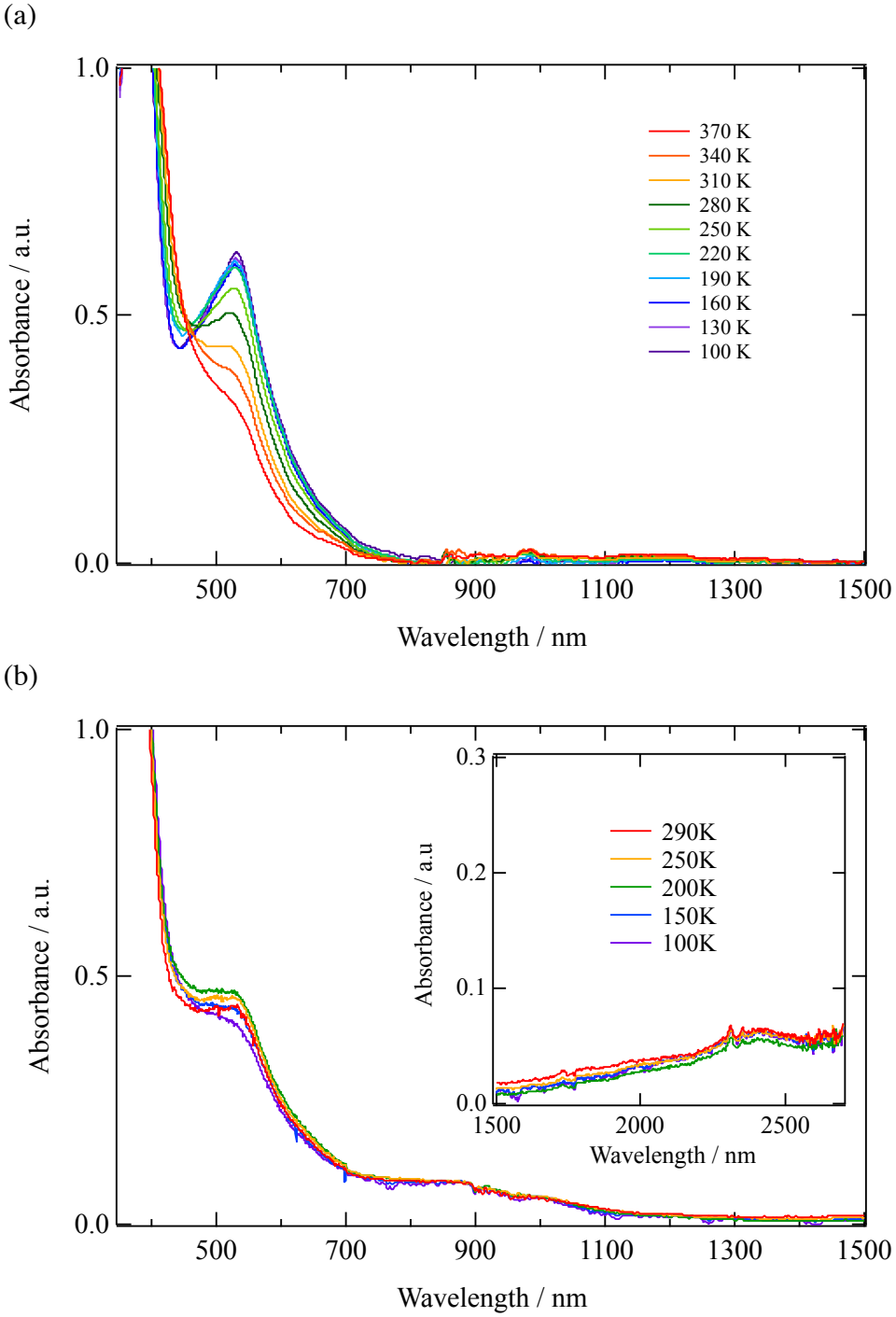

Figure 2.11: Solid state absorption spectra of $[Fe^{II}_4]$ (a) and $[Fe^{III}_2Fe^{II}_2]$ (b). Spectra were collected on solid samples compressed into KBr pellets and measured in transmission mode.

Single-crystal absorption spectroscopy. Single-crystals absorption spectra of $[Fe^{II}_4]$ were collected at 100 K and 293 K. The spectrum at 100 K shows the low energy edge of the LS-Fe^{II} MLCT band at high resolution (Figure 2.12). The MLCT absorption was found to extend to around 850 nm, overlapping with the HS-Fe^{II} d-d transition band ($^5T_{2g} \rightarrow {}^5E_g$). The LS-$Fe^{II}$ MLCT band was disappeared when the sample was heated up to 293 K.

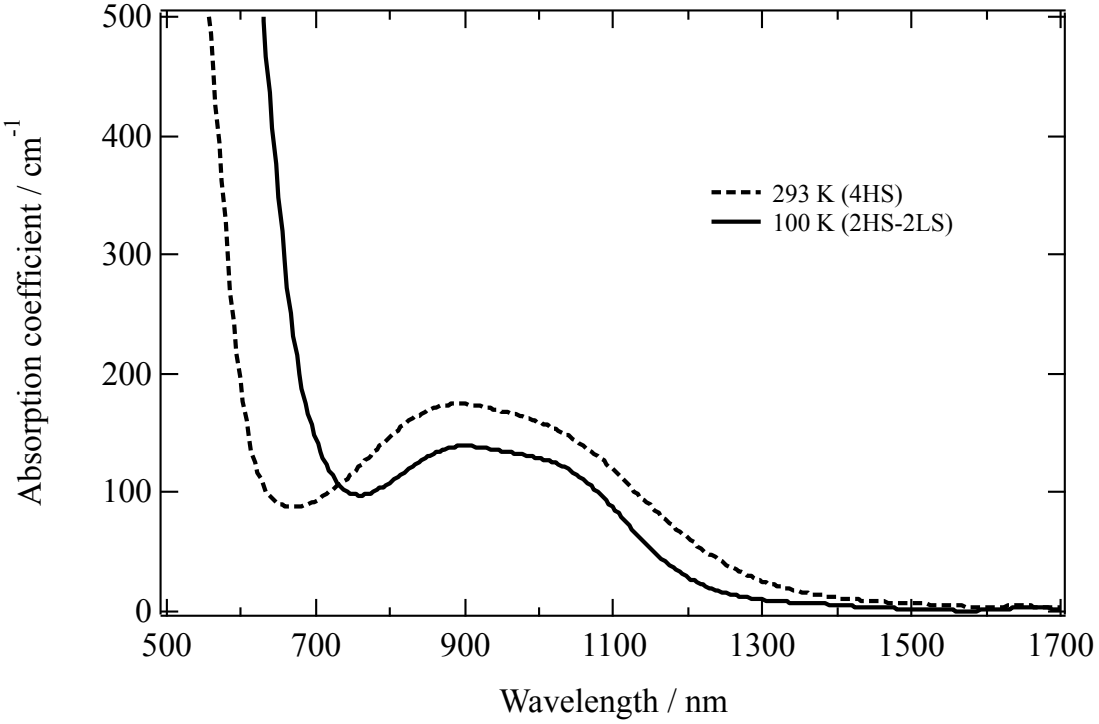

Figure 2.12: Single crystal absorption spectra of $[Fe^{II}_4]$ at 293 K and 100 K.

DC magnetic susceptibility. DC magnetic susceptibilities of crystalline sample of $[Fe^{II}_4]$ and $[Fe^{III}_2Fe^{II}_2]$ were measured in the temperature range of 5 – 300 K with applying magnetic field of 500 Oe (Figure 2.13). The $\chi_m T$ value of $[Fe^{II}_4]$ at 100 K (↑) was 6.89 emu mol^{-1} K, close to the spin only value of 6.63 emu mol^{-1} K (g = 2.10), calculated from the sum of the uncorrelated spins of two HS-Fe^{II} (S = 2) and two LS-Fe^{II} (S = 0) ions, as predicted. As the sample was heated, the $\chi_m T$ value rapidly increased. At 190 K (↑), the $\chi_m T$ plot showed a small step with a value of 10.57 emu mol^{-1} K, closely corresponding to the spin only value of 9.95 emu mol^{-1} K expected for an average of three HS-Fe^{II} ions and one diamagnetic LS-Fe^{II} centres per molecule. Upon further heating to 300 K, the magnetic susceptibility reached a plateau with a $\chi_m T$ value of 13.26 emu mol^{-1} K, suggesting that all iron ions were in their HS states above 250 K. Mössbauer measurements confirmed that the decrease in $\chi_m T$ values under 100 K were not due to SCO behaviour, indicating that antiferromagnetic interactions between the HS iron ions were likely to be responsible (Figure 2.16). Subsequent measurements in cooling mode echoed the two-step heating profile, but with a relatively wide thermal hysteresis. The thermal hysteresis and multistep phase transition mean that $[Fe^{II}_4]$ is a thermally multi-bistable molecule with the spin state conversions of $[(LS\text{-}Fe^{II})_2(HS\text{-}Fe^{II})_2] \rightleftarrows [(LS\text{-}Fe^{II})(HS\text{-}Fe^{II})_3] \rightleftarrows [(HS\text{-}Fe^{II})_4]$.

For $[Fe^{III}_2Fe^{II}_2]$, the $\chi_m T$ value at 100 K was 0.942 emu mol^{-1} K, closely matching the predicted value of 0.941 (g = 2.24) for two uncorrelated LS-Fe^{III} ions (S = 1/2) and two LS-Fe^{II} ions (S = 0). With heating, the $\chi_m T$ value increased gradually, reaching 2.36 emu mol^{-1} K at 300 K. Further heating led to some sample degradation so all measurements were carried out below 300 K. The susceptibility data suggests that thermal SCO occurred gradually above 200 K in $[Fe^{III}_2Fe^{II}_2]$, in agreement with the Mössbauer spectra, in which a low-intensity HS-Fe^{III} doublet appeared correspondingly (Figure 2.17).[39] The decrease in $\chi_m T$ values at low temperature indicates that antiferromagnetic interactions were operative between the LS-Fe^{III} ions. The LS-Fe^{II} ions in $[Fe^{III}_2Fe^{II}_2]$ show greater thermal stability than those in $[Fe^{II}_4]$, perhaps attributable to the increased distortion of the Fe^{II} coordination environments in $[Fe^{II}_4]$ (ave. $\Sigma_{LS\text{-}Fe^{II}}$ = 91.8(29)°, where Σ represents the sum of the deviation from 90° of the twelve *cis*-N-Fe-N angles around a metal centre)[40,41] compared to $[Fe^{III}_2Fe^{II}_2]$ at 100 K ($\Sigma_{LS\text{-}Fe^{II}}$ = 81.87(24)°) (Table 2.3).

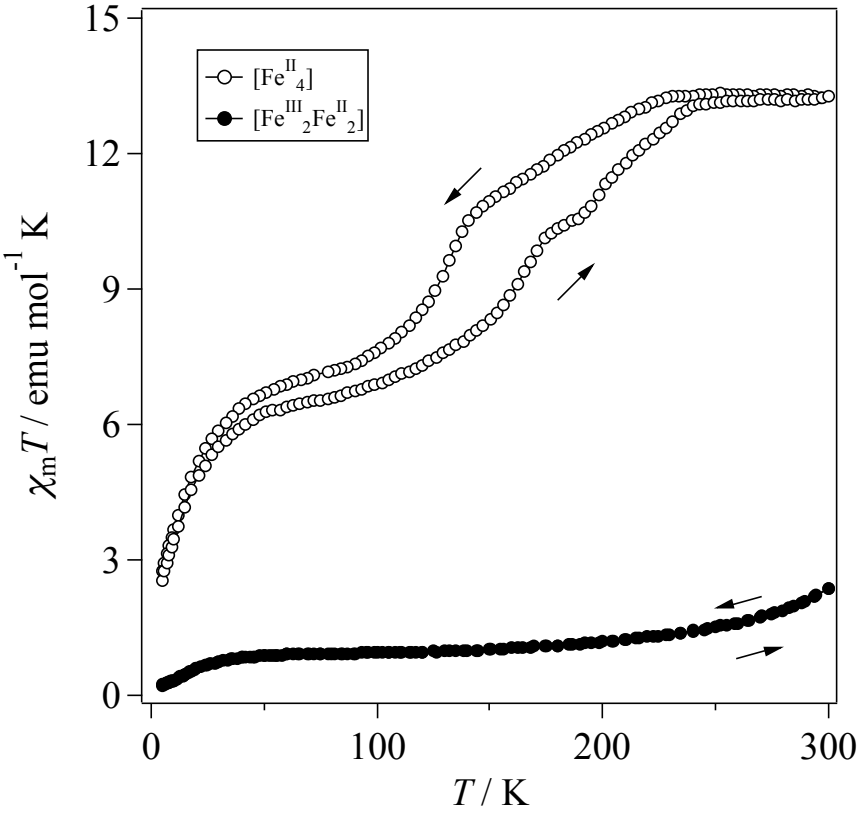

Figure 2.13: The thermal magnetic susceptibility data collected for $[Fe^{II}_4]$ (○) and $[Fe^{III}_2Fe^{II}_2]$ (●).

The combination of heterovalent iron chromophores within a cooperative SCO complex suggested that site and charge-specific LIESST behaviour may be accessible for the first time. To investigate the photoresponsivity of $[Fe^{II}_4]$ and $[Fe^{III}_2Fe^{II}_2]$ to different wavelengths of laser light, irradiation experiments were conducted inside the SQUID magnetometer. For the LIESST phenomenon to be observed, specific electronic absorption bands should be excited; usually d-d or MLCT for Fe^{II} and LMCT for Fe^{III}. UV-Vis-NIR measurements in solid state showed $[Fe^{II}_4]$ to have a broad MLCT band centred at λ_{max} = 530 nm and spreading to *ca*. 850 nm, while $[Fe^{III}_2Fe^{II}_2]$ had a separate LMCT band at 864 nm originating from its LS-Fe^{III} moieties (Figure 2.11 (a) and Figure 2.12). The combination of different absorption bands encouraged us to attempt site-selective LIESST excitation experiments. A microcrystalline sample of $[Fe^{II}_4]$ was irradiated using a 532 nm laser (10 mW/cm^2) at 5 K, leading to an initial decrease in the $\chi_m T$ value (Figure 2.14 (a)). The $\chi_m T$ value then increased rapidly to a maximum of 9.87 emu mol^{-1} K as the sample was heated to 56 K, indicating the occurrence of the LIESST effect. The photo-induced state then thermally relaxed to the initial phase upon further temperature increase. When 808 nm laser irradiation (10 mW/cm^2) was used, very similar behaviour was observed, attributable to excitation of the low energy tail of the broad LS-Fe^{II} MLCT band, the $\chi_m T$ value of the photo excited state reaching a maximum of 9.54 emu mol^{-1} K at 56 K.

For $[Fe^{III}_2Fe^{II}_2]$, a green light-induced excited state (gES) was accessed by irradiation with a 532 nm laser (10 mW/cm^2) at 5 K, which led to an increase in the $\chi_m T$ values, reaching a saturation value of 1.24 emu mol^{-1} K at 5 K after 4 hours (Figure 2.15). When the sample was then irradiated with red light (10 mW/cm^2) the $\chi_m T$ value increased to a second saturation level of 1.46 emu mol^{-1} K at 5 K indicative of a second green+red light-induced excited state (grES). Subsequent temperature increases were mirrored by rises in the $\chi_m T$ values of both the gES and grES, indicative of antiferromagnetic coupling, reaching maxima at 22 K of 1.40 and 1.99 emu mol^{-1} K respectively, before thermally relaxing to the LS phase (Figure 2.14 (b)). Both species had entirely reverted to the ground state by 100 K. Interestingly, when $[Fe^{III}_2Fe^{II}_2]$ was excited by only red light, the susceptibility reached saturation at 1.45 emu mol^{-1} K after 6 hours; very close to the value obtained for the grES (Figure 2.15). Light excitation experiments of LS-Fe^{III} LMCT band using a 1064 nm DPSS laser selectively were operated, but light-excited state was not trapped. These results suggest that the generation of HS-Fe^{II} permit Fe^{III} to show their light-induced spin transition.

(a)

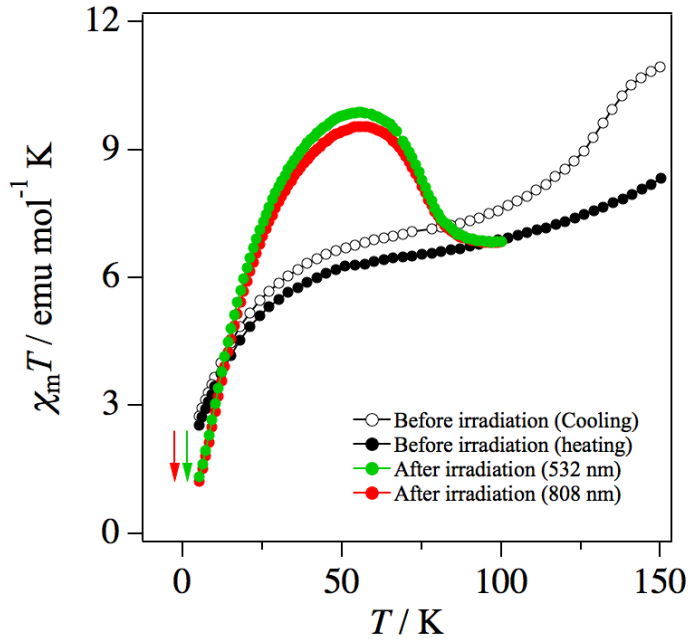

(b)

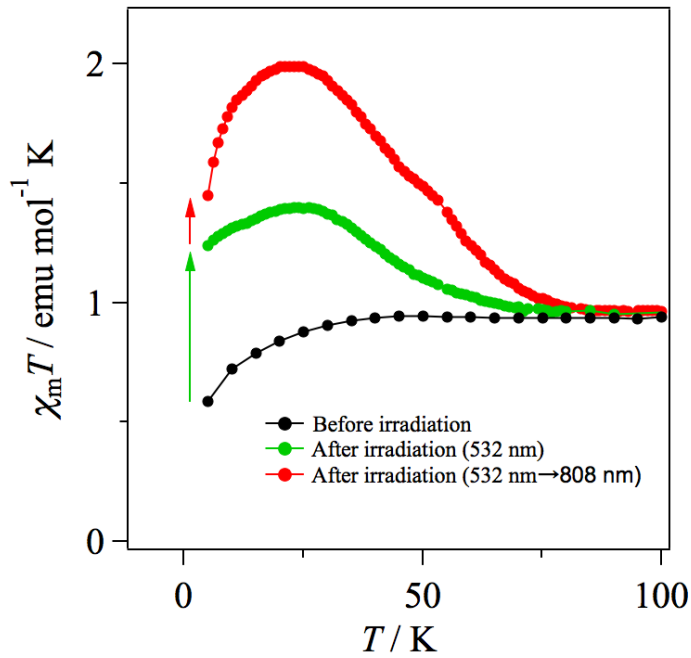

Figure 2.14: Thermal relaxation processes of LIESST phenomena for $[Fe^{II}_4]$ (a) and $[Fe^{III}_2Fe^{II}_2]$ (b). The magnetic susceptibility after light irradiation was measured using an applied magnetic field of 500 Oe and a scan rate of 0.1 K/min in scaning mode.

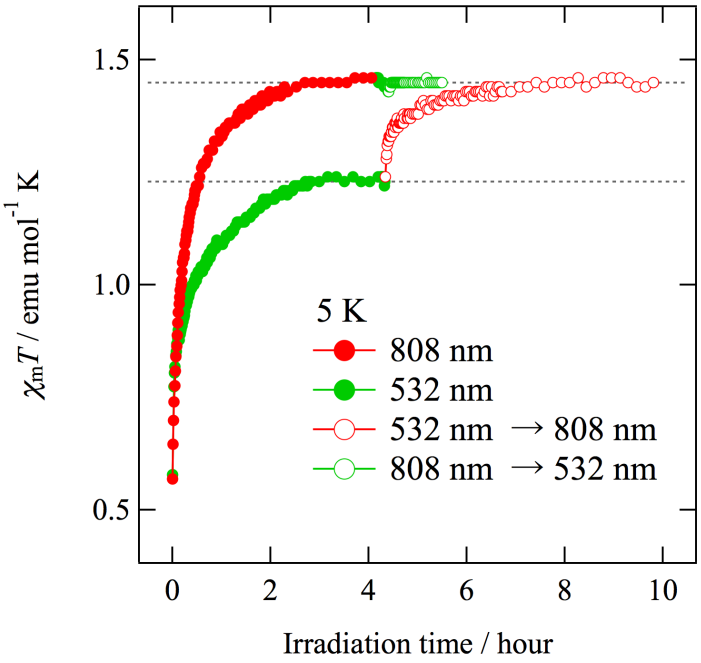

Figure 2.15: Duration and wavelength dependency of $[Fe^{III}_2Fe^{II}_2]$ photo-excitation at 5 K. After 532 nm laser light irradiation, the sample was irradiated with the 808 nm laser under the same conditions as the 532 nm laser (10 mW/cm^2), then an increase in $\chi_m T$ value was observed. When the irradiation order was reversed, (808 nm then 532 nm) no substantial difference was observed upon changing between the light sources. Red markers indicate 808 nm laser product; green markers, 532 nm laser product. Filled markers indicate initial irradiation product; empty markers, second irradiation product.

Mössbauer spectra. Temperature dependent Mössbauer spectra of $[Fe^{II}_4]$ between 293 – 5 K (Figure 2.16) and Mössbauer parameters (relative to metallic iron) are listed in Table 2.10. The Mössbauer spectrum at 293 K showed a quadruple doublet, and the Mössbauer parameters of isomer sift (δ) and quadruple splitting (ΔE_Q) are $\delta = 0.96$ mm s^{-1} with $\Delta E_Q = 1.80$ mm s^{-1} suggesting that all iron ions are HS-Fe^{II} state. The sample was cooled down to 5 K, and the Mössbauer spectrum showed two quadruple doublets, of which parameter sets ($\delta = 1.21$ mm s^{-1} and $\Delta E_Q = 2.28$ mm s^{-1}) and ($\delta = 0.27$ mm s^{-1} and $\Delta E_Q = 1.01$ mm s^{-1}) and the peak-intensity ratio is 52/48, are characteristic of HS-Fe^{II} and LS-Fe^{II} ions, respectively. The Mössbauer spectra at 100 K also showed two quadruple doublets, of which parameter sets ($\delta = 1.17$ mm s^{-1} and $\Delta E_Q = 2.21$ mm s^{-1}) and ($\delta = 0.29$ mm s^{-1} and $\Delta E_Q = 0.97$ mm s^{-1}) and the peak-intensity ratio is HS-Fe^{II}/LS-Fe^{II} = 54/46. The Mössbauer spectra at 180 K (heating mode) showed two quadruple doublets, of which parameter sets ($\delta = 1.05$ mm s^{-1} and $\Delta E_Q = 2.02$ mm s^{-1}) and ($\delta = 0.29$ mm s^{-1} and $\Delta E_Q = 1.05$ mm s^{-1}) and the peak-intensity ratio is HS-Fe^{II}/LS-Fe^{II} = 76/24. The results suggested that $[Fe^{II}_4]$ showed two-step LS-Fe^{II} to HS-Fe^{II} thermal spin transition.

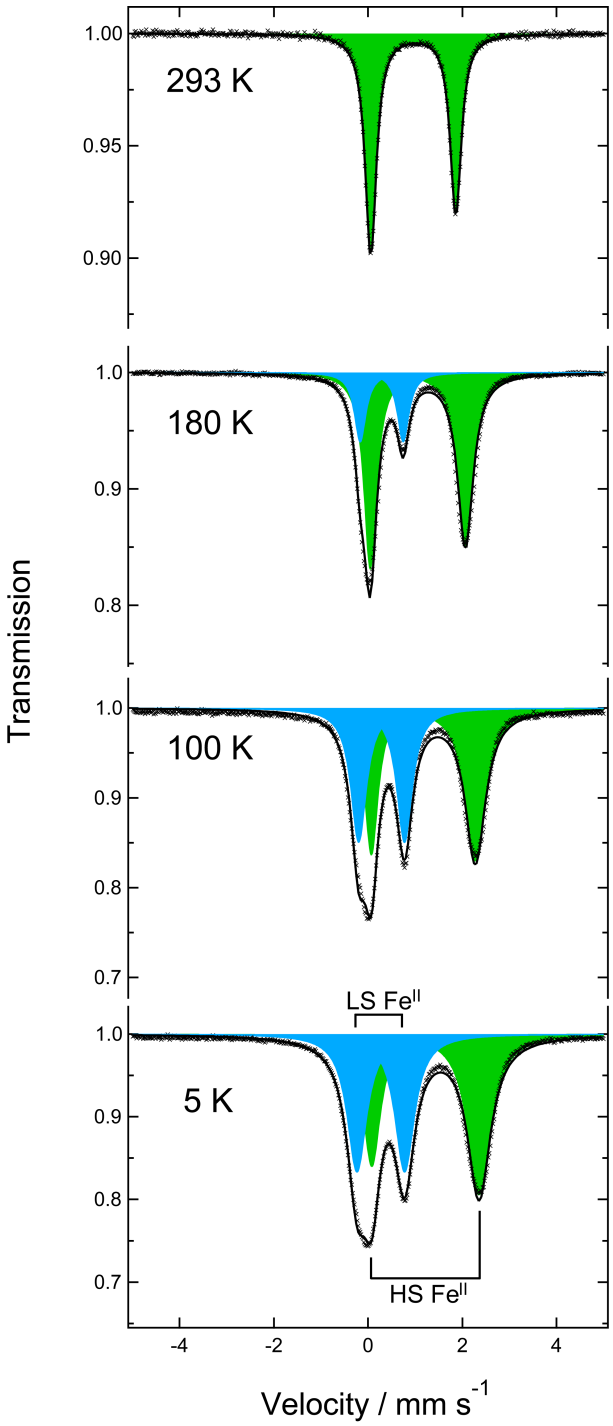

Figure 2.16: Temperature dependent Mössbauer spectra of [Fe^{II}_4] between 293 K and 5 K. Parameters see Table 2.10.

Table 2.10: Mössbauer parameters for $[Fe^{II}_4]$.

	δ (mm s^{-1})[a]		ΔE_Q (mm s^{-1})[b]		Area fractions (%)	
T (K)	LS-Fe^{II}	HS-Fe^{II}	LS-Fe^{II}	HS-Fe^{II}	LS-Fe^{II}	HS-Fe^{II}
293	—	0.96	—	1.80	—	100
180 (↑)[c]	0.29	1.05	0.91	2.02	24	76
100 (↑)[c]	0.29	1.17	0.97	2.21	46	54
5	0.27	1.21	1.01	2.28	48	52

[a] Isomer shift relative to metallic iron. [b] Quadrupole splitting. [c] Measured in heating mode.

Temperature dependent Mössbauer spectra of $[Fe^{III}_2Fe^{II}_2]$ between 300 – 5 K (Figure 2.17) and Mössbauer parameters are listed in Table 2.11. Mössbauer spectrum showed three quadruple doublets at 5 K, of which parameter sets (δ = 0.08 mm s^{-1} and ΔE_Q = 3.27 mm s^{-1}), (δ = 0.19 mm s^{-1} and ΔE_Q = 3.06 mm s^{-1}), and (δ = 0.37mm s^{-1} and ΔE_Q = 0.87 mm s^{-1}), and the peak-intensity ratio is 27/27/46, are characteristic of two kinds of LS-Fe^{III} and LS-Fe^{II} ions, respectively. The spectra at 100 K also showed three quadruple doublets and the peak-intensity ratio is LS-Fe^{III}/ LS-Fe^{III}/ LS-Fe^{II} = 27/27/46 suggesting that $[Fe^{III}_2Fe^{II}_2]$ dose not shows thermal SCO behaviour between 5 K and 100 K. At 200 K, the peak-intensity of LS-Fe^{III} decreased and new doublet peak with δ = 0.35 mm s^{-1} and ΔE_Q = 1.02 mm s^{-1} which corresponding to the HS-Fe^{III} ion was observed. The peak-intensity ratio is LS-Fe^{III}/ LS-Fe^{III}/ HS-Fe^{III}/ LS-Fe^{II} = 25/25/5/45 suggests that Fe^{III} ions showed thermal SCO behaviour above 100 K. As heating the sample, the peak-intensity of HS-Fe^{III} increase and the ratio is LS-Fe^{III}/ LS-Fe^{III}/ HS-Fe^{III}/ LS-Fe^{II} = 21/21/13/45 at 300 K. The temperature dependent Mössbauer measurements of $[Fe^{III}_2Fe^{II}_2]$ make clear that the increase of $\chi_m T$ value at high temperature region is originated from the thermal spin transition of LS-Fe^{III} to HS-Fe^{III} ions.

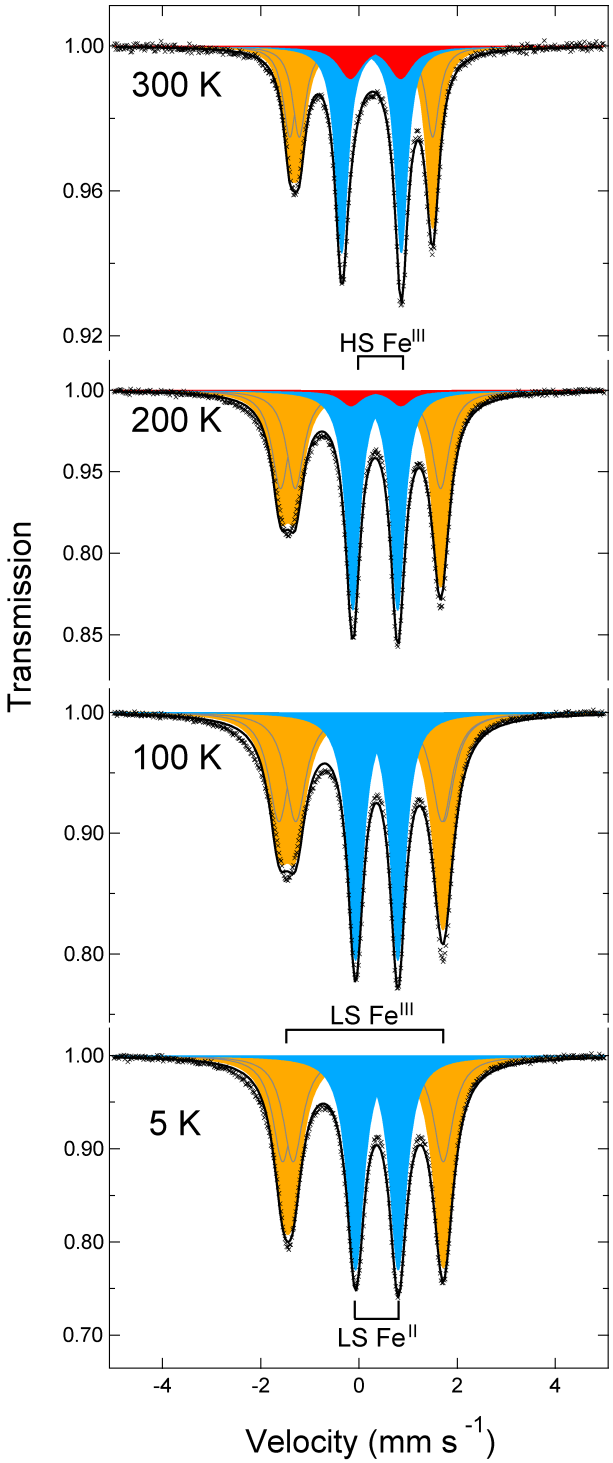

Figure 2.17: Temperature dependent Mössbauer spectra of $[Fe^{III}_2Fe^{II}_2]$ between 300 K and 5 K. Parameters see Table 2.11.

Table 2.11: Mössbauer parameters for $[Fe^{III}_2Fe^{II}_2]$.

	δ (mm s^{-1})			
T (K)	LS-Fe^{III}	LS-Fe^{III}	HS-Fe^{III}	LS-Fe^{II}
300	0.05	0.14	0.34	0.26
200	0.03	0.18	0.35	0.33
100	0.05	0.20	—	0.36
5	0.08	0.19	—	0.37

	ΔE_Q (mm s^{-1})			
T (K)	LS-Fe^{III}	LS-Fe^{III}	HS-Fe^{III}	LS-Fe^{II}
300	2.90	2.72	1.02	1.21
200	3.26	2.96	1.02	0.91
100	3.36	2.98	—	0.86
5	3.27	3.06	—	0.87

	Area fractions (%)			
T (K)	LS-Fe^{III}	LS-Fe^{III}	HS-Fe^{III}	LS-Fe^{II}
300	21	21	13	45
200	25	25	5	45
100	27	27	—	46
5	27	27	—	46

Due to the low relaxation temperature and the existence of intramolecular antiferromagnetic interactions at low temperature, the spin states of the excited species could not be elucidated by susceptibility data alone. To investigate the electronic characteristics of the light induced excited states, light irradiation experiments of Mössbauer spectra were operated. Before irradiation, measurements conducted on [Fe^{II}_4] at 5 K showed two doublet peaks corresponding to LS-Fe^{II} and HS-Fe^{II} ions with a peak-intensity ratio of HS-Fe^{II}/LS-Fe^{II} = 0.52/0.48 (Figure 2.18 and Table 2.12). When the sample was irradiated with 532 nm laser at 5 K, the LS-Fe^{II} peak intensity decreased, and the peak-intensity ratio of LS-Fe^{II}/HS-Fe^{II} changed to 0.18/0.82, suggesting LS-Fe^{II} to HS-Fe^{II} spin conversion had occurred. 808 nm irradiation resulted in a similar final peak-intensity ratio of LS-Fe^{II}/HS-Fe^{II} = 0.17/ 0.83, suggesting that irradiation at both 532 nm and 808 nm generated a photo-induced HT* (4HS) state from the 2HS-2LS state.

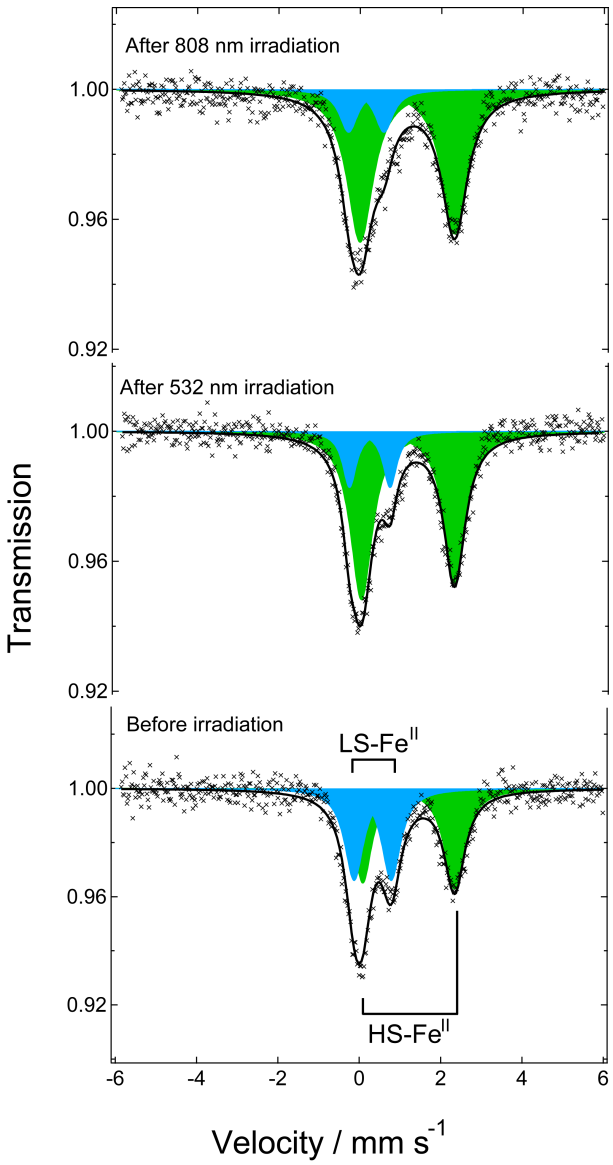

Figure 2.18: Light dependent Mössbauer spectra of [Fe^{II}_4] at 5 K. For the fitting parameters see Table 2.12.

Table 2.12: Mössbauer parameters for $[Fe^{II}_4]$ at 5 K.

	δ (mm s^{-1})		ΔE_Q (mm s^{-1})		Area fractions (%)	
	LS-Fe^{II}	HS-Fe^{II}	LS-Fe^{II}	HS-Fe^{II}	LS-Fe^{II}	HS-Fe^{II}
After 808 nm irradiation	0.15	1.15	0.87	2.32	17	83
After 532 nm irradiation	0.23	1.17	1.00	2.29	18	82
Before irradiation	0.33	1.21	0.91	2.26	48	52

The Mössbauer spectrum of $[Fe^{III}_2Fe^{II}_2]$ collected in the absence of light at 5 K showed two doublet peaks, corresponding to LS-Fe^{II} and LS-Fe^{III}, with a peak-intensity ratio of LS-Fe^{III}/LS-Fe^{II} = 0.45/0.55 (Figure 2.19 and Table 2.13). After 532 nm laser irradiation at 5 K, however, the LS-Fe^{II} absorption decreased, and a new doublet appeared corresponding to HS-Fe^{II}. The peak-intensity ratio of LS-Fe^{III}/HS-Fe^{III}/LS-Fe^{II}/HS-Fe^{II} = 0.42/0.00/0.31/0.27 confirmed that Fe^{II}-specific LIESST had occurred after exposure to green light. Following green light excitation, the sample was then irradiated with an 808 nm laser at 5 K. The intensity of the LS-Fe^{III} doublet peak decreased, and a new doublet peak emerged with a small quadrupole splitting parameter corresponding to HS-Fe^{III}. The peak-intensity ratio of LS-Fe^{III}/HS-Fe^{III}/LS-Fe^{II}/HS-Fe^{II} = 0.32/0.13/0.30/0.25, confirmed that the red light had led to the selective LIESST of the Fe^{III} ions. The results suggested that 532 nm light irradiation induced the LS-Fe^{II} to HS-Fe^{II} spin transition, and that 808 nm light irradiation induced LS-Fe^{III} to HS-Fe^{III} spin transition selectively, resulting in the remarkable situation of generating a tetranuclear cluster in which iron ions are present in four different electronic states.

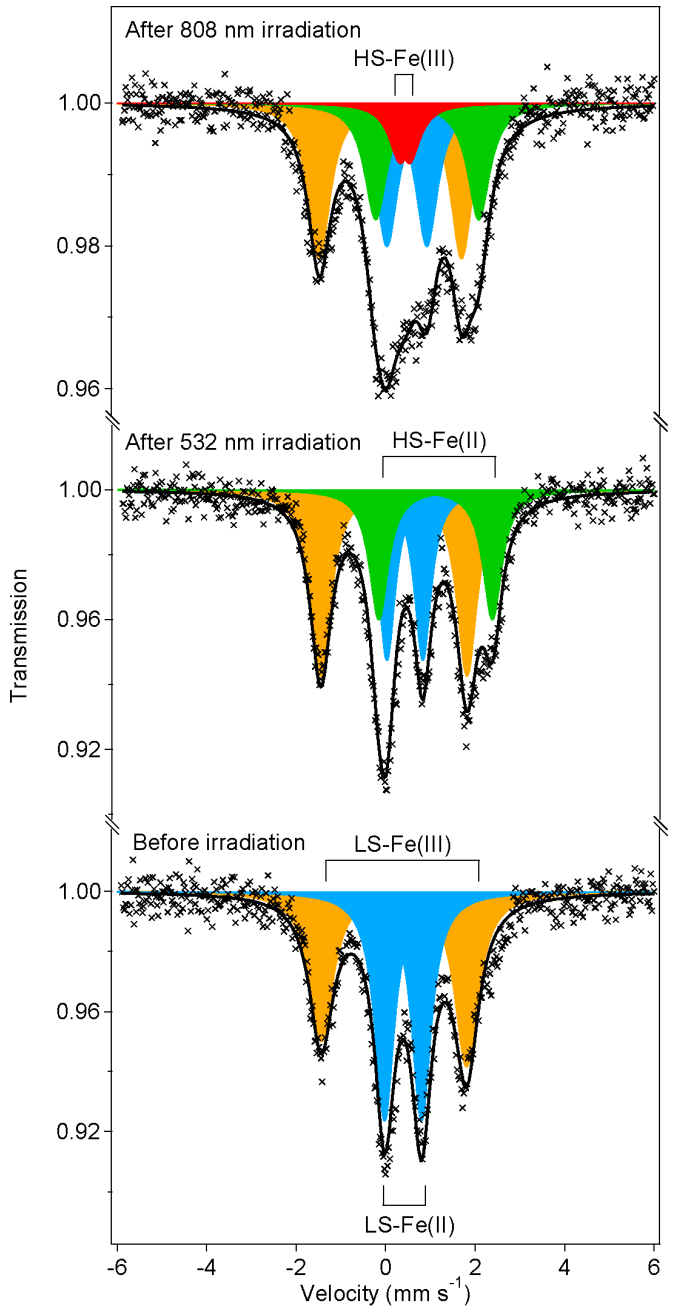

Figure 2.19: The light irradiation dependence ^{57}Fe Mössbauer spectra of [$Fe^{III}_2Fe^{II}_2$] at 5 K. The Mössbauer spectra confirm that irradiation with 532 nm (green) laser results in Fe^{II}-specific LIESST, while subsequent irradiation with 808 nm (red) laser light caused spin transition to occur the Fe^{III} ions. For the fitting parameters see Table 2.13.

Table 2.13: Mössbauer parameters for $[Fe^{III}_2Fe^{II}_2]$ at 5 K.

	δ (mm s^{-1})			
	LS-Fe^{III}	HS-Fe^{III}	LS-Fe^{II}	HS-Fe^{II}
After 532 nm + 808 nm irradiation	0.11	0.43	0.47	0.93
After 532 nm irradiation	0.17	—	0.42	1.11
Before irradiation	0.18	—	0.39	—

	ΔE_Q (mm s^{-1})			
	LS-Fe^{III}	HS-Fe^{III}	LS-Fe^{II}	HS-Fe^{II}
After 532 nm + 808 nm irradiation	3.18	0.19	0.89	2.30
After 532 nm irradiation	3.27	—	0.80	2.54
Before irradiation	3.25	—	0.82	—

	Area fractions (%)			
	LS-Fe^{III}	HS-Fe^{III}	LS-Fe^{II}	HS-Fe^{II}
After 532 nm + 808 nm irradiation	32	13	30	25
After 532 nm irradiation	42	—	31	27
Before irradiation	45	—	55	—

2.4 Conclusion

Homo- ($[Fe^{II}_4]$) and heterovalent ($[Fe^{III}_2Fe^{II}_2]$) grids were synthesized and found to display light-induced excited spin state trapping (LIESST) at low temperatures. While $[Fe^{II}_4]$ showed hysteretic multi-step thermal spin-crossover (SCO) behaviour, $[Fe^{III}_2Fe^{II}_2]$ showed little thermal SCO up to 300 K. Irradiation of $[Fe^{III}_2Fe^{II}_2]$ at low temperatures with green and red lasers, however, led to Fe^{II} and Fe^{III}-specific LIESST phenomena respectively; the first observation of site-selective spin state switching. In all, the $\{Fe_4L_4\}^{n+}$ molecule showed a total of seven stable magnetic phases (spin states) and four oxidation states. Molecules displaying such extraordinary multi-stability and capacity to function as molecular switches are in great demand due to their potential applications in future technologies. In particular, the herein reported first observation of selective multistep light-induced spin state transition, through the targeted excitation of different metal centres, may have a profound effect on the design of multi-bistable systems and introduce a new level of complexity to the range of responses accessible in magnetic molecules.

---

[1] Bousseksou, A., Molnár, G., Demont, P. & Menegotto, J. Observation of a thermal hysteresis loop in the dielectric constant of spin crossover complexes: towards molecular memory devices. *J. Mater. Chem.* **13**, 2069–2071 (2003).

[2] Bousseksou, A., Molnár, G., Salmon, L. & Nicolazzi, W. Molecular spin crossover phenomenon: recent achievements and prospects. *Chem. Soc. Rev.* **40**, 3313-3335 (2011).

[3] Real, J. A., Andrés, E., Moñoz, M. C., Julve, M., Granier, T., Bousseksou, A. & Varret, F. Spin crossover in a catenane supramolecular system. *Science* **268**, 265–267 (1995).

[4] Kahn, O., Martinez, C. J. Spin-Transition Polymers: From Molecular Materials Toward Memory Devices. *Science* **279**, 44-48 (1998)

[5] Halder, G., Kepert, C. J., Moubaraki, B., Murray, K. S. & Cashion, J. D. Guest-Dependent Spin Crossover in a Nanoporous Molecular Framework Material. *Science* **298**, 1762-1765 (2002).

[6] Gütlich, P., Gaspar, A. B. & Garcia, Y. Spin state Switching in iron coordination compounds. *Beilstein J. Org. Chem.* **9**, 342-391 (2013).

[7] Güetlich, P. & Goodwin, H. A. (eds.) Spin crossover in transition metal compounds III. *Top. Curr. Chem.* **235**, (2004).

[8] Halcrow, M. A. Trapping and manipulating excited spin states of transition metal compounds. *Chem. Soc. Rev.* **37**, 278-289 (2008).

[9] Halepto, D. M., Holt, D. G. L., Larkworthy, L. F. Leigh, G. L. Povey, D.C. & Smith, G. W. Spin crossover in chromium(II) complexes and the crystal and molecular structure of the high spin form of bis[1,2-bis(diethylphosphino)ethane]di-iodochromium(II). *J. Chem. Soc., Chem. Commum.* 1322-132 (1989).

[10] Sim, P. G. & Sinn, E. First Manganese(III) Spin Crossover and First d^4 Crossover. Comment on Cytochrome Oxidase. *J. Am. Chem. Soc.* **103**, 241-243 (1981).

[11] Hayami, S., Komatsu, Y., Shimizu, T., Kamihata, H. & Lee, Y. H. Spin-crossover in cobalt(II) compounds containing terpyridine and its derivatives. *Coord. Chem. Rev.* **255**, 1981-1990 (2011).

[12] Nihei, M., Shiga, T., Maeda, Y. & Oshio, H. Spin crossover iron(III) complexes. *Coord. Chem. Rev.* **251**, 2606-2621 (2007).

[13] Venkataramani, S., Jana, U., Dommaschk, M., Sönnichses, F. D.,Tuczek, F. & Herges, R. Magnetic Bistability of Molecules in Homogeneous Solvent at Room Temperature. *Science* **331**, 445-448 (2011).

[14] Létard, J.-F., Réal, J. A., Moliner, N., Gaspar, A. B., Capes, L., Cador, O. & Kahn, O. Light Induced Excited Pair Spin State in an Iron(II) Binuclear Spin-Crossover Compound. *J. Am. Chem. Soc.* **121**, 10630–10631 (1999).

[15] Hauser, A., Vef, A. & Adler, P. Intersystem crossing dynamics in Fe(II) coordination compounds. *J. Chem. Phys.* **95**, 8710-8717 (1991).

[16] Vef, A., Manthe, U., Güetlich, P. & A. Hauser, A. Intersystem crossing dynamics in the spin-crossover systems $[M:Fe(pic)_3]Cl_2Sol$ (M=Mn or Zn, Sol=MeOH or EtOH). *J. Chem. Phys.* **101**, 9326-9332 (1994).

[17] Juhász, G., Hayami, S., Sato, O. & Maeda, Y. Photo-induced spine transition for iron(III) compounds with π-π interactions. *Chem. Phys. Lett.* **364**, 164-170 (2002).

[18] Rotaru, A., Dugay, J., Tan, R. P., Gural'skiy, I. A., Salmon, L., Demont, P., Carrey, L., Molnár, G., Respaud, M. & Bousseksou, A. Nano-electromanipulation of Spin Crossover Nanorods: Towards Switchable Nanoelectronic Devices. *Adv. Mater.* **25**, 1745-1749 (2013).

[19] Li, B., Wei, R.-J., Tao, J. Huang, R.-B., Zheng, L.-S. & Zheng, Z. Solvent-Induced Transformation of Single Crystals of a Spin-Crossover (SCO) Compound to Single Crystals with Two Distinct SCO Centers. *J. Am. Chem. Soc.* **132**, 1558–1566 (2010).

[20] Nihei, M., Tahira, H., Takahashi, N., Otake, Y., Yamamura, Y., Saito, K. & Oshio, H. Multiple Bistability and Tristability with Dual Spin-State Conversions in $[Fe(dpp)_2][Ni(mnt)_2]\cdot 2MeNO_2$. *J. Am. Chem. Soc.* **131**, 3553–3560 (2010).

[21] Gaspar, A. B., Muñoz, M. C. & Real, J. A. Dinuclear iron(II) spin crossover compounds: singular molecular materials for electronics. *J. Mater. Chem.* **16**, 2522-2533 (2006).

[22] Nihei, M., Ui, M., Yokota, M., Han, L.-Q., Maeda, A., Kishida, H., Okamoto, H. & Oshio, H. Two-step Spin Conversion in a Cyanide Bridged Ferrous Square. *Angew. Chem. Int. Ed.* **44**, 6484-6487 (2005).

[23] Wei, R.-J., Hun, Q., Tao, J., Huang, R.-B. & Zheng, L.-S. Spin-Crossover Fe_4^{II} Square: Two-Step Complete Spin Transition and Reversible Single-Crystal-to-Single-Crystal Transformation. *Angew. Chem. Int. Ed.* **50**, 8940-8943 (2011).

[24] Breuning, E., Rubem, M., Lehn, J.-M. Renz, F. Garcia, Y., Ksenofontov, V., Gütlich, E., Wegelius, K. & Rissanen, K. Spin Crossover in a Supermolecular Fe^{II}_4 [2 × 2] Grid Triggered by Temperature, Pressure, and Light. *Angew. Chem. Int. Ed.* **39**, 2504-2507 (2000).

[25] Schneider, B., Demeshko, S., Dechert, S. & Meyer, F. A Double-Switching Multistable Fe_4 Grid Complex with Stepwise Spin-Crossover and Redox Transition. *Angew. Chem. Int. Ed.* **49**, 9274-9277 (2010).

[26] Wang, Y.-T., Li, S.-T., Wu, S.-Q., Cui, A.-L., Shen, D.-Z. & Kou, H.-Z. Spin Transitions in Fe(II) Metallogrids Modulated by Substituents, Counteranions, and Solvents. *J. Am. Chem. Soc.* **135**, 5942–5945 (2013).

[27] Sato, H., Miya, L., Mitsumoto, K., Matsumoto, T., Shiga, T., Newton, G. N. & Oshio, H. Multi-redox Active [3 × 3] Copper Grids. *Inorg. Chem.* **52**, 9714-9716 (2013).

[28] Zhao, L., Matthews, C. J., Thompson, L. K. & Heath, S. L. A novel magnetically coupled nanomanganese(II) 3 × 3 portculluis-like gird involving just oxygen bridges, generated by strict self assembly of the metal cation and a single heptadentate ligand. *Chem. Commun.* 265-266 (2000).

[29] Shiga, T., Matsumoto, T., Noguchi, M., Onuki, T., Hoshiono, N., Newton, G. N., Nakano, N. & Oshio, H. Cobalt Antiferromangetic Ring and Grid Single-Molecule Magnet. *Chem. – Asian J.* **4**, 1660-1663 (2009).

[30] Wu, D.-Y., Sato, O.,Einaga, Y. & Duan, C.-Y. A Spin-Crossover Cluster of Iron(II) Exhibiting a Mixed-Spin Structure and Synergy between Spin Transition and Magnetic Interaction. *Angew. Chem. Int. Ed.* **48**, 1475-1478 (2009).

[31] Zueva, E. M., Ryabikh, E. R. & Borshch, S. A. Theoretical Analysis of Spin Crossover in Iron(II) [2 × 2] Molecular Grids. *Inorg. Chem.* **50**, 11143-11151 (2011).

[32] Schneider, B., Demeshko, S., Neudeck, S., Dechert, S. & Meyer, F. Mixed-Spin [2 × 2] Fe4 Grid Complex Optimized for Quantum Cellular Automata. *Inorg. Chem.*, **52**, 13230-13237 (2013).

[33] Bréfuel, N., Watanabe, H., Toupet, L., Come, J., Matsumoto, N., Collet, E., Tanaka, K. & Tuchagues, J.-P. Concerted Spin Crossover and Symmetry Breaking Yield Three Thermally and One Light-Induced Crystallographic Phases of a Molecular Material. *Angew. Chem., Int. Ed.* **48**, 9304-9307 (2009).

[34] Griffin, M., Shakespeare, S., Shepherd, H. J., Harding, C. J., Létard, J.-F., Desplanches, C., Goeta, A. E., Howard, J. A. K., Powell, A. K. Mereacre, V., Garcia, Y., Naik, A. D., Müller-Bunz, H., & Morgan, G. G. A Symmetry-Breaking Spin-State Transition in Iron(III). *Angew. Chem. Int. Ed.* **50**, 896-900 (2011).

[35] Vieira, B. J. C., Coutinho, J. T., Santos, I. C., Pereira, L. C. J., Waerenborgh, J. C. & da Gama, V. [Fe(nsal$_2$trien)]SCN, a New Two-Step Iron(III) Spin Crossover Compound, with Symmetry Breaking Spin-State Transition and an Intermediate Ordered State. *Inorg. Chem.* **52**, 3845-3850 (2013).

[36] Slater, J. W., D'Alessandro, D. M., Keene, F. R. & Steel, P. J. Metal-metal interactions in dinuclear ruthenium complexes containing bridging 4,5-di(2-pyridyl)imidazolates and related ligands. *Dalton Trans.* 1954-1962 (2006).

[37] Hayami, S., Hiki, K., Kawahara, T., Maeda, Y., Urakami, D., Inoue, K., Ohama, M., Kawata, S. & Sato, O. Photo-Induced Spin Transition of Iron(III) Compounds with π-π Intermolecular Interactions. *Chem. Eur. J.* **15**, 3497-3508 (2009).

[38] D'Alessandro, D. M. & Keene, F. R. Intervalence Charge Transfer (IVCT) in Trinuclear and Tetranuclear Complexes of Iron, Ruthenium, and Osmium. *Chem. Rev.* **106**, 2270-2298 (2006).

[39] Cook, C., Habib, F., Aharen, T., Clérac, R., Hu, A. & Murugesu, M. High-Temperature Spin Crossover Behavior in a Nitrogen-Rich Fe^{III}-Based System. *Inorg. Chem.* **52**, 1825- 1831 (2013).

[40] Guionneau, P., Brigouleix, C., Barrans, Y., Goeta, A. E., Létard, J.-F., Howard, J. A. K., Gaultier, J. & Chasseau, D. High pressure and very low temperature effects on the crystal structures of some iron(II) complexes. *C. R. Acad. Sci. Ser. IIc* **4**, 161-171 (2001).

[41] Guionneau, P., Marchivie, M., Bravic, G., Létard, J.-F. & Chasseau, D. Co(II) molecular complexes as a reference for the spin crossover in Fe(II) analogues. *J. Mater. Chem.* **12**, 2546-2551 (2002).

CHAPTER 3

Solid-state NMR Study of Antiferromagnetic Oxovanadium Rings

3.1 Introduction

Ring-shaped metal complex molecules with antiferromagnetic interactions between metal ions may have unique magnetic ground states depending on their number of metal ions. Even-membered rings were well investigated to exemplify quantum effects based on topologically assembled spin systems in the field of molecular magnetism. An structure of an iron deca-nuclear complex, $[Fe^{III}_{10}(OMe)_{20}(O_2CCH_2Cl)_{10}]$ (Fe10) was first reported by Lippard et al. in 1990,[1] and the magnetic properties was reported in 1994 (Figure 3.1 (a)).[2] At very low temperature, the spin ground state of the Fe10 wheel was spin singlet up to an applied magnetic field of 3 T. As the magnetic field was increased, magnetization (M) showed some steps corresponding to transitions between quantum spin states (Figure 3.1 (b)). These magnetization steps are the characteristic behaviour of discrete antiferromagnetic molecular systems. Solid-state nuclear magnetic resonance (NMR) measurements of the Fe10 wheel were reported by Borsa et al., in which they studied its spin dynamics. Measurements of nuclear spin-lattice relaxation time, T_1, and analyses of its reciprocal T_1^{-1} (nuclear spin-lattice relaxation rate) afford a powerful tool for the investigation of spin dynamics since the relaxation of a nuclear spin is affected by fluctuations in the local field induced by hyperfine interactions with the local magnetic moments i.e. unpaired spins. In particular, ring-shaped magnetic molecules show an enhancement of T_1^{-1} at temperatures low enough to slow down of the magnetic spin fluctuations (Figure 3.1 (c)).[9]

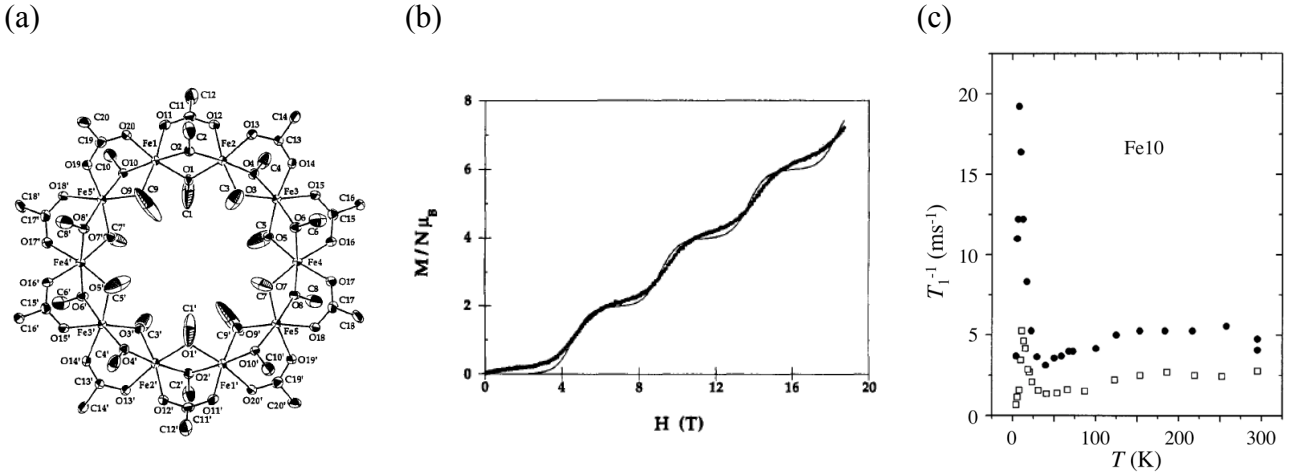

Figure 3.1: (a) ORTEP diagram of the ferric wheel Fe10. (b) Magnetization curves for Fe10 at 0.6 K. (c) ^{1}H nuclear spin-lattice relaxation rate, T_1^{-1}, versus T plots for Fe10 at two different resonance frequencies (●) 14 MHz and (□) 60 MHz.

There are other examples of antiferromagnetic rings for which the magnetic properties and solid-state NMR characteristics have been well studied, such as $[Cr_8F_8(piv)_{16}]$ (Cr8, piv = pivalic acid, Cr^{3+}; $S = 3/2$) and $[LiFe_6(OCH_3)_{12}(C_{15}H_{11}O_2)_6]B(C_6H_5)_4 \cdot CH_2Cl_2$ (Fe6(Li), Fe^{3+}; $S = 5/2$) (Figure 3.2 (a)).[3,4] In both cases, antiferromagnetic interactions are operative between the metal ions, and the exchange coupling constants between neighboring paramagnetic centres are $J/k_B \cong -17.2$ K for Cr8 and $J/k_B \cong -21$ K for Fe6(Li), respectively. Solid-state NMR measurements were performed for these rings and reveal the enhancement of T_1^{-1} at low temperatures.[5] The $1/T_1\chi T$ versus T plots showed the characteristic peaks, and suggest that slowing down of the magnetic spin fluctuations occurred around the peak temperature (Figure 3.2 (b)). The spin fluctuation frequency (Γ) showed temperature dependency and decreased as temperature was lowered with the relationship $\Gamma \propto T^{3.5}$. These studies show that solid-state NMR measurements are very powerful tools to detect the dynamics of spin fluctuation.

(a)

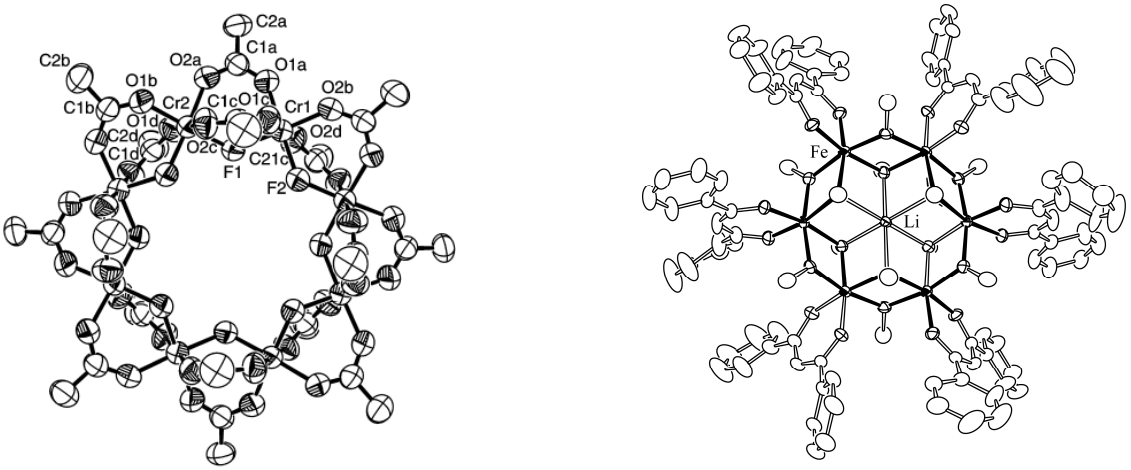

(b)

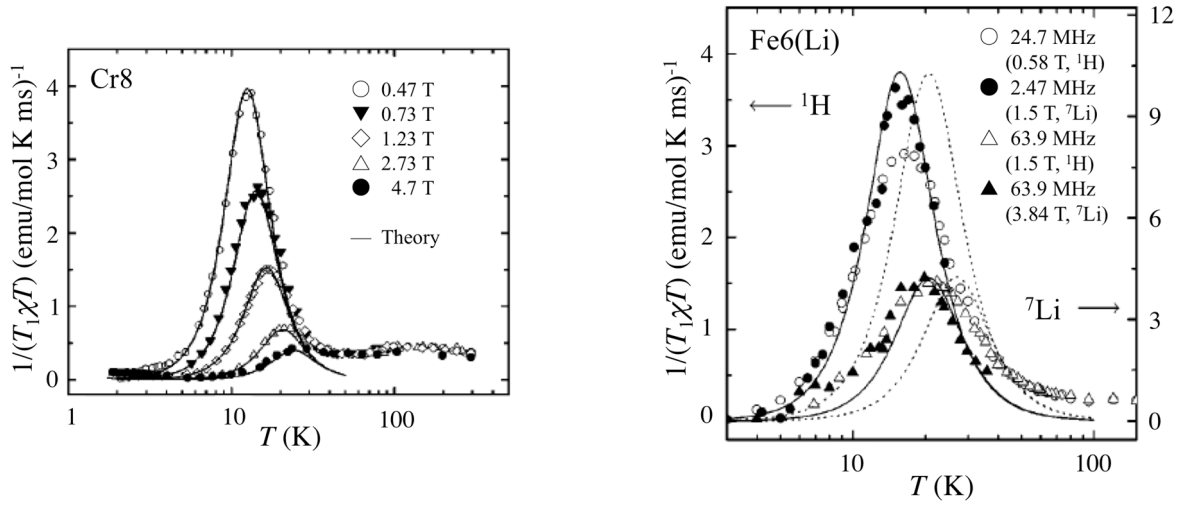

(c)

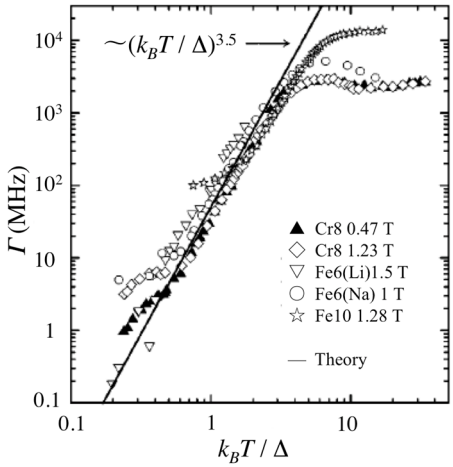

Figure 3.2: (a) ORTEP diagrams and (b) $1/T_1\chi T$ versus T plots for Cr8 (left) and Fe6(Li) (right). (c) Temperature dependence of spin fluctuation frequency for Cr8 (△; 0.47 T, ◇; 1.23 T), Fe6(Li) (▽; 1.5 T), Fe6(Na) (○; 1 T) and Fe10 (☆; 1.28 T). The constant Δ is the energy gap to the lowest S =1 state and it is approximately $\Delta = -4J/N$, where J is magnetic coupling constant and N is the number of paramagnetic metal ions in the ring.

Cyclodextrins (CDs) are a family of compounds made up of D-glucose units linked together in a ring. Typical CDs contain a number of glucose monomers ranging from six to eight units in the ring (abbr. α-, β-, γ-CD respectively). The inside of the ring structure is hydrophobic and CDs can encapsulate hydrophobic molecules, acting as molecular capsules and rendering them functional building blocks in supramolecular chemistry. In 2005, Küfers and co-workers reported a six membered supermolecular ring complex, $Na_6[VO_6Na_6(\alpha\text{-}CDH_{-12})_2]\cdot 59H_2O$ (V6), where two α-CDs sandwich six oxovanadium (VO) ions and six sodium ions, coordinating with the oxygen atoms of their alkoxo moieties, leading to an alternating (Na/V) six-membered vanadium ring structure (Figure 3.3 (a) (left)).[6] Oshio et al. expanded the sandwich-type VO ring system and reported the structure and magnetic properties of the odd-membered ring, $Na_7[VO_7Na_7(\beta\text{-}CDH_{-14})_2]\cdot 76H_2O$ (V7), isolated using β-CDs as stabilizing ligands in 2009.[7] VO has S = 1/2 spin and antiferromagnetic interactions are operative between metal centres in the magnetic CD rings. Moreover, Hoshino reported the structures, high-field electron paramagnetic resonance (HF-EPR) measurements, and the magnetic properties of V6, V7, and $Na_8[VO_8Na_8(\gamma\text{-}CDH_{-16})_2]\cdot 98H_2O$ (V8) complexes in his Ph.D. thesis,[8] and showed that antiferromagnetic interactions ($\theta \cong$ -0.6 K for V6, $\theta \cong$ -0.5 K for V7, and $\theta \cong$ -0.5 K for V8, θ is Weiss temperature) are operative in all VO rings (Figure 3.3 (b)). Micro-SQUID measurements were performed at ultralow temperature and the results suggest that while the spin ground state of V6 and V8 are spin singlet, V7 is spin doublet. In this work, solid-state NMR measurements were performed to study the static and dynamic properties of the magnetic ground state of the VO antiferromagnetic ring systems at ultralow temperature.

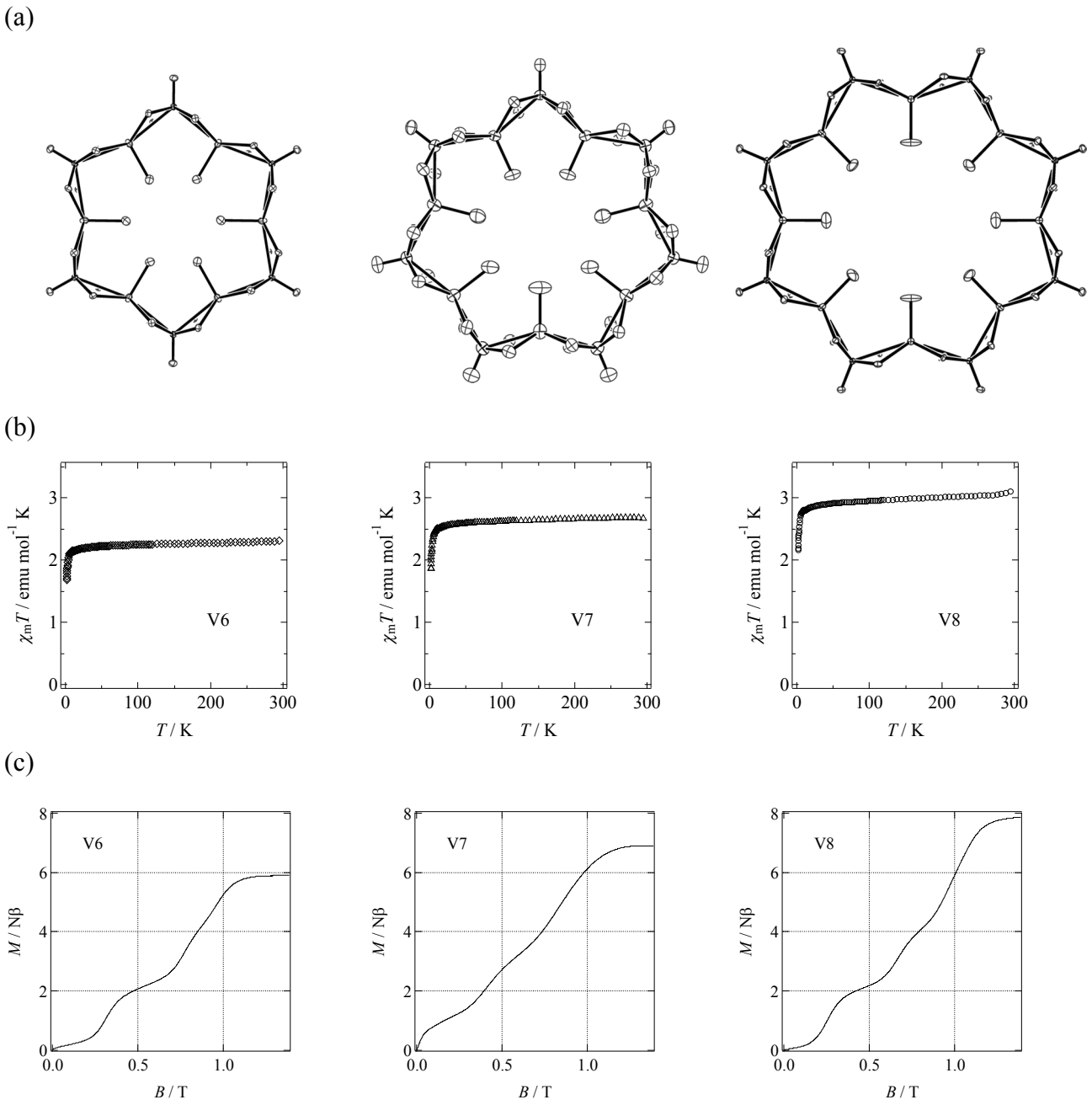

Figure 3.3: (a) ORTEP diagrams of the core structure, (b) temperature dependency magnetic susceptibility data, and (c) magnetization curves at 0.04 K for V6 (left), V7 (center), and V8 (right).

3.2 Experiments

Experimental Procedures

Solid-state NMR measurements: Deuterium oxide substituted samples were prepared for the measurements. Solid-state ^{1}H-NMR measurements utilized a homemade phase-coherent spin-echo pulse spectrometer (^{1}H, I = 1/2; $\gamma_N/2\pi$ = 42.5774 MHz/T). The ^{1}H-NMR spectra at the resonance frequency of 7.1 MHz or 11.6 MHz were obtained either by sweeping the magnetic field (for V6 and V7) or by Fourier transformation of the NMR echo signal (for V8). The proton spin-lattice relaxation time measurements were measured by the saturation method. The NMR measurements at ultralow temperature were carried out using a ^{3}He-^{4}He dilution refrigerator.

Synthetic Procedures

All chemicals were used without further purification except when noted. $VOSO_4 \cdot nD_2O$ and NaOD were prepared by the recrystallization of $VOSO_4 \cdot nH_2O$ and NaOH from D_2O (99.9 %). In each case three recrystallizations were performed to ensure complete deuteration.

Preparation of $Na_n[(VO)_nNa_n(D_2O)_n(CD)_2] \cdot xD_2O$
(V6; {n, CD} = {6, α-CDH$_{-12}$}, V7; {7, β-CDH$_{-14}$}, V8; {8, γ-CDH$_{-16}$})

The suspension of $VOSO_4 \cdot nD_2O$ (110 mg) and CD (140 mg) in D_2O (1.0 mL) was added into the solution of NaOD (192 mg) and CD (140 mg) in D_2O (1.0 mL). The brown solution was separated into four batches and acetone (0.2 mL) was allowed to diffuse into each, resulting in the formation of blue rhombic crystals, which were collected by filtration.

X-ray structure analyses of V6, V7 and V8 reveal that the D_2O substituted crystals are isomorphous to the H_2O crystals.

3.3 Results and Discussion

^{1}H-NMR spectra measurements. Temperature dependent ^{1}H-NMR spectra were collected using the ^{3}He-^{4}He dilution refrigerator down to ca. 60 mK. The NMR spectra of V6 and V7 were obtained by sweeping the external magnetic field at constant frequency, and the spectra of V8 were obtained by Fourier transformation of the NMR echo signal (Figure 3.4-3.6). All vanadium rings showed single peaks and the peak widths (FWHA; full width at half amplitude) showed temperature dependence (Figure 3.7-3.9).

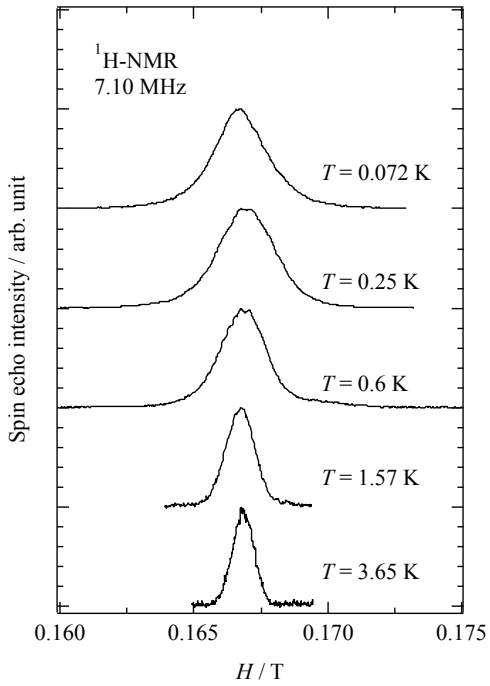

Figure 3.4: Temperature dependency ^{1}H-NMR spectra of V6 at the resonance frequency of 7.1 MHz.

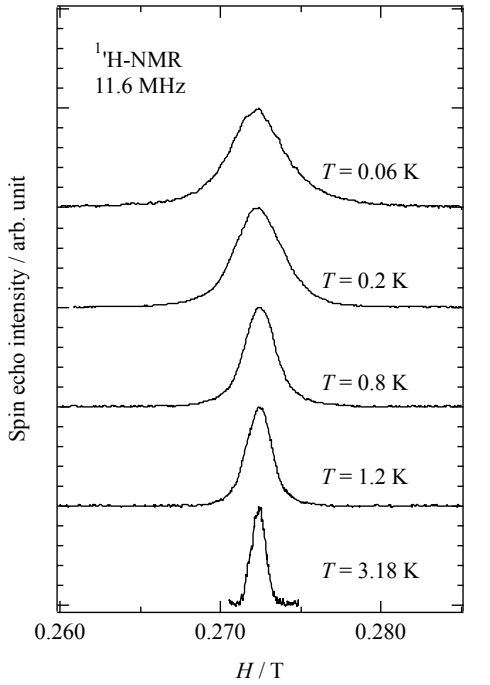

Figure 3.5: Temperature dependency ^{1}H-NMR spectra of V7 at the resonance frequency of 11.6 MHz.

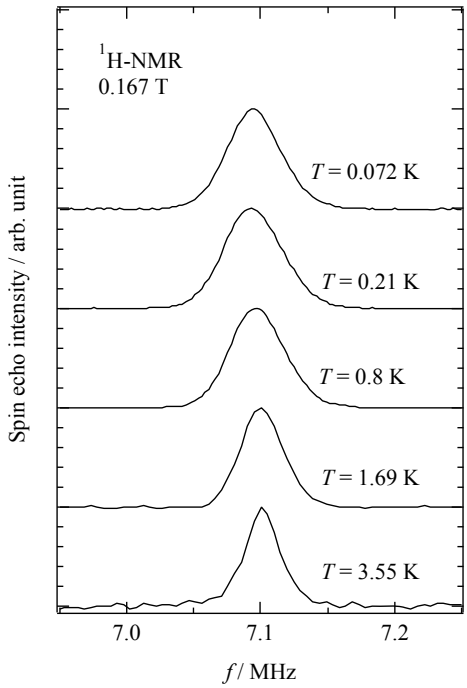

Figure 3.6: Temperature dependency ^{1}H-NMR spectra of V8 at 0.167 T. The spectra were obtained by Fourier transformation of the NMR echo signal.

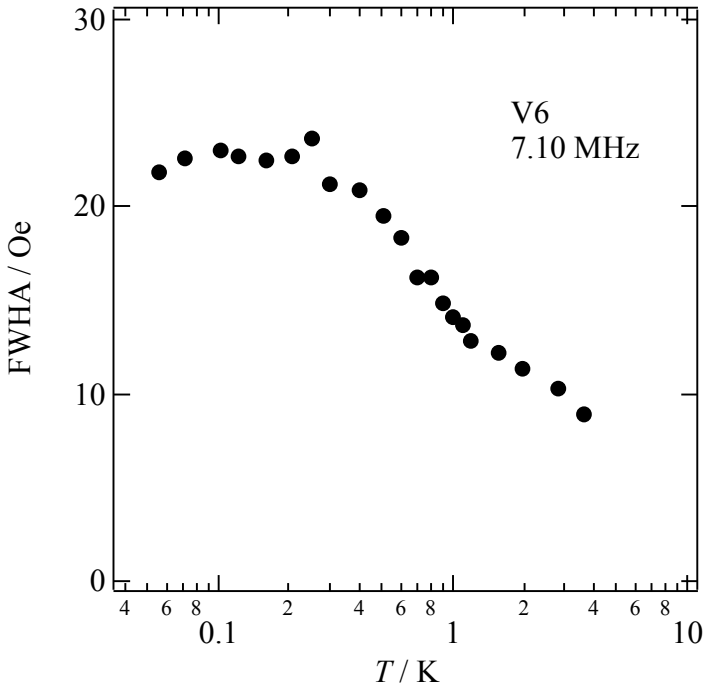

Figure 3.7: Full widths at half amplitude of the ^{1}H-NMR spectra in V6 plotted as a function of temperature.

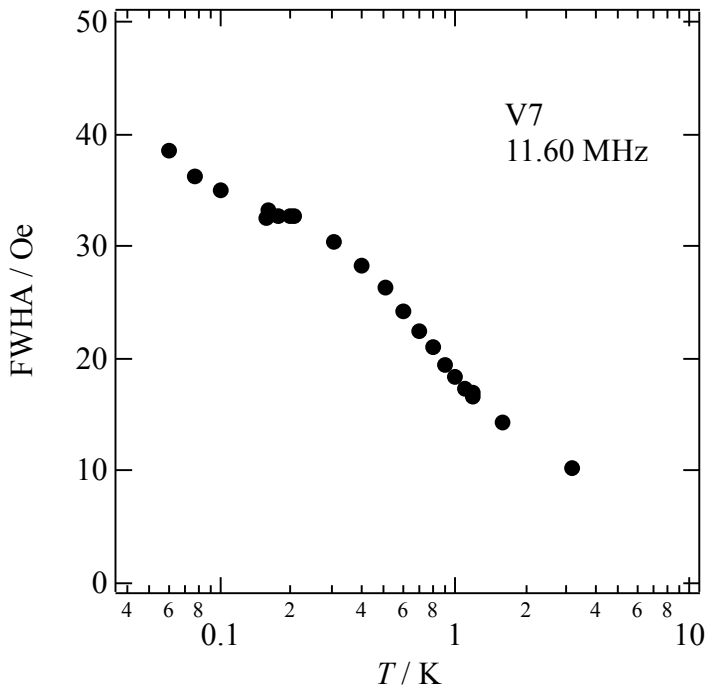

Figure 3.8: Full widths at half amplitude of the ^{1}H-NMR spectra in V7 plotted as a function of temperature.

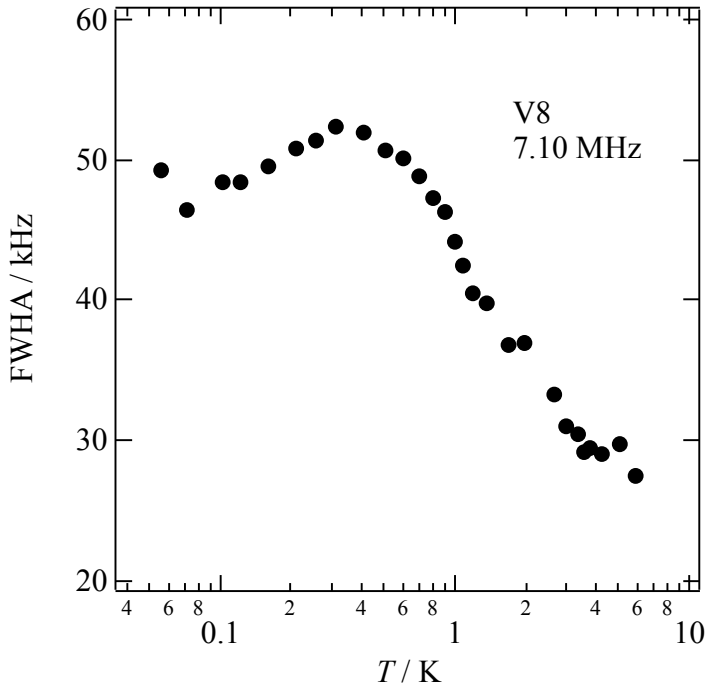

Figure 3.9: Full widths at half amplitude of the ^{1}H-NMR spectra in V8 plotted as a function of temperature.

The peak width of NMR spectra is proportionate to the magnetic susceptibility. Thus, the magnetic susceptibility data for V6, V7, and V8 below 1.8 K could be determined from NMR spectral data (Figure 3.10). As the samples were cooled, the magnetic susceptibility (χ) increased, conforming to the Curie-Weiss law in the paramagnetic region. V6 and V8 showed peaks, with the magnetic susceptibility decreasing below the peak temperature (Curie temperature, T_c). This behaviour suggests that V6 and V8 reach the antiferromagnetic ordered phase as complete molecules below the T_c, and the spin multiplicities of the rings at ground state are close to spin singlet. On the other hand, the magnetic susceptibility of V7 increased with cooling suggesting that the ground state of V7 is not spin singlet, but spin doublet.

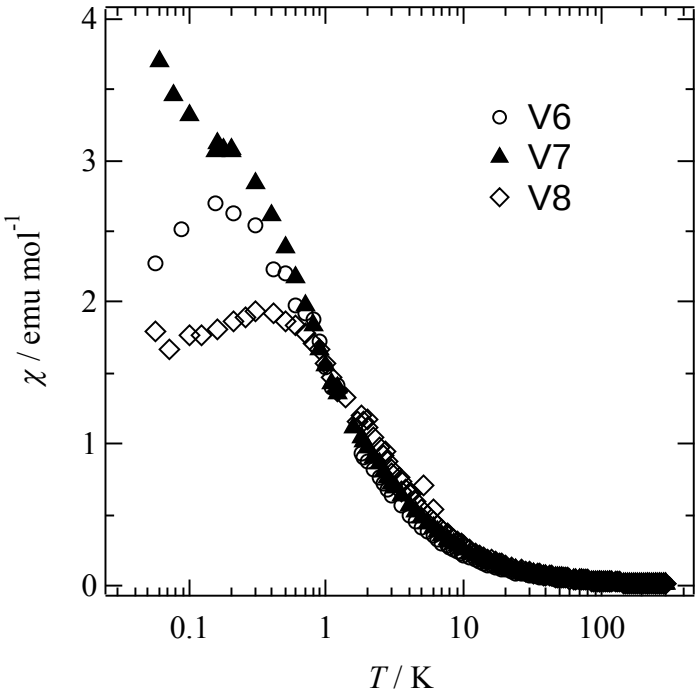

Figure 3.10: Temperature dependence of χ versus T plots. Low temperature region data (below 1.8 K) were estimated from ^{1}H-NMR spectra and high temperature region data (above 1.8 K) were recorded by SQUID magnetometer.

Field dependent NMR spectra were collected for V6 and V7 at 600 mK. The peak widths of both samples were proportional to the magnetic field (Figure 3.11(a) and (b)).

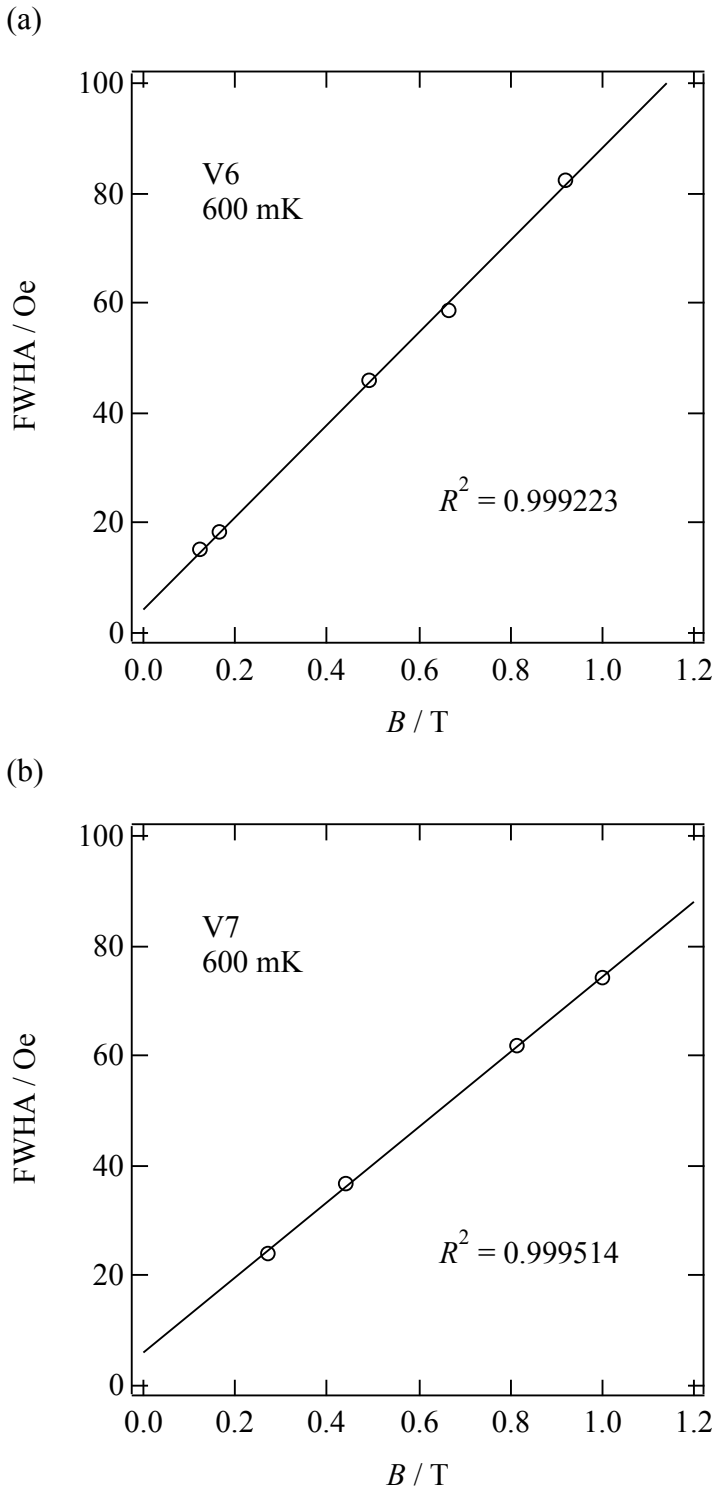

Figure 3.11: Magnetic field dependence of peak widths (FWHA) of V6 (a) and V7 (b) at 600 mK. Solid line is a straight-line approximation.

For V6, the resonance frequency dependence of the temperature dependent ^{1}H-NMR spectra was collected and the estimated magnetic susceptibility data are shown in Figure 3.12. The data were collected at 5.25 MHz (0.123 T), 7.10 MHz (0.166 T, Figure 3.7), and 28.31 MHz (0.665 T). As the magnetic field was increased, the magnetic susceptibility at low temperature region also increased. This behaviour suggests that the ground state of V6 was changed to a magnetic ground state by increasing the applied magnetic field above 0.2 T, as confirmed to micro-SQUID data (0.32 T, $S = 0 \rightarrow 1$).

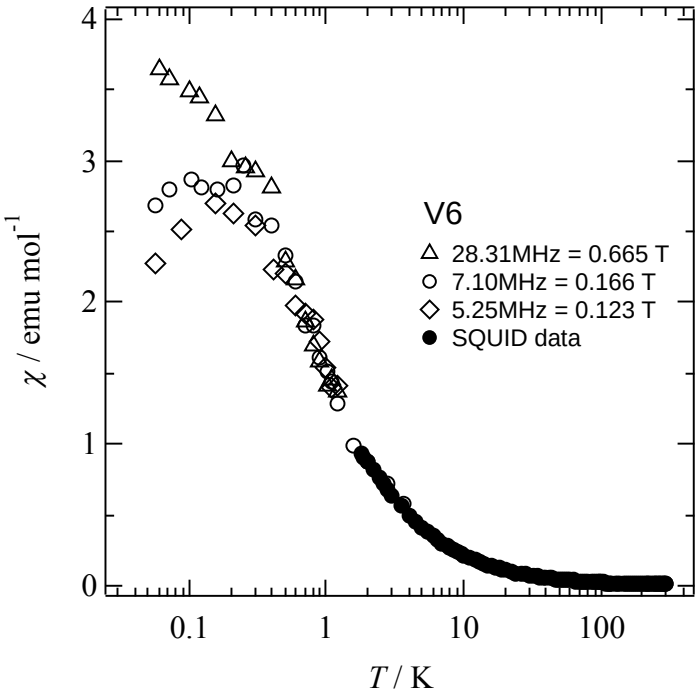

Figure 3.12: Magnetic field dependence of χ versus T plots of V6. Low temperature region data (below 1.8 K) were estimated from ^{1}H-NMR spectra, and high temperature region data (above 1.8 K, filled circles) were recorded by SQUID magnetometer.

^{1}H spin-lattice relaxation time (T_1) measurements. The ^{1}H spin-lattice relaxation times T_1 of the oxovanadium rings were measured. The nuclear spin-lattice relaxation rate T_1^{-1}, which is the reciprocal of T_1, showed temperature dependency. Both V6 and V7 showed enhancement of their T_1^{-1} values at low temperature, but V8 did not show any significant peaks (Figure 3.13-3.15).

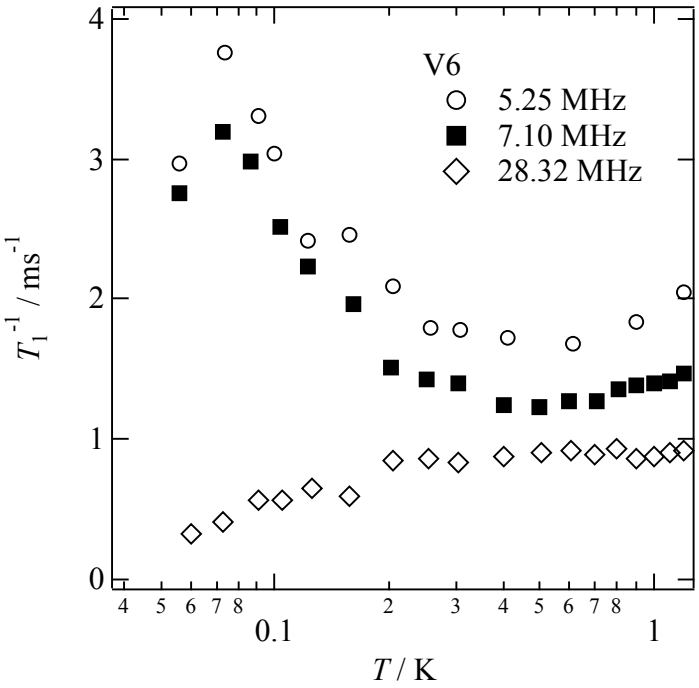

Figure 3.13: ^{1}H nuclear spin-lattice relaxation rate, T_1^{-1}, plotted as a function of temperature for the V6 at three different resonance frequencies: (○) 5.25 MHz, (■) 7.10 MHz, and (◇) 28.32 MHz.

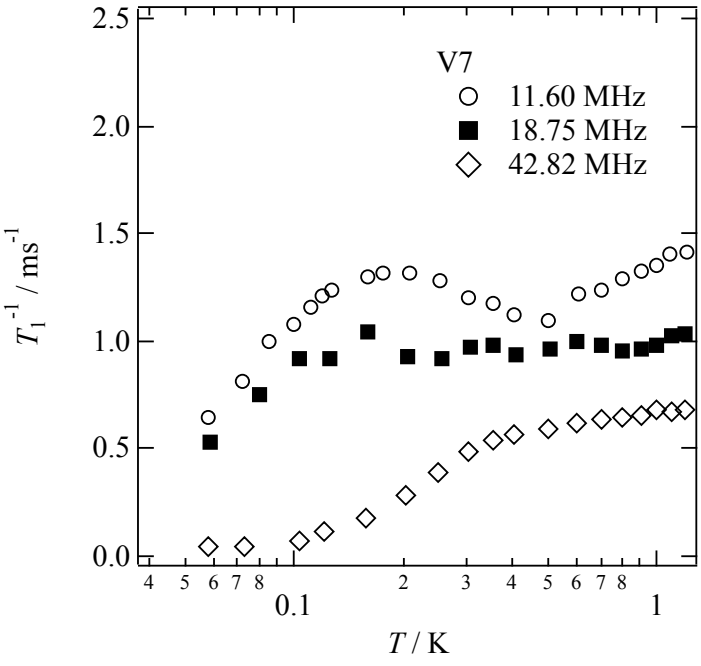

Figure 3.14: ^{1}H nuclear spin-lattice relaxation rate, T_1^{-1}, plotted as a function of temperature for the V7 at three different resonance frequencies: (○) 11.60 MHz, (■) 7.10 MHz, and (◇) 28.32 MHz.

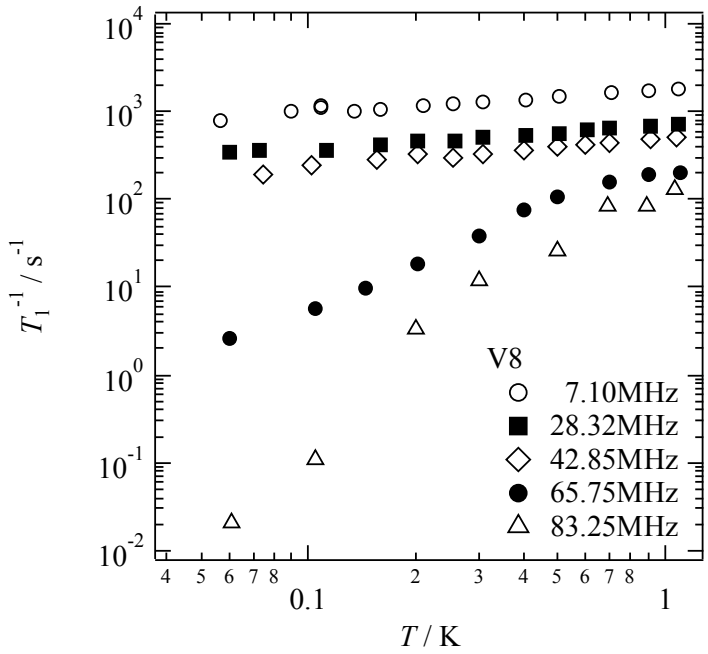

Figure 3.15: ^{1}H nuclear spin-lattice relaxation rate, T_1^{-1}, plotted as a function of temperature for the V8 at five different resonance frequencies: (○) 7.10 MHz, (■) 28.32 MHz, (◇) 42.85 MHz, (●) 65.75 MHz, and (△) 83.25 MHz.

To analyse the T_1^{-1} data, the Lorentzian-type expression, which is often called the BPP (Bloembergen-Purcell-Pound) model, was applied for the vanadium rings[5,9]

$$\frac{1}{T_1\chi T} = A\frac{\Gamma(T)}{\Gamma^2(T) + {\omega_N}^2} \tag{3.1}$$

where A is a fitting constant independent of both magnetic field and temperature, ω_N is the proton nuclear Larmor frequency, and $\Gamma(T)$ is the temperature dependent characteristic frequency of electron spin fluctuations which at low temperature is given by $\Gamma(T) \propto T^{\alpha}$. The scaling exponent α will be determined by a best-fit procedure applied to the experimental data. When the Γ is much larger than ω_N ($\Gamma >> \omega_N$), such as in the high temperature region (paramagnetic state), we can write

$$\frac{1}{T_1\chi T} \propto \frac{1}{\Gamma} \tag{3.2}$$

Thus, in the paramagnetic region, Γ is constant and it means that magnetic susceptibility is proportional to T_1^{-1}.

$$\frac{1}{T_1} \propto \chi T \tag{3.3}$$

T_1^{-1} versus T and χT versus T plots of V6, V7, and V8 are shown in Figure 3.16-18. Although V6 and V7 were well explained by BBP model, V8 did not show good agreement in the high temperature region. The reason for this may be related to the low-symmetry of the molecular structure of V8. The BPP model is useful for the simple approximation of spin-lattice relaxation time. Symmetry breaking effects induce degeneracy of spin ground states, resulting in deviations in relaxation time from simple theoretical estimations. The BPP model was applied for analyses of V6 and V7.

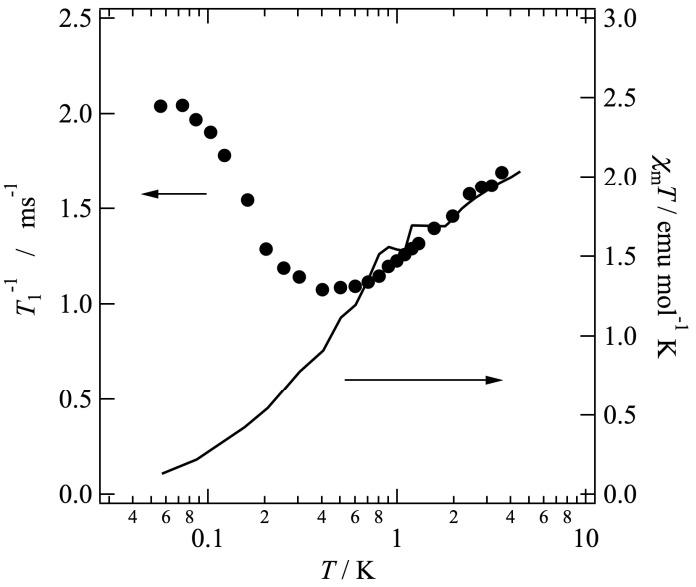

Figure 3.16: Temperature dependence of T_1^{-1} versus T plots (●; 7.10 MHz) and $\chi_m T$ versus T plots (solid line) of V6.

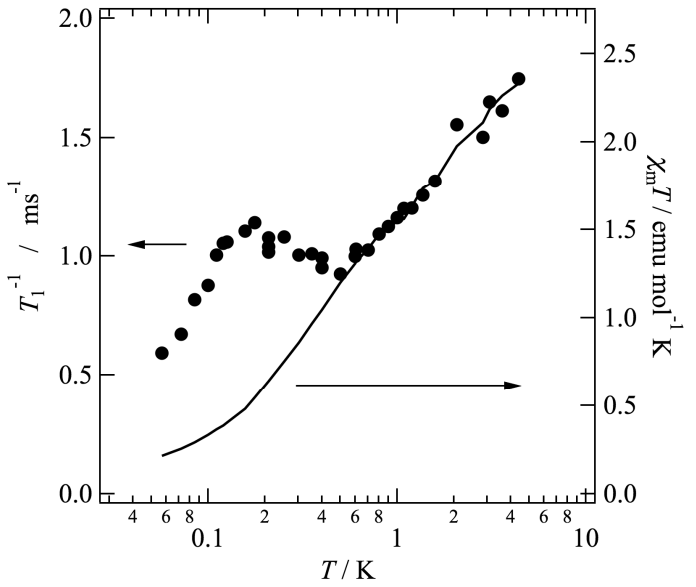

Figure 3.17: Temperature dependence of T_1^{-1} versus T plots (●; 11.60 MHz) and $\chi_m T$ versus T plots (solid line) of V7.

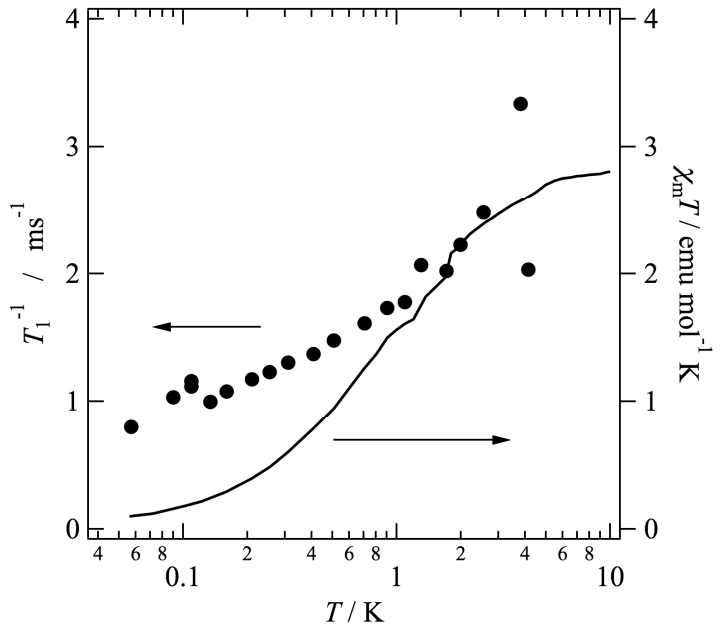

Figure 3.18: Temperature dependence of T_1^{-1} versus T plots (●; 7.10 MHz) and $\chi_m T$ versus T plots (solid line) of V8.

$1/T_1\chi T$ versus T plots of V6 and V7 are shown in Figure 3.19 (a) and (b). Both plots show enhancement of the $1/T_1\chi T$ values observed in the low temperature region. Although the data of V6 at all frequencies and the data of V7 at 42.85 MHz (1.006 T) showed good agreement with the theoretical curves, V7 showed a gap from the theoretical curves in the low magnetic field region (especially 18.75 MHz, 0.4403T), which may originate from spin frustration or level crossing effects.[4] According to the BPP model (Eq. (3.1)), the maximum position of the peak depends on ω_N, and a peak is observed when the Γ value is the same frequency as ω_N. The observed data at 18.75 MHz can be considered to have a peak at much lower temperature than that of the theoretical estimation, which suggests that the spin fluctuation does not freeze under low applied magnetic field. This observation is one of the magnetic features of odd-membered antiferromagnetic ring.

Γ versus T plots of V6 and V7 are shown in Figure 3.19 (c) and (d). Both complexes show plateaus above approximately 0.7 K, indicating that the magnetic state is paramagnetic. The fluctuation frequency of V6 in the paramagnetic region is larger than V7, showing that the magnetic interactions in V6 are stronger than those in V7 ($J_{V6} > J_{V7}$). When the sample was cooled, the Γ values showed decreased, and the spin fluctuations slow down as the temperature is taken below 0.7 K. The inclines of the slopes are proportional to the function of $T^{1.5}$ (dashed lines). This similarity of temperature dependences of Γ value is likely to arise due to the similarity of the molecular structures of the V6 and V7 rings.

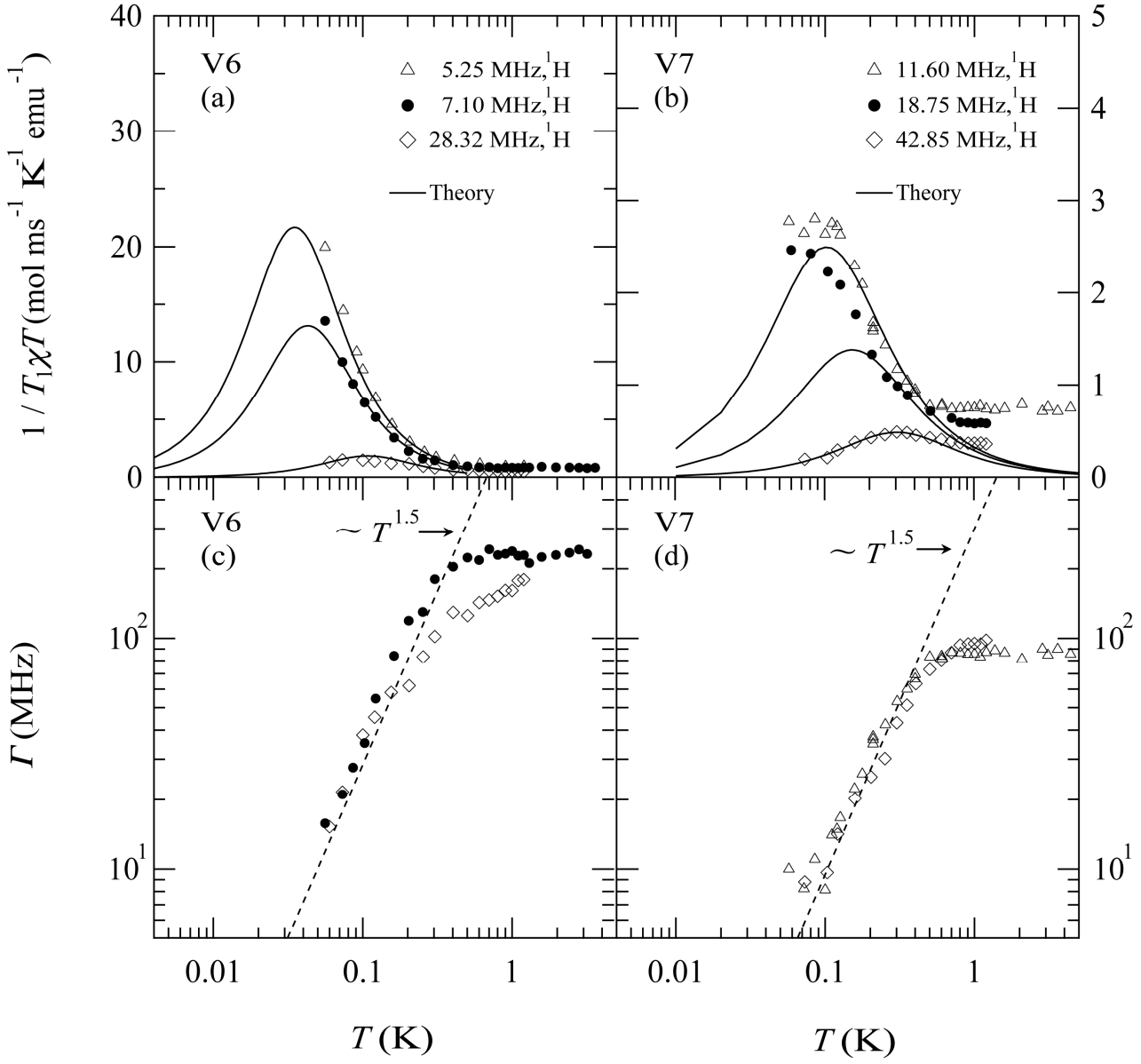

Figure 3.19: Comparison between the theory (solid lines) and experimental data (symbols) for $1/T_1\chi T$ versus T plots of V6 (a) and V7 (b). Γ versus T plots of V6 (c) and V7 (d). Dashed lines are power-law scaled.

3.4 Conclusion

Solid-state ^{1}H-NMR measurements of V6, V7, and V8 were conducted at very low temperature using the dilution refrigerator technique. The ^{1}H-NMR spectra showed single broad peaks for all systems and the peak widths showed temperature dependency. Magnetic susceptibilities were estimated from the FWHA of the peaks and suggesting that the ground states of V6 and V8 were spin singlet, while that of V7 was spin doublet, as conformed to the micro-SQUID experiments. Spin-lattice relaxation time, T_1, measurements also showed temperature dependency. The analyses of the fluctuation frequency of the electron spins on the vanadium ions showed to frequencies to decrease with decreasing temperature, with the relationship $\Gamma \propto T^{1.5}$. The $1/T_1\chi T$ versus T plots of V6 and V7 indicate enhancements of $1/T_1\chi T$ values in the low-temperature region for both complexes. While the $1/T_1\chi T$ versus T data of V6 showed a good agreement with the theoretical curves derived from BPP theory, V7 showed a gap from the theoretical curves under low magnetic fields. This deviation is likely to arise from the additional contributions of spin frustration and/or level crossing effects.

---

[1] Taft, K. L. & Lippard, S. J. Synthesis and Structure of [Fe(OMe)$_2$(O$_2$CCH$_2$Cl)], a Molecular Ferric Wheel. *J. Am. Chem. Soc.*, **112**, 9629-9630 (1990).

[2] Taft, K. L., Delfs, C. D., Papaefthymiou, G. C., Fomer, S., Gatteschi, D. & Lippard, S. J. [Fe(OMe)$_2$(O$_2$CCH$_2$Cl)], a Molecular Ferric Wheel. *J. Am. Chem. Soc.*, **116**, 823-832 (1994).

[3]van Slageren, J., Sessoli, R., Gatteschi, D., Smith, A. A., Helliwell, M., Winpenny, R. E. P., Cornia, A., Barra, A.-L., Jansen, A. G. M., Rentschler, E. & Timco, G. A. Magnetic Anisotropy of the Antiferromagnetic Ring [Cr$_8$F$_8$Piv$_{16}$]. *Chem.-Eur. J.*, **8**, 277-285 (2002).

[4] Affronte, M., Cornia, A., Lascialfari, A., Borsa, F., Gatteschi, D., Hinderer, J., Horvatic, M., Jansen, A. G. M. & Julien, M.-H. Observation of Magnetic Level Repulsion in Fe6:Li Molecular Antiferromagnetic rings. *Phys. Rev. Lett.*, **88**, 167201 (2002)

[5] Baek, S. H., Luban, M., Lascialfari, A., Micotti, E., Furukawa, Y., Borsa, F., van Slageren, J. & Cornia, A. Scaling behavior of the proton spin-lattice relazation rate in antiferromagnetic molecular rings. *Phys. Rev. B*, **70**, 134434 (2004).

[6] Geiβelmann, A., Klüfers, P., Kropfgans, C., Mayer, P. & Piotrowski, H. Carbohydrate–Metal Interactions Shaped by Supramolecular Assembling. *Angew. Chem., Int. Ed.*, **44**, 924-927 (2005).

[7] Hoshino, N., Nakano, N., Nojiri, H., Wernsdorfer, W. & Oshio, H. Templating Odd Numbered Magnetic Rings: Oxovanadium Heptagons Sandwiched by *β*-Cyclodextrins. *J. Am. Chem. Soc.*, **131** 15100–15101 (2009).

[8] Hoshino, N. Novel Quantum Spin Systems of Multi-nuclear Metal Complexes. *Ph.D. thesis*, *University of Tsukuba*, (2009).

[9] Rousochatzakis, I., Läuchli, A., Borsa, F. & Luban, M. Theory of severe slowdown in the relaxation of ring and clusters with antiferromagnetic interactions. *Phys. Rev. B*, **79**, 064421 (2009).

CHAPTER 4

Syntheses and Magnetic Properties of Triangular Complexes

4.1 Introduction

Odd-membered antiferromagnetic rings have been attracting great interest due to their potential to exhibit spin frustration, non-colinear spin states and the existence of spin chirality. In particular, the magnetic properties of odd-membered antiferromagnetic rings with $S = 1/2$ spins have been extensively studied for three membered rings. For triangular systems, half step magnetization and hysteresis curves originating from spin chirality were observed in the antiferromagnetically coupled Cu^{II}_3 polyoxometalate sandwich complex $Na_9[Cu_3Na_3(H_2O)_9(\alpha\text{-}AsW_9O_{33})_2)$ (Figure 4.1 (a)).[1] The magnetization curve collected by the application of a rapidly pulsed field showed asymmetry between the positive and negative field regions (Figure 4.1 (b)). Several [Cu3]-type molecules have been synthesized by molecular design, and their magnetic behaviours have been investigated, motivated by interests in quantum spin.[2,3,4]

(a) (b)

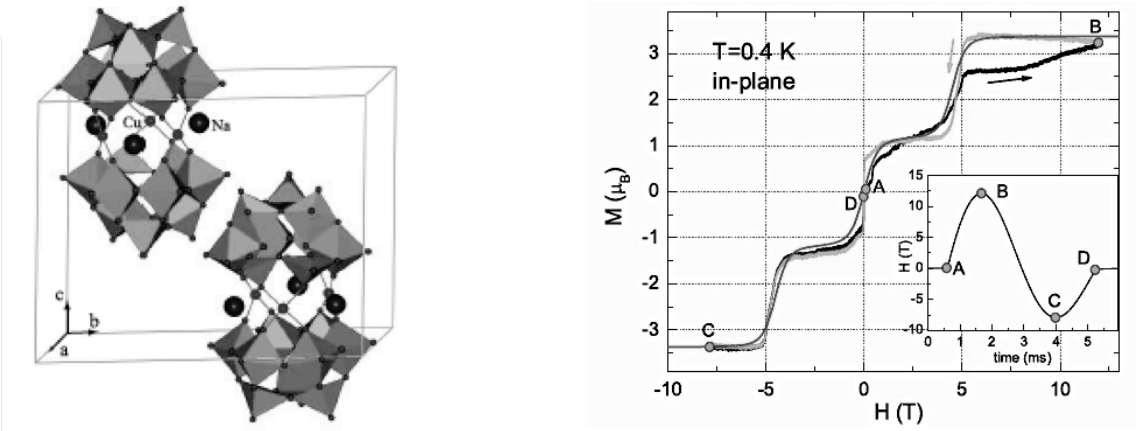

Figure 4.1: (a) The crystal structure of $Na_9[Cu_3Na_3(H_2O)_9(\alpha\text{-}AsW_9O_{33})_2]$. (b) Magnetization curve versus pulsed magnetic field at 0.4 K. The insert shows the pulsed magnetic field versus time.

Frustrated spin models in one dimension have attracted attention for both the uniqueness of their characteristics and the diversity of their properties. In contrast to higher dimensional spin systems, quantum spin chains have no long-range order. If there is no frustration like an antiferromagnetic ladder with an even number of legs, antiferromagnetic spin ladders with $S = 1/2$ spins are expected to have an excitation gap. When frustration is present, the Lieb-Schultz-Mattis theorem suggests that the spin gap must be accompanied with at least doubly degenerate ground states.[5] Three-leg spin tubes have a triangular column type structure, and antiferromagnetic interactions are operative between the spins. Although the theory of spin tube is well studied and the expected physical properties are interesting from a fundamental viewpoint, there are only few examples of compounds with triangular column type structures.[6,7,8] As a first example of three-leg spin tube with $S = 3/2$,

the inorganic chromium inorganic ($CsCrF_4$, Cr^{3+}; $S = 3/2$) was reported in 2009.[9] The space group of $CsCrF_4$ is $P\bar{6}2m$, and identical Cr3 equilateral triangles are stacked without rotation along the *c* axis (Figure 4.2 (a)). The distance between Cr ions in the equilateral triangle is 3.741 Å, while that along the *c* axis is 3.857 Å. The magnetic susceptibility data shows that antiferromagnetic interactions are operative between the chromium ions and the Weiss temperature is -143 K. The specific heat capacity shows there is no magnetic phase transition below 4 K (Figure 4.2 (b)). The *C*/*T* curve tends to a non-zero value at 0 K, and suggests that this compound has a gapless spin-liquid state, the so-called Tomonaga–Luttinger liquid.

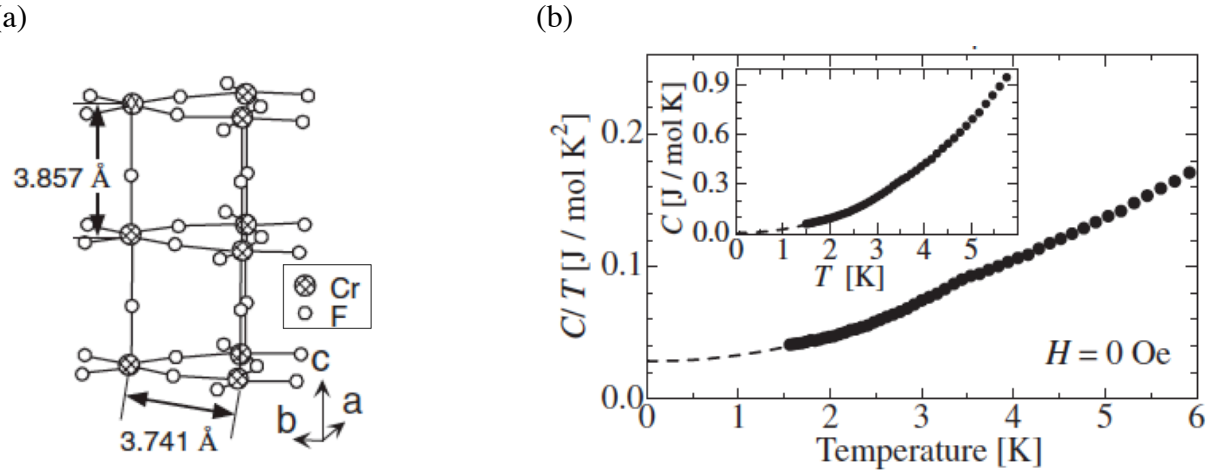

Figure 4.2: (a) The crystal structure of $CsCr_3F_4$. (b) Temperature dependence of heat capacity under zero magnetic field. The inset shows temperature dependence of specific heat capacity. The dashed lines are extrapolated lines.

Spin tube with divalent copper ions, $[Cl(CuCl_2tachH)_3]^{2+}$, (tach = *cis*, *trans*-1,3,5-triamino-cyclohexane) was reported in 2004 by Cronin et al. and the physical properties have been well studied (Figure 4.3 (a)).[10,11] This Cu3 spin tube shows weak antiferromagnetic interactions between Cu(II) ions in the intra-triangular units, and has moderate antiferromagnetic interactions between Cu(II) ions of neighbouring Cu3 triangle units. Therefore, the spin system can be regarded as three weakly antiferromagnetic-coupled chains. Magnetization measurements at low temperature suggest this system shows gapless Tomonaga-Luttinger liquid ground state, although the theoretical prediction did indicate the existence of a spin gap. In order to access a novel quantum phase, fine-tuning of the magnetic interactions and spin topology is important.

In another example, a dabco (= 1,4-diazabicyclo[2.2.2]octane) bridged-type copper spin tube structure *catena*-$[Cu_3(L1)_3(dabco)_3] \cdot 3Et_2O$ (H_2L1 = 1,1-(1,4-phenylene)-bis(4,4-dimethylpentane-1,3-dione)) was reported in 2006.[12] The planar triangular moiety consists of three copper(II) ions and three bis-β-diketone type bridging ligands, and the trinuclear metallocycles are bridged by dabco moieties. Although this three-leg spin tube is not a twisted structure, the space group is $P2_1/m$, i.e. has no crystallographic C_3 axis. In this system, the physical properties appear likely to be very interesting but only the structure was reported. The structure may be a useful building unit for spin tube systems.

(a) (b)

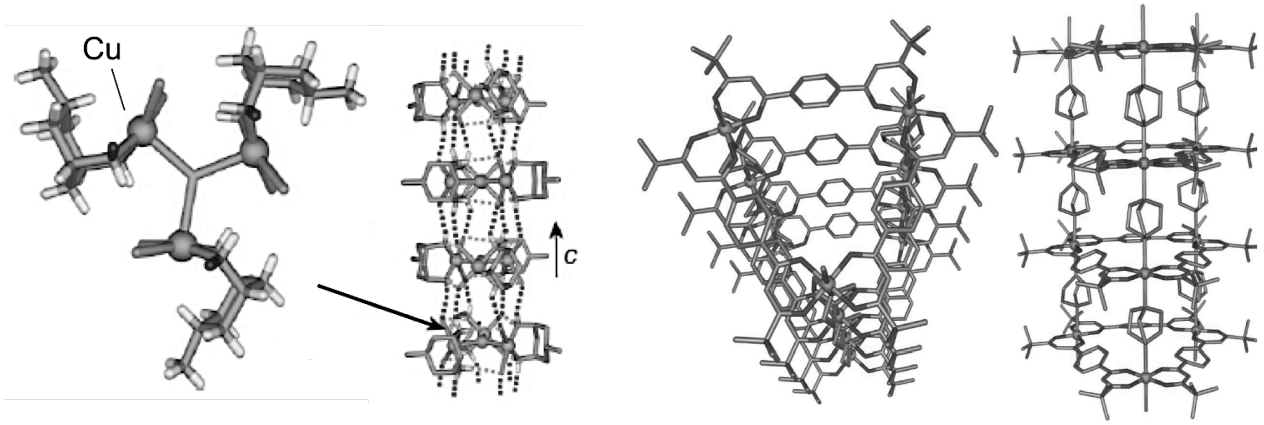

Figure 4.3: (a) The Crystal structure of $[Cl(CuCl_2tachH)_3]^{2+}$ (left) and a representation of the 1-D chains formed between the $\{Cu^{II}_3Cl\}$ cluster units that run parallel to the *c* axis (right). (b) Two schematic representation of a fragment of the trigonal prismatic species *catena*-$[Cu_3(L1)_3(dabco)_3] \cdot 3Et_2O$.

In this chapter, the rational synthesis and magnetic properties of triangular metal complexes with highly planar structures were studied. A new guanidine-derived ligand, $H_3L_{gu}Cl$, was prepared and its copper and nickel complexes were synthesized. This ligand has three planar tetra-dentate coordination sites and can coordinate the equatorial positions of transition metal ions, suggesting that it may be a useful building block for planar triangle complexes (Scheme 4.1).[13]

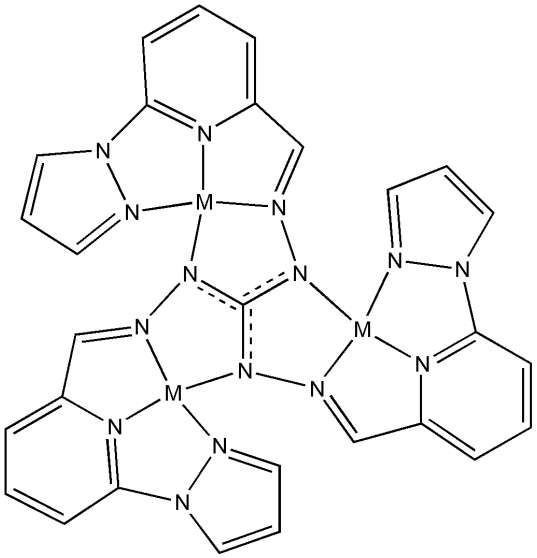

Scheme 4.1: The expected structure of the triangular complex with the novel guanidine derivative ligand. M indicates transition metal ions.

4.2 Experiments

Experimental Procedures

X-ray Crystallography: A single crystal was removed from the mother liquor, mounted on a glass rod and intensity data was collected using a Bruker SMART or SMART APEX II CCD systems with Mo-Kα radiation ($\lambda = 0.71073$ Å). The structure was solved by direct methods and refined by full-matrix least-square techniques on F^2 using SHELXTL.

Magnetic Measurements: Magnetic susceptibility data with an applied magnetic field of 500 Oe were collected using a Quantum Design MPMS-5S SQUID magnetometer. Magnetic data were corrected for the diamagnetism of the sample holder and for the diamagnetism of the sample using Pascal's constants.

NMR measurements: ^{1}H-NMR spectra were measured on a Bruker AVANCE400 spectrometer at room temperature. Chemical shifts in NMR were reported in ppm (δ), relative to the internal standard of tetramethylsilane (TMS). The signals observed were described as s (singlet), d (doublet), t (triplet), m (multiplets). The number of protons (n) for a given resonance is indicated as nH. Coupling constants are reported as J in Hz.

Elemental analysis: Elemental analyses were performed using a Perkin Elmer 2400 element analyzer.

Synthetic Procedures: All chemicals were used without further purification except when noted. Diethyl ether was distilled over calcium hydride then sodium/benzophenone.

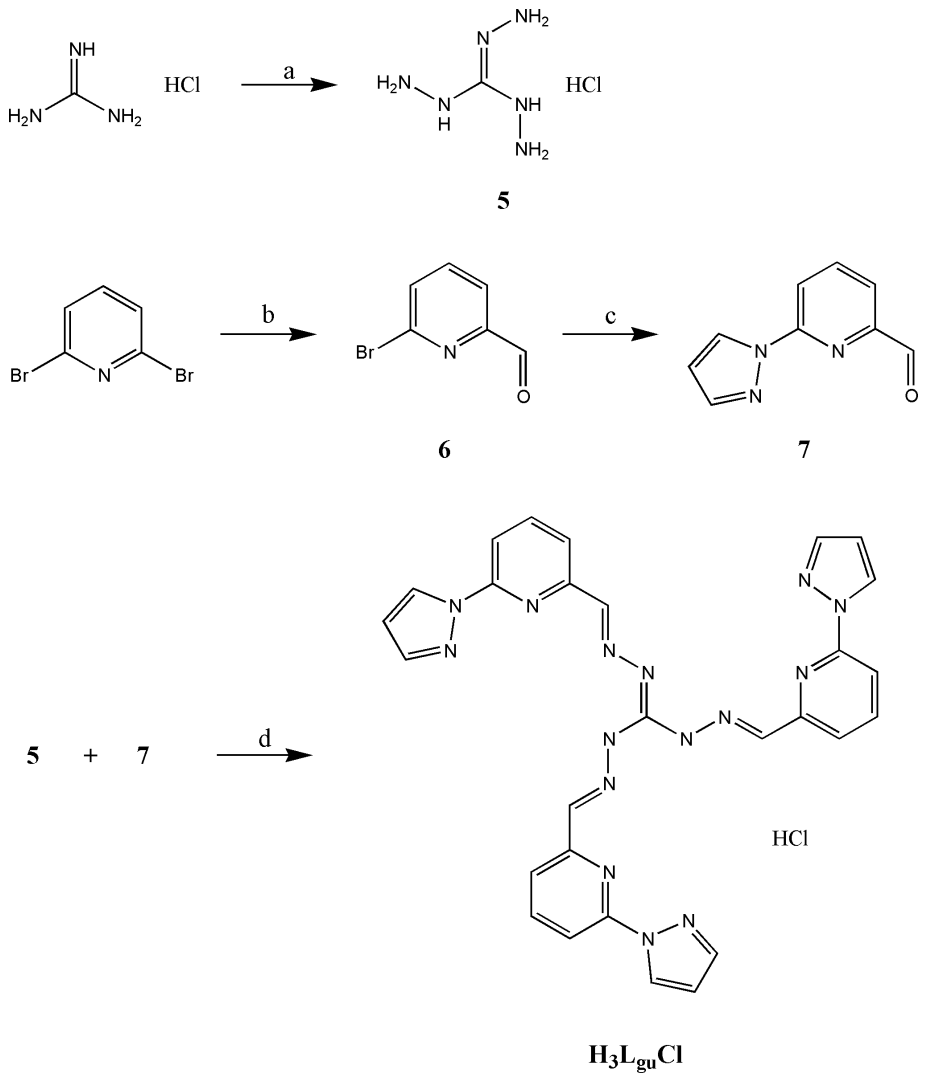

$H_3L_{gu}Cl$

Scheme 4.2: Synthetic scheme of $H_3L_{gu}Cl$. a; $N_2H_4 \cdot H_2O$, 1,4-dioxane. b; *n*-BuLi, DMF, Et_2O, 68 %. c; pyrazole, 1,10-phenanthroline monohydrate, CuI, K_2CO_3, toluene, 79 %. d; EtOH.

Preparation of 1,2,3-triaminoguanidinium chloride (5)[14]

To a suspension of guanidinium chloride (1.91 g, 20 mmol) in 1,4-dioxane (10 ml) was added hydrazine monohydrate (3.41 g, 68 mmol) with stirring. The mixture was heated under reflux for two hours. After the mixture cooled to ambient temperature, the product was collected by filtration, washed with 1,4-dioxane, and dried to give **5** as a white crystalline solid.

Preparation of 6-bromo-2-pyridinecarboxaldehyde (6)[15]

2,6-dibromopyridine (19.0 g, 80.0 mmol) was dissolved in anhydrous diethyl ether (150 cm^3) under a nitrogen atmosphere. The solvent was cooled down to -78 °C and *n*-buthyl lithium (2.6 M in hexane) (30.7 cm^3, 80.0 mmol) was added slowly, keeping under -60 °C. After addition was complete, the reaction mixture was allowed to warm to -40 °C for fifteen minutes, and cooled down

to -78 °C again. Anhydrous *N*,*N*-dimethylformamide (6.74 cm^3, 88.0 mmol) was added, ensuring that the reaction temperature did not exceed -70 °C. The mixture was stirred for two hours at -78 °C, before the reaction was quenched by the addition of 6 M hydrochloric acid. (30 cm^3). The organic phase was collected and dried over anhydrous magnesium sulfate. After evaporating the solvent, the residue was purified by column chromatography on a silica gel (eluting with dichloromethane) to give **6** (10.1 g, 54.3 mmol, 68 % yield) as a crystalline white solid: ^{1}H-NMR ($CDCl_3$) δ 10.01 (s, 1H), 7.93 (dd, 1H, J = 6.4 Hz, 1.8 Hz), 7.76 (dd, 1H, J = 8.0 Hz), 7.73 (dd, 1H, J = 7.8 Hz, 1.8Hz).

Preparation of 6-(1H-pyrazol-1-yl)-2-pyridinecarboxaldehyde (**7**)[16]

A mixture of **6** (5.58 g, 30.0 mmol), pyrazole (2.66 g, 39.0 mmol), 1,10-phenanthroline monohydrate (1.19 g, 6.00 mmol), CuI (1.25g, 3.00 mmol), and K_2CO_3 (4.56 g, 30.0 mmol) was suspended in toluene (120 cm^3) and refluxed for one day. After cooling to room temperature, the mixture was filtered through celite, and the solvent was removed in *vacuo*, and the residue was purified by silica gel chromatography (eluting with dichloromethane/ethyl acetate = 40:1) to give **7** (4.08 g, 23.6 mmol, 79 % yield) as a white solid: ^{1}H-NMR ($CDCl_3$) δ 10.05 (s, 1H), 8.68 (d, 1H, J = 6.6 Hz), 8.23 (d, 1H, J = 8.4 Hz), 7.99 (dd, 1H, J = 8.0 Hz), 7.84 (d, 1H, J = 7.4 Hz), 7.78 (s, 1H), 6.52 (dd, 1H, J = 2.6 Hz, 2.2 Hz). Anal. (calc.) for $C_9H_7N_3O$ (**7**): C, 62.68 (62.42); H, 4.15 (4.07); N, 24.26 (24.26)%.

Preparation of 1,2,3-tris[(6-(1H-pyrazol-1-yl)pyrid-2-ylmethylene)amino]guanidinium chloride ($H_3L_{gu}Cl$)

5 (469 mg, 0.33 mmol) was dissolved in water (5 cm^3) and ethanol solution (50 cm^3) **7** (1.90 g, 1.10 mmol) was added into the aqueous solution, resulting in the production of white precipitate. The suspension was stirred for three hours at room temperature and the precipitate was collected by filtration, washed with ethanol and diethyl ester, and dried to give $H_3L_{gu}Cl$ (2.32 g) as a pale yellow powder.

Preparation of $[Cu_3L_{gu}Cl_3]Cl\cdot 8H_2O$ ($[Cu_3]\cdot 8H_2O$)

$H_3L_{gu}Cl$ (80 mg, 0.13 mmol) in water (10 mL) was added into $CuCl_2\cdot 2H_2O$ (70 mg, 0.41 mmol) in water (5 mL). After two weeks, brown needle crystals of $[Cu_3]\cdot H_2O$ were collected by filtration (48 mg, 0.047 mmol, 37 % yield). Anal. (calc.) for $C_{28}H_{35}N_{15}Cl_4Cu_3O_7$ ($[Cu_3]\cdot 7H_2O$): C, 32.78 (32.77); H, 3.28 (3.44); N, 20.29 (20.48)%

Preparation of $[Ni_3L_{gu}(CH_3OH)_5H_2O](BF_4)_4\cdot CH_3OH$ ($[Ni_3]\cdot CH_3OH$)

$H_3L_{gu}Cl$ (20 mg, 0.033 mmol) and $Ni(BF_4)_2\cdot 6H_2O$ (34 mg, 0.10 mmol) were dissolved in methanol (5 mL). The mixture was heated and stirred for ten minutes, then cooled to ambient temperature. Diisopropyl ether was allowed to diffuse into the solution, resulting in the formation of yellow block-like crystals of $[Ni_3]$, which were collected by filtration (28.5 mg, 0.0219 mmol, 66 % yield). Anal. (calc.) for $C_{29}H_{35}N_{15}B_4Cu_3F_{16}O_6$ ($[Ni_3]$-$4CH_3OH$+$5H_2O$): C, 28.55 (28.72); H, 3.12 (2.91); N, 17.64 (17.32)%.

Table 4.1: Table of crystallographic parameters for [Cu_3] and [Ni_3].

	[Cu_3]	[Ni_3]
Formula	$C_{28}H_{37}Cl_4Cu_3N_{15}O_8$	$C_{34}H_{47}B_4F_{16}N_{15}Ni_3O_7$
F.W.	1044.15	1301.24
Space Group	$P2_1/n$ (No.14)	$P\bar{1}$ (No.2)
a / Å	11.665(3)	10.0521(8)
b / Å	6.7814(15)	11.4299(9)
c / Å	48.532(11)	22.6136(18)
α / °	-	77.6660(10)
β / °	94.167(4)	83.379(2)
γ / °	-	83.524(2)
V / Å^3	3828.8(15)	2510.9(3)
Z	4	2
T / K	100	100
μ / mm^{-1}	2.001	1.235
λ / Å	0.71073	0.71073
$R1$ ($> 2\sigma$)	0.0907	0.0862
$wR2$ ($> 2\sigma$)	0.2249	0.2077
Gof	1.022	1.054

[a] $R1 = \sum | |F_o| - |F_c| | / \sum |F_o|$. [b] $wR2 = \{ \sum [w(F_o^2 - F_o^2)^2] / \sum [w(F_o^2)^2] \}^{1/2}$.

Table 4.2: Selected bond lengths (Å) for [Cu_3].

Cu(1)-N(1)	2.045(7)	Cu(2)-N(5)	1.978(7)	Cu(3)-N(10)	1.959(7)
Cu(1)-N(3)	1.944(7)	Cu(2)-N(6)	2.039(7)	Cu(3)-N(11)	2.039(7)
Cu(1)-N(4)	1.977(7)	Cu(2)-N(8)	1.958(7)	Cu(3)-N(13)	1.945(7)
Cu(1)-N(15)	1.989(7)	Cu(2)-N(9)	1.975(7)	Cu(3)-N(14)	1.977(7)
Cu(1)-Cl(1)	2.644(2)	Cu(2)-Cl(2)	2.503(2)	Cu(3)-Cl(3)	2.700(3)

Table 4.3: Selected bond lengths (Å) for [Ni_3].

Ni(1)-N(1)	2.114(6)	Ni(2)-N(5)	2.047(5)	Ni(3)-N(10)	2.057(5)
Ni(1)-N(3)	2.003(6)	Ni(2)-N(6)	2.147(6)	Ni(3)-N(11)	2.132(6)
Ni(1)-N(4)	2.021(5)	Ni(2)-N(8)	1.992(5)	Ni(3)-N(13)	1.997(6)
Ni(1)-N(15)	2.067(5)	Ni(2)-N(9)	2.034(5)	Ni(3)-N(14)	2.023(5)
Ni(1)-O(1)	2.104(5)	Ni(2)-O(3)	2.067(5)	Ni(3)-O(5)	2.063(5)
Ni(1)-O(2)	2.102(5)	Ni(2)-O(4)	2.128(5)	Ni(3)-O(6)	2.105(5)

4.3 Results and Discussion

Structures. [Cu_3] crystallized in the $P2_1/n$ space group and the structural data were collected at 100 K. [Cu_3] has a planer trinuclear triangular core, consisting of three copper ions (Figure 4.4 (a)). All copper ions are square pyramidal geometry and show elongated-type Jahn-Teller distortion with the elongated axis lying perpendicular to the ligand plane. The coordination bond lengths, charge balance and coordination geometries of copper ions suggest that the all copper ions are divalent. Chloride ions coordinate the copper ions as axial ligands. The ligand, L_{gu}^{2-}, coordinates the equatorial position of all copper ions and bridging them. The distances between the copper ions are Cu1-Cu2 = 4.835 Å, Cu2-Cu3 = 4.803 Å and Cu3-Cu1 = 4.836 Å, respectively. The structure suggests that strong antiferromagnetic interactions are operative between the metal ions through Cu-N-N-Cu magnetic pathways.

[Ni_3] crystallized in the $P\bar{1}$ space group and the structural data were collected at 100 K. [Ni_3] also has a similar trinuclear triangular core, consisting of three nickel ions, and four tetrafluoroborate ions were included in the crystal lattices as counter anions (Figure 4.4 (b)). The distances between the nickel ions are Ni1-Ni2 = 4.960 Å, Ni2-Ni3 = 4.988 Å and Ni3-Ni1 = 4.996 Å, respectively. All nickel ions have six-coordinate octahedral coordination geometries suggesting that all nickel ions are divalent and in their HS state (S = 1). All nickel centres are coordinated in a meridonal fashion by the N-donor atoms of the ligand and by two oxygen atoms from solvent molecules. The Ni1 ion is coordinated by one water and one methanol molecule in the apical positions, while Ni2 and Ni3 ions are coordinated by two methanol molecules.

Overall, the guanidine derivative ligand, $H_3L_{gu}Cl$, could form the $[M_3L_{gu}]^{n+}$ (M; metal ion) type structure. Guanidine has two single bonds and one double bond between the nitrogen and carbon atoms. In this system, the bond lengths between the centre carbon atom (C28) and nitrogen atoms are C28-N5 = 1.345 Å, C28-N10 = 1.360 Å, and C28-N15= 1.373 Å for [Cu_3] and C28-N5 = 1.359 Å, C28-N10 = 1.375 Å, and C28-N15= 1.368 for [Ni_3], respectively. These bond lengths are intermediate between single and double bonds, and show that the C=N double bond in both complexes is delocalized between the four atoms. Therefore, all carbon and nitrogen atoms form sp^2-like hybrid orbitals, and complexes with highly planar structures were produced.

The crystal packing structures of both triangles are shown in Figure 4.5. The coordinated solvent molecules and counterions prevent the formation of spin-tube-like structures.

(a)

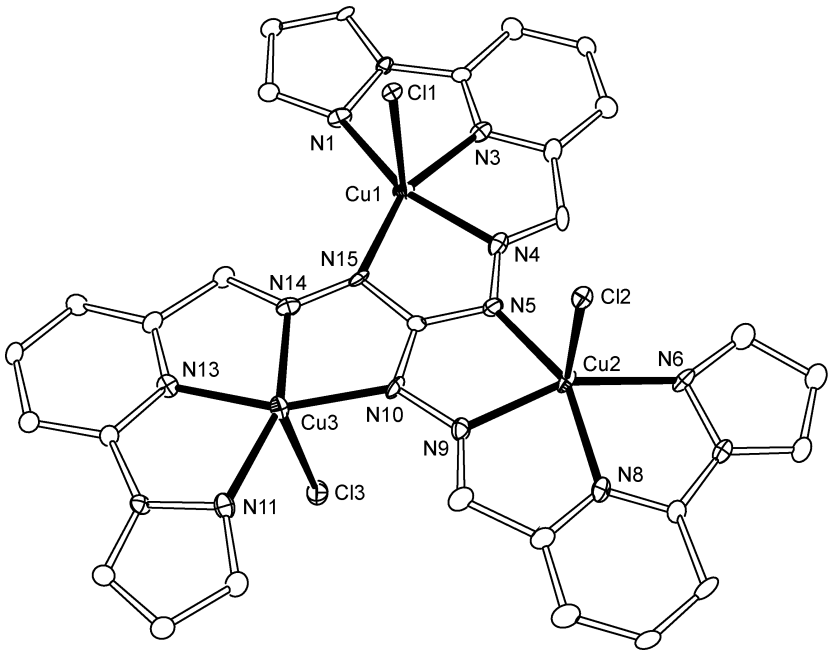

(b)

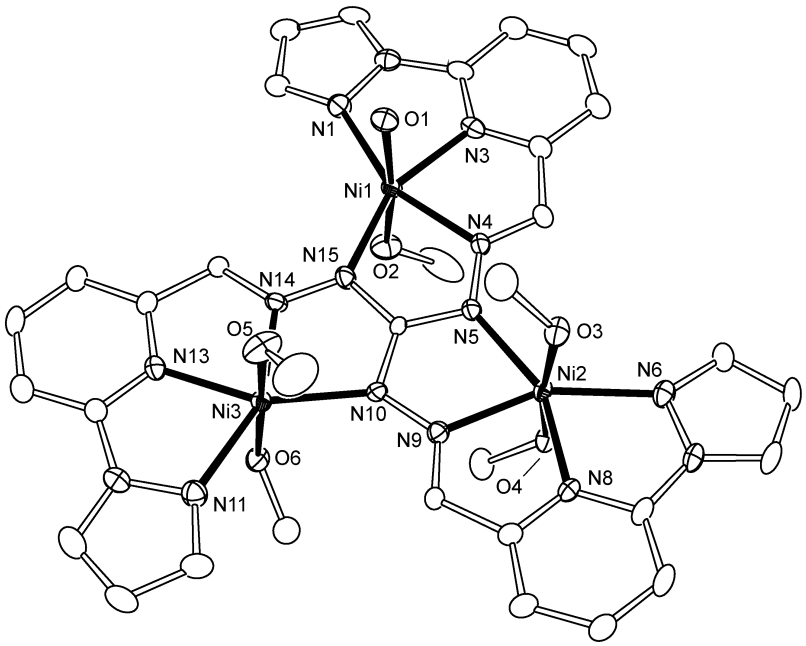

Figure 4.4: ORTEP diagram of [Cu_3] (a) and [Ni_3] (b) at 100 K. Thermal ellipsoids are at 30 % probability. Counter anions, hydrogen atoms and solvent molecules have been omitted for clarity.

(a)

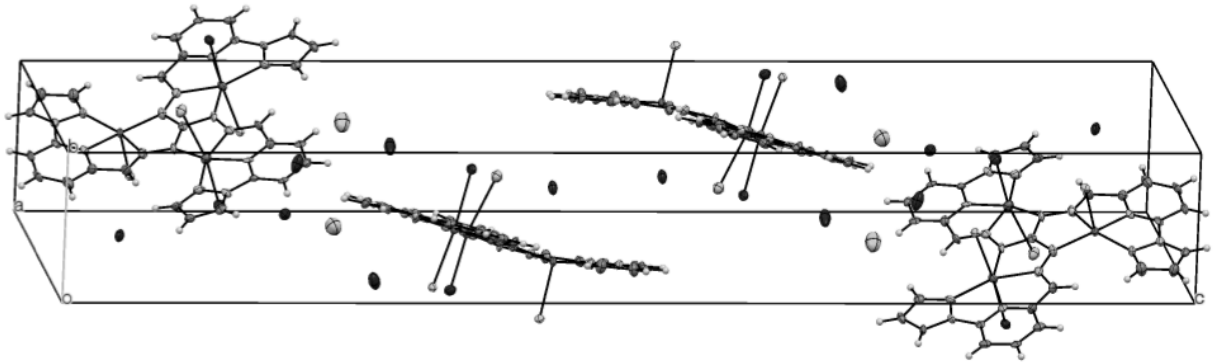

(b)

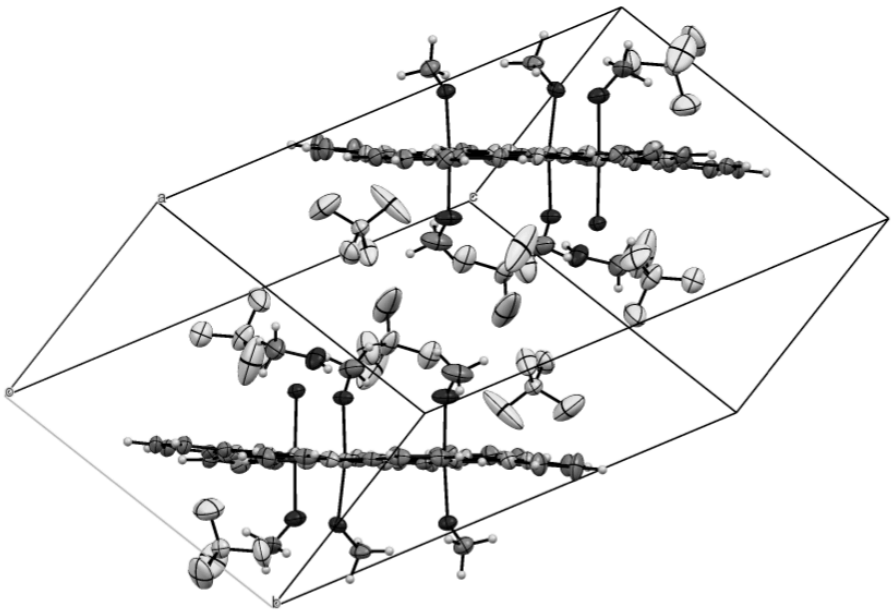

Figure 4.5: Crystal packing diagram of [Cu_3] (a) and [Ni_3] (b).

Magnetic properties. DC magnetic susceptibility data of [Cu_3] and [Ni_3] were measured in the temperature range of 1.8 – 300 K under an applied magnetic field of 500 Oe and the $\chi_m T$ versus T plots are shown in Figure 4.6. The $\chi_m T$ value of [Cu_3] at 300 K was 0.622 emu mol^{-1} K, and decreased with cooling to reach a plateau blow 130 K. The $\chi_m T$ value of [Cu_3] at 100 K was 0.411 emu mol^{-1} K, close to the spin only value of 0.375 emu mol^{-1} K (g = 2.00), expected for the isolated spin of one Cu^{II} ion (S = 1/2). The $\chi_m T$ value of [Ni_3] at 300 K was 3.20 emu mol^{-1} K, slightly larger than the spin only value of 3.00 emu mol^{-1} K (g = 2.00), calculated from the sum of the uncorrelated spins of three Ni^{II} ions (S = 1). The $\chi_m T$ value also showed decrease with decreasing of temperature. The $\chi_m T$ value of 1.8 K was 0.039 emu mol^{-1} K, suggesting that the spin ground state of [Ni_3] at low temperature is spin singlet. The triangular model spin Hamiltonian of $H = -2J(\boldsymbol{S}_1 \cdot \boldsymbol{S}_2 + \boldsymbol{S}_2 \cdot \boldsymbol{S}_3 + \boldsymbol{S}_3 \cdot \boldsymbol{S}_1)$, where J represents the exchange of coupling constant between metal ions, was used to analyse the magnetic susceptibility data of [Cu_3] and [Ni_3] (Scheme 4.3). The solid lines are the least square fits and the parameters for [Cu_3] are g = 2.08(1), J = -130(1) cm^{-1}, and for [Ni_3] are g = 2.18(1), J = -14.9(1) cm^{-1}, showing that strong antiferromagnetic interactions are operative between the metal ions, respectively.

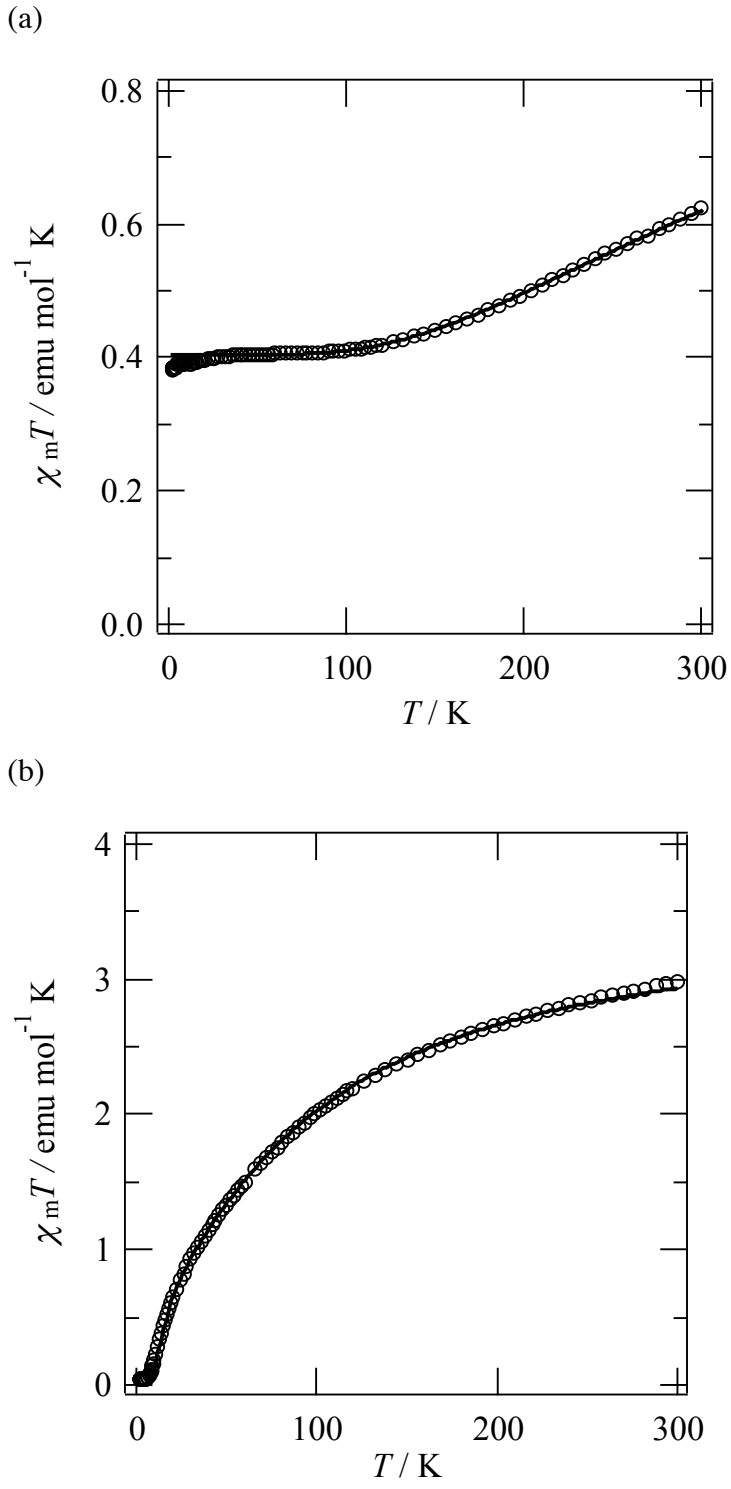

Figure 4.6: Temperature dependence of magnetic susceptibility data of [Cu_3] (a) and [Ni_3] (b). Solid lines are fitting curve.

Scheme 4.3: Regular triangle model spin Hamiltonian.

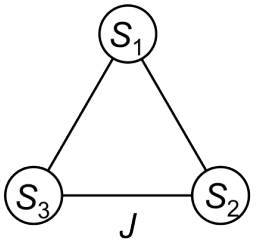

Cu^{II}: $S_1 = S_2 = S_3 = 1/2$

Ni^{II}: $S_1 = S_2 = S_3 = 1$

$$H = -2J(\boldsymbol{S}_1 \cdot \boldsymbol{S}_2 + \boldsymbol{S}_2 \cdot \boldsymbol{S}_3 + \boldsymbol{S}_3 \cdot \boldsymbol{S}_1)$$

The field-dependence of magnetization data for [Cu_3] at 1.8 K is shown in Figure 4.7 (a). The magnetic moment of [Cu_3] at 5 T reached 0.974 Nβ, suggesting that the ground state of [Cu_3] is S_T = 1/2. The magnetization curve was analysed using an S = 1/2 Brillouin function and the estimated curve is shown as a solid line. The observed data are slightly lower than the estimated curve across the majority of the applied magnetic fields, suggesting that weak antiferromagnetic interactions are likely to be operative between neighbouring triangular molecules at low temperature. Calculated magnetization curves of [Cu_3] at 1.8 K, estimated from a regular triangle model with the above-mentioned g and J values are shown in Figure 4.8. At low magnetic fields, the ground state S_T = 1/2 is strongly stabilized and the next level crossing point (to S_T = 3/2) is estimated to occur at 280 T. The magnetic moment of [Ni_3] at 5 T was 0.068 Nβ, showing that the ground state of [Ni_3] is S = 0 (Figure 4.7 (b)). The calculated magnetization curves of [Ni_3] at 1.8 K showed that level crossing is estimated to occur at 19.6 T (S_T = 0 → 1), 41.2 T (S_T = 1 → 2), and 61.8 T (S_T = 2 → 3) (Figure 4.9).

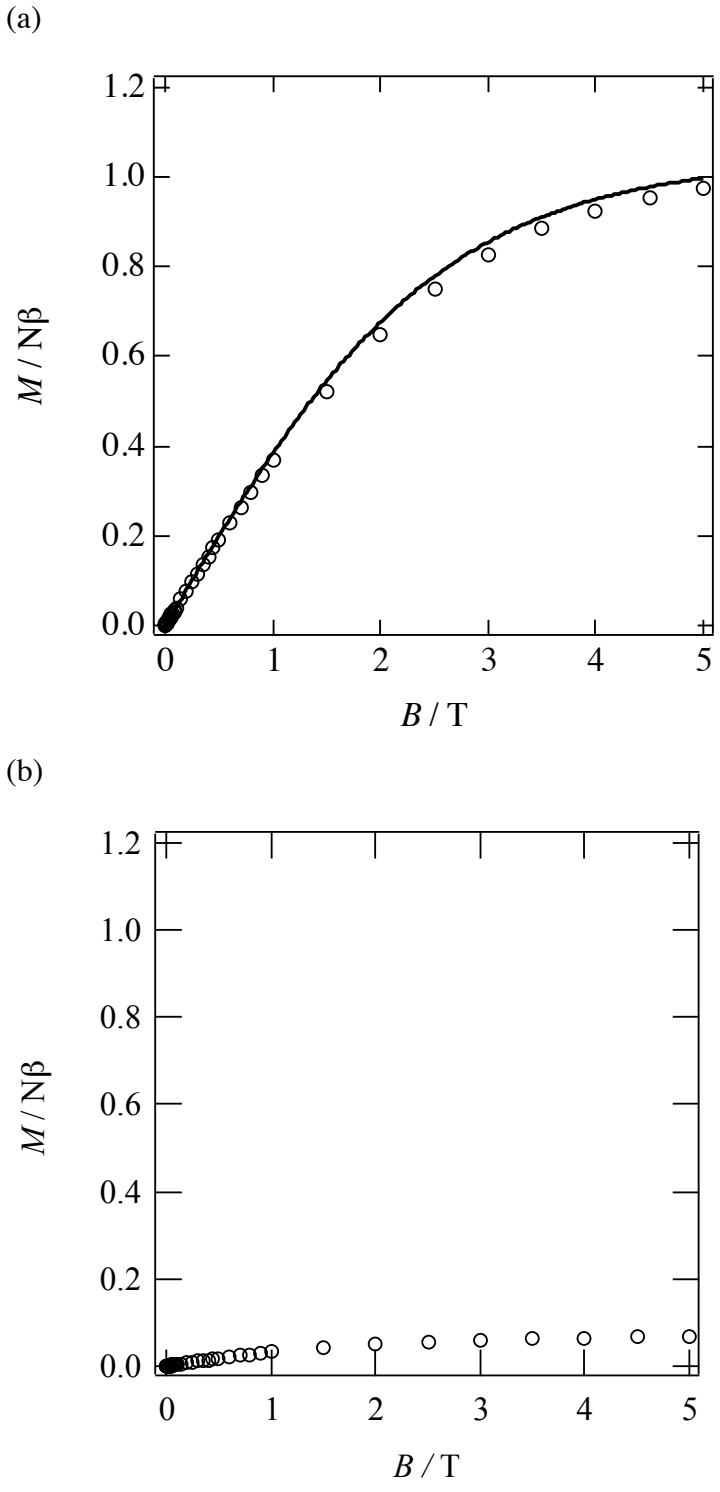

Figure 4.7: Field-dependence of magnetization curves at 1.8 K for [Cu_3] (a) and [Ni_3] (b). The solid line in (a) is the Brillouin function for S = 1/2 using g = 2.08.

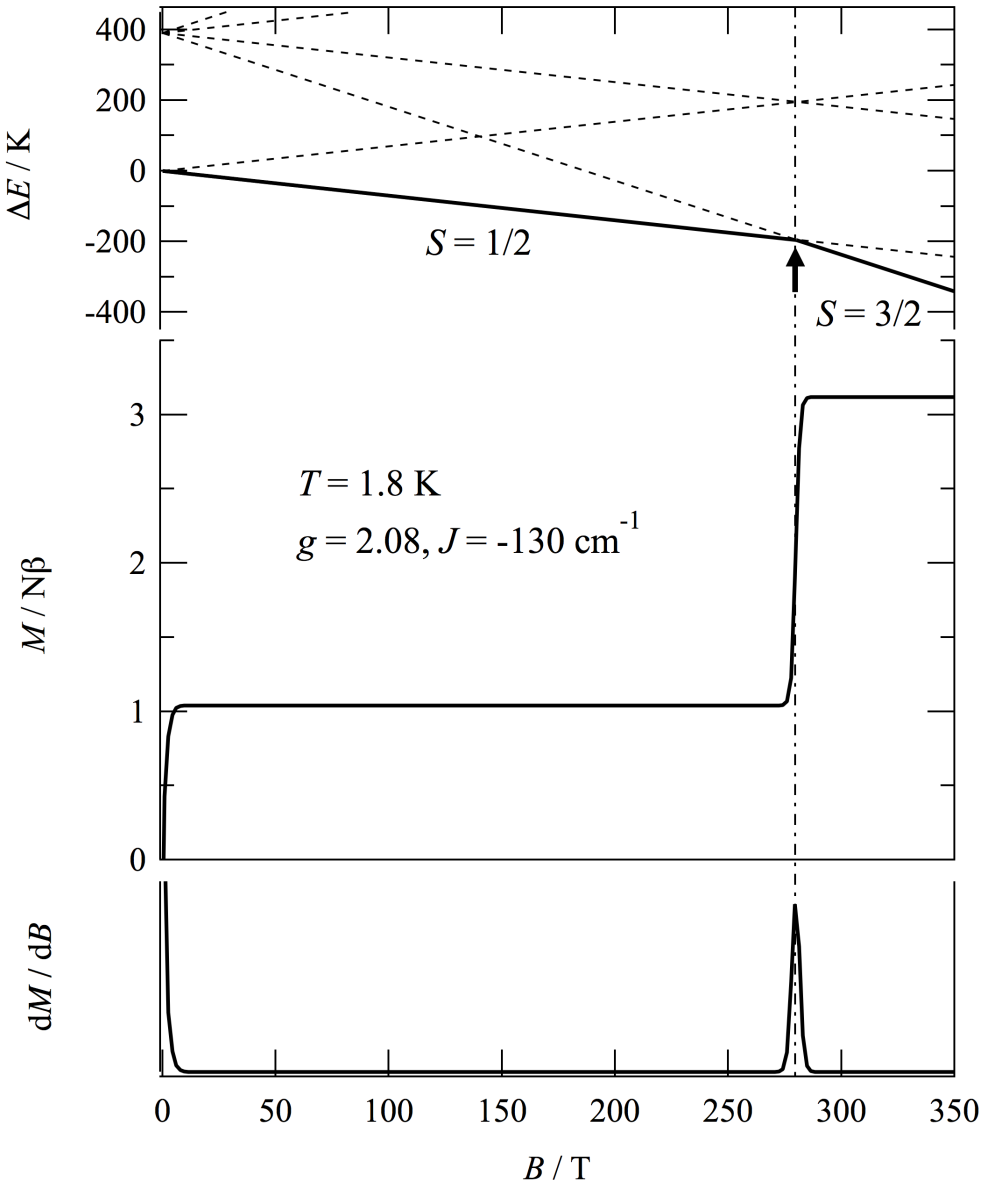

Figure 4.8: Calculated magnetization curves for [Cu_3]. (Top) Energy diagram for the regular triangle ring of antiferromagnetic spins (S = 1/2). (Middle) Calculated magnetization curves. (Bottom) Differentiation of magnetization curves.

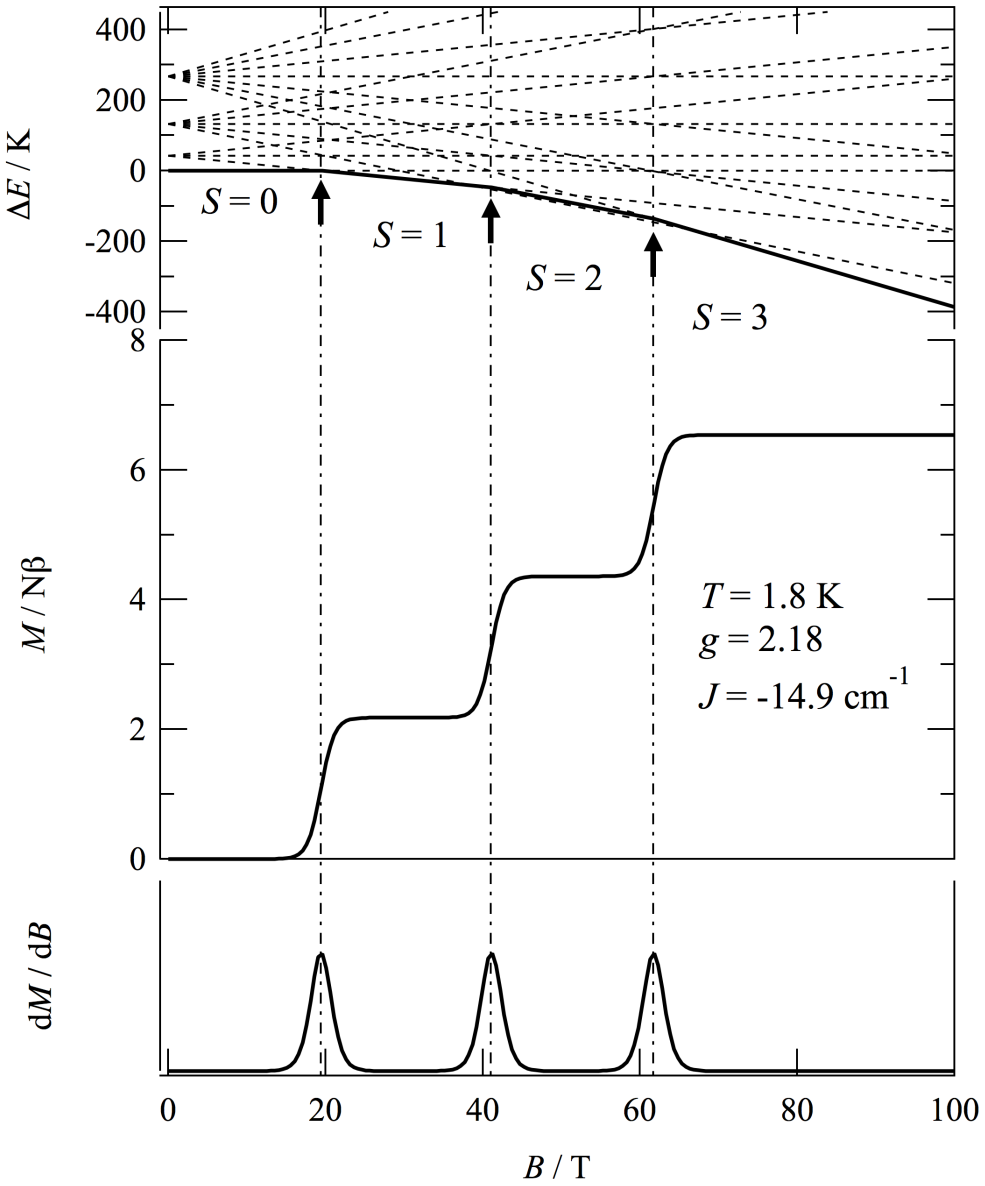

Figure 4.9: Calculated magnetization curves for [Ni_3]. (Top) Energy diagram for the regular triangle ring of antiferromagnetic spins (S = 1). (Middle) Calculated magnetization curves. (Bottom) Differentiation of magnetization curves.

4.4 Conclusion

A novel guanidine derivative and its tri-nuclear metal complexes were synthesized. The ligand can coordinate three metal ions by its N4 coordination positions, forming planar triangular structures. The exchange coupling constants were g = 2.08(1), J = -130(1) cm^{-1} for [Cu_3], and g = 2.18(1), J = -14.9(1) cm^{-1} for [Ni_3], suggesting that antiferromagnetic interactions are operative between the metal ions in both complexes. The ground spin state of [Cu_3] at low temperature is spin doublet. In the case of [Ni_3], the magnetic susceptibility data and magnetization curve suggest that the ground state of [Ni_3] is spin singlet. It is considered that the synthesized guanidine derivative ligand is useful to construct antiferromagnetic triangle units with planar molecular structures. In this example, counterions and solvent molecules precluded the formation of supramolecular spin tube type arrangements. Further work will attempt to connect the units to form extended structures. The presented complexes are 4+ cations, a fact that may be used to their advantage by employing anionic bridging units to link them into extended systems. These results will shed light on the molecular design of planar triangular building blocks and extended spin tubes.

---

[1] Choi, K.-Y., Matsuda, Y. H., Nojiri, H., Kortz, U., Hussain, F., Stowe, A. C., Ramsey, C. & Dalal, N. S. Observation of a Half Step Magnetization in the {Cu_3}-Type Triangular Spin Ring. *Phys. Rev. Lett.*, **96**, 107202 (2006).

[2] Casarin, M., Corvaja, C., di Nicola, C., Falcomer, D., Franco, L., Monari, M., Pandolfo, L., Pettinari, F. & Tagliatesta, P. Spontaneous Self-Assembly of an Unsymmetric Trinuclear Triangular Copper(II) Pyrazolate Complex, [$Cu_3(\mu_3$-OH)(μ-pz)$_3$(MeCOO)$_2$(Hpz)] (Hpz = Pyrazole). Synthesis, Experimental and Theoretical Characterization, Reactivity, and Catalytic Activity. *Inorg. Chem.*, **43**, 5865-5876 (2004).

[3] Costes, J.-P., Dahan, F. & Laurent, J.-P. Synthesis, Characterization, Structure, and Magnetic Properties of the Novel Trinuclear Copper(II) Hydro Complex [$(AE)_3Cu_3OH$](ClO_4)$_2$ (AEH = 7-amino-4-methyl-5-aza-3heptane-2-one). *Inorg. Chem.*, **25**, 413-416 (1986).

[4] Escuer, A., Vicente, R., Peñalba, E., Solans, X. & Font-Bardía, M. Synthesis, Crystal Structure, and Magnetic Behavior of (μ_3-CO_3)[Cu_3(Medpt)$_3$(ClO_4)$_3$](ClO_4): A New Copper(II) Carbonato-Bridged Complex with a Triangular Array. *Inorg. Chem.*, **35**, 248-251 (1996).

[5] Lieb, E., Schultz, T. & Mattis, D. Two soluble models of an aniferromagnetic chain. Ann. Phys., 16, 407-466 (1961).

[6] Kawano, K. & Takahashi, M. Three-Leg Antiferromagnetic Heisenberg Ladder with Frustrated Boundary Condition; Ground State Properties. *J. Phys. Soc. Jpn.*, **66**, 4001-4008 (1997).

[7] Sakai, T. & Sato, M. Vector chirality and inhomogeneous magnetization in frustrated spin tubes in high magnetic fields. *Phys. Rev. B*, **75**, 014411 (2007).

[8] Sakai, T., Sato, M., Okunishi, K., Otuka, Y., Okamoto, K. & Itoi, C. Quantum phase transitions of the asymmetric three-leg spin tube. *Phys, Rev. B*, **78**, 184415 (2008).

[9] Manaka, H., Hirai, Y., Hachigo, Y., Mitsunaga, M., Ito, M. & Terada, N. Spin-Liquid State Study of Equilateral Triangle S = 3/2 Spin tubes Formed in $CsCrF_4$. *J. Phys. Soc. Jpn.*, **78**, 093701 (2009).

[10] Seeber, G., Kögerler, P., Kariuki, B. M. & Cronin, L. Supermolecular assembly of ligand-directed triangular {Cu^{II}_3Cl} clusters with spin frustration and spin-chain behaviour. *Chem. Commun.*, 1580-1581 (2004).

[11] Ivanov, N. B., Schnack, J., Schnalle, R., Richter, J., Kögerler, P., Newton, G. N., Cronin, L., Oshima, Y. & Nojiri, H. Heat Capacity Reveals the Physics of a Frustrated Spin Tube. *Phys. Rev. Lett.* **105**, 037206 (2010).

[12] Clegg, J. K., Lindoy, L. F., McMurtrie, J. C. & Schilter, D. Extended three-dimensional supermolecular architectures derived from trinuclear (bis-β-diketonato)copper(II) metallocycles. *Dalton Trans*., 3114-3121 (2006).
[13] Müller, I. M. & Möller, D. A New Ligand for the Formation of Triangular Building Blocks in Supermolecular Chemistry. *Eur. J. Inorg. Chem*., 257-267 (2005).
[14] Gong, Y.-H., Miomandre, F., Méallet-Renault, R., Badré, S., Galmiche, L., Tang, J., Audebert, P. & Clavier, G. Synthesis and Physical Chemistry of *s*-Tetrazines: Which Ones are Fluorescent and Why? *Eur. J. Org. Chem*., **35**, 6121-6128 (2009).
[15] He, Z., Craig, D. C. & Colbran, S. B. Structures and properties of 6-aryl substituted tris(2-pyridylmethyl)-amine transition metal complexes. *Daluton Trans*. 4224-4235 (2002).
[16] Zeng, F. & Yu, Z. Construction of Highly Active Ruthenium(II) NNN Complex Catalysts Bearing a Pyridyl-Supported Pyrazolyl-Imidazolyl Ligand for Transfer Hydrogenation of Ketones. *Organometallics* **28**, 1855-1862 (2009).

APENDIX

I. Calculation Procedure for Kambe's method

Kambe's method was applied for [Cu_3] and [Ni_3] (CHAPTER 4).[1] Igor Pro 3.0 or later is required.

```
// Kambe's method
// Regular triangle model spin Hamiltonian
//
// S1, S2, S3; Cu(II)
//
// H = -2 J (S1S2 + S2S3 + S3S1)
// S12 = S1 + S2, ST = S12 + S3

#pragma rtGlobals=1                    // Use modern global access method.

Constant M1 = 2     // Spin multiplicity
Constant M2 = 2
Constant M3 = 2

Constant STATE_S1  = 0
Constant STATE_S2  = 1
Constant STATE_S3  = 2
Constant STATE_S12= 3
Constant STATE_ST  = 4

Constant BOHR                = 4.6686437e-5      // cm-1 G-1
Constant BOLTZMANN           = 0.69503877        // cm-1 K-1

Menu "Macros"
        "Initialize", Init()
End

Function Init()
        Variable ss1, ss2, ss3, ss12, sst, i
        Variable /G states
        Make /D /O /N=(30000, 5) state

        ss1 = M1 - 1          // twice of S1
        ss2 = M2 - 1
        ss3 = M3 - 1
```

```
	i = 0
	For	(ss12=abs(ss1-ss2); ss12<=ss1+ss2; ss12+=2)
		For(sst=abs(ss12-ss3); sst<=ss12+ss3; sst+=2)
					state[i][STATE_S1	] = ss1 / 2
					state[i][STATE_S2	] = ss2 / 2
					state[i][STATE_S3	] = ss3 / 2
					state[i][STATE_S12	] = ss12 / 2
					state[i][STATE_ST	] = sst / 2
					i += 1
		Endfor
	Endfor

	states = i
	Redimension /N=(states, -1) state
End

Function FitXmT(w, t) : FitFunc
	Wave w; Variable t
	Variable g, j, theta
	Variable st,ej,xmt,a,b,i
	Wave state
	NVAR states

	g	= w[0]
	j	= w[1]		// cm-1
	theta	= w[2]		// K
//	t	= temperature	// K

	For(a=0,b=0, i=0;i<states;i+=1)
		st	= state[i][STATE_ST]
		ej	= -j * st * (st+1)
		a += st * (st+1) * (2*st+1) * exp(-ej/BOLTZMANN/t)
		b += (2*st+1) * exp(-ej/BOLTZMANN/t)
	Endfor

	xmt = 0.1251 * g^2 * a / b
	Return(xmt * t / (t - theta))
End
```

[1] Kambe, K. On the Paramagnetic Susceptibilities of Some Polynuclear Complex Salts *J. Phys. Soc. Jpn.* **5,** 48-51 (1950).

ACKNOWLEDGEMENT

The author would like to thank all member of Oshio's laboratory. The author is very grateful to Professor Hiroki Oshio, Dr. Masayuki Nihei, Dr. Takuya Shiga, and Dr. Graham Neil Newton for their kind advices and valuable discussion throughout this study. The author is grateful to Professor Takahiko Kojima, Kazuya Saito, and Yasuhiko Yamamoto for reviewing for this thesis and for the valuable discussion. The author deeply thanks Prof. Youichi Murakami and Prof. Reiji Kumai (High Energy Accelerator Research Organization) for the structural analyses using a synchrotron, Prof. Hiroshi Okamoto (The Tokyo University) for single crystal absorption spectroscopy, Prof. Shinya Hayami (Kumamoto University) for light irradiation Mössbauer spectroscopy, and Dr. Yuji Furukawa (Iowa State University) for solid state NMR measurements. Thanks are also due to his parents for their kind encouragements and support.